UNIVERSITY OF CALGARY

Understanding Tribocorrosion of Pipeline Steels: Measuring the Impact of Hydraulic Fracturing Fluid Additives on Material Loss

by

Edwin David Yánez Orquera

A THESIS
SUBMITTED TO THE FACULTY OF GRADUATE STUDIES
IN PARTIAL FULFILLMENT OF THE REQUIREMENTS FOR THE
DEGREE OF MASTER OF SCIENCE

DEPARTMENT OF MECHANICAL AND MANUFACTURING ENGINEERING

CALGARY, ALBERTA
August, 2021

Abstract

Hydraulic fracturing operations involve the use of highly pressurized water mixtures that contain solid proppant particles as well as a variety of additives to function as drag reducers, corrosion inhibitors, bactericides, and other related compounds. In the current study, the influence of three of such additives (Dynarate 6524, DWP 621-1, and CalGuard 3100) on the wear of transporting pipelines made of AISI 4715 steel is assessed through tribocorrosion experiments. More specifically, electrochemical measurements have been conducted including, open circuit potential (OCP), linear polarization resistance (LPR), potentiodynamic polarization, and electrochemical impedance spectroscopy. Evaluation of the wear generated in tribocorrosion experiments was accomplished through optical profilometry and scanning probe microscopy. Scanning electron microscopy (SEM) imaging has been used to study the surface of the samples after testing. Energy dispersive X-ray spectroscopy (EDX) was also used to construct compositional maps of the elements left on worn surfaces. Finally, a statistical study using response surface methodology (RSM) has been conducted to identify the optimal blend of additives that minimizes wear. With RSM, it was found that all additives mitigate tribocorrosion wear, and that the use of Dynarate alone is reduces overall wear the most.

Preface

This thesis constitutes original work conducted by the author, Edwin David Yánez Orquera, in fulfilment of the requirements of the MSc. program with the department of Mechanical and Manufacturing Engineering at the University of Calgary. The body of the thesis constitutes unpublished work with the data portrayed on Figs. 4.1, 4.2, 4.3, and 4.4 in Section 4.1 which have been published as part of a collaborative effort in the journal *Tribology International* [1].

Acknowledgments

I would like to expresss my deepest gratitude to my supervisor, Dr. Philip Egberts, whose expertise and desire to help have proven to be invaluable over the curse of this project. Likewise, the quality of this project would not have been possible without the aid from my co-supervisor, Dr. Frank Cheng, who has open the doors of collaboration to his research group well known for their knowledge of corrosion. A special thanks to Calfrac Well Services Ltdfor their role in making this project possible. Likewise, I would also like to thank Dr. Joanna Wong who has kindly provided a portion of her lab that provided the physical space need to run these experiments. I would also like to show appreciation for the aid from Dr. Jitendra Panda who, as a postdoc in the research group, was instrumental in scoping the project and providing insightful suggestions. A special mention to Dr. Simon Park who provided access to the optical profilometer used in this project as well as his student, Chaneel Park, who cordially taught me how to operate the instrument. I must also mention Christopher Debuhr, the SEM operator, who skillfully conducted the measurements.

I would also like to extend a general sentiment of gratitude to all the people in the Dr. Egberts research group whose professionalism, dedication, and affable attitudes have created a hospitable work environment.

An special thanks to Don Knuth, Leslie Lamport, and Peter Wilson [2–4] whose contributions to the LaTeXproject has enabled me to produce this thesis.

This section would now be complete without offering my most sincere appreciation to my parents who have been crucial in providing the emotional support needed in overcoming the obstacles encountered over the course of the project.

Dedicated, with love and affection, to my mom and dad.

Table of Contents

Abstract . . . . . **ii**

Preface . . . . . **iii**

Acknowledgments . . . . . **iv**

Dedication . . . . . **v**

Table of Contents . . . . . **vi**

List of Tables . . . . . **vii**

List of Figures . . . . . **viii**

1 Introduction **1**

1.1 Motivation 1

1.2 Document Structure 3

2 Literature Review **5**

2.1 Theoretical Background 5

2.1.1 Drag reducers 5

2.1.2 Friction 8

2.1.3 Lubrication 9

2.1.4 The Synergism Approach to Tribocorrosion 12

2.2 Research opportunity 14

3 Experimental **16**

3.1 Sample preparation 17

3.2 Tribometer 18

3.2.1 Apparatus 19

3.2.2 Apparatus Control 21

3.3 Electrochemical cell 24

3.3.1 Electrochemical Tests and Parameters . . . 24
3.3.2 Electrolyte . . . 28
3.3.3 Custom Lugging Probe . . . 29
3.4 Data Processing . . . 30
3.4.1 Friction coefficient . . . 31
3.4.2 Wear Assessment . . . 34
3.4.2.1 Wear by Optical Profilometry . . . 36
3.4.2.2 Wear by Scanning Probe Microscopy (SPM) . . . 39
3.4.3 Optimization of Additive Combinations . . . 42
4 Results . . . 46
4.1 First batch: overall additive effects . . . 46
4.1.1 Discussion . . . 51
4.2 Second batch: optimization for least material loss . . . 60
4.2.1 Discussion . . . 69
4.3 Third batch: Exploration into Dynarate 6524 . . . 70
4.3.1 Discussion . . . 78
5 Conclusion and Recommendations . . . 83
5.1 Conclusions . . . 83
5.2 Recommendations . . . 84
Bibliography . . . 86
Appendix A: HTDS water analysis . . . 101
Appendix B: Equations Related to the Measurement of the Coefficient of Friction . . . 103
Appendix C: Optical Artifacts . . . 106
Appendix D: Reduced RSM Model . . . 109
Appendix E: Extended drift experiment . . . 111

List of Tables

3.1 Experimental parameters 19

3.2 Apparatus details 21

3.3 PID gains used for batches 2 and 3 24

3.4 Face-centered CCD experimental design for batch 2. 45

4.1 Synergism and Dominant Wear tests 58

4.2 Analysis of coded coefficients 61

4.3 Analysis of Variance 62

4.4 Summary Statistics for the CCD Model 64

4.5 Optimal additive combination 68

4.6 Predicted response at optimal parameters 68

4.7 Fitting PEIS parameters for the equivalent circuit. 71

List of Figures

1.1 Schematic illustrating how a typical hydraulic fracturing operation takes place. Image obtained from Ref. [5] 2

1.2 Schematic showing abrasive and erosive wear caused by proppant particles traveling along the pipeline. 3

1.3 Factors influencing a tribocorrosion system. Adapted from Ref. [8]. 4

2.1 Schematic showing the interaction of drag reducing additives in fluid flow through a pipeline: (a) a coiled chain molecule slightly reduces eddy currents, and (b) a extended chain being more effective at making the fluid more laminar. Schematics obtained from Ref. [11]. 6

2.2 Films produced by polymer viscosity modifiers: (a) a layer of adsorbed polymer serves as a lubricant in the boundary regime, and (b) in the fluid friction regime the contacts are separated by the medium. Figure obtained from [19]. 7

2.3 A schematic of the Stribeck curve is provided above. Below is one of the original figures published by Stribeck. The axes y and x axes read *Coefficient of Friction* and *Revolutions per minute*. The traces correspond to different loads with T = 25°C, ϕ shaft = 70 mm, P_{Geom} = 0.1-2.0 MPa, oil for gas powered engines $\eta \approx$ 180 mPa·s. Graphs obtained from Ref. [27]. 10

2.4 Examples of organic and inorganic films used as boundary lubricants: (a) hexadecanol on metallic surface, (b) stearic acid forming a monolayer of iron stearate, and (c) film formed by reaction of sulfur with steel. Figure obtained from Ref. [29]. 11

2.5 (a) Measurements conducted on a passive material where the onset of rubbing has a marked effect on the open circuit potential. (b) Measurements conducted on a material not exhibiting passive film formation. (c) and (d) Nyquist plots conducted on the passive material of part (a) along the segments labeled 1-4. Plots obtained from Ref. [38]. 13

3.1 A sample of steel from batch 1 displaying the cutout area taken prior to testing. 18

3.2 Reciprocating tribometer used. 20

3.3 Examples of load control effects based on: a) average over a full cycle, and b) PID using recent data points. 23

3.4 Delrin reservoir mounted on a steel sample from batch 1. 25

3.5 Equivalent circuits: (a) Randles Circuit, and (b) Modified Randles circuit for a porous coating. 28

3.6 Friction loop where the positive and negative data points correspond to the forward and backward direction of reciprocation. A visualization of the window used to trim the ends of the data is shown as the middle section delimited by thin vertical green lines. 34

3.7 Evolution of friction coefficient over the course of a test. 35

3.8 Wear track measurement according using Zeta-20 apparatus. (a) A portion of the metallic sample under the optical lens. The wear track is seen as a darker strip running from the lower left corner to the upper right corner. (b) Profiles over the wear track corresponding to the crossing white lines on part (a). 37

3.9 Comparison between topographical maps of the wear track on the same sample of steel. a) Topography obtained from optical data. b) Topography obtained from SPM data. 40

3.10 Illustration of the construction of the rectangular region. 41

3.11 3-dimensional representation of the Face-Centered Central Composite Design labeled in Yates order. Based on [85]. 44

4.1 Kinetic Coefficient of Friction (COF) measured over the course of T-type experiments. Each colour represents a different testing medium where D stands for DI-water and H stands for HTDS water. The subscripts, where present, indicate the additives in solution. Originally published on [1]. 47
4.2 Kinetic Coefficient of Friction (COF) measured over the course of W_0-type experiments. Each colour represents a different testing medium where D stands for DI-water and H stands for HTDS water. The subscripts, where present, indicate the additives in solution. Originally published on [1]. 48
4.3 Open circuit potential OCP for steel samples undergoing reciprocating abrasion under several electrolytes. Each colour represents a different electrolyte where D stands for DI-water and H stands for HTDS water. The subscripts, where present, indicate the additives in solution. In the figure, 1000 cycles is approximately equivalent to 90 minutes. Originally published on [1] 49
4.4 Potentiodymaic polarization curves. Originally published on [1]. 50
4.5 Results from batch 1. Hhe electrolytes used are portrayed as follows: D for DI water, and H for HTDS water. The additives are represented by subscripts as follows: Dy for Dynarate, Dw for DWP, and C for CalGuard. The wear conditions are represented as follows: T for normal conditions, C_0 for corrosion wear only, and W_0 for abrasion under cathodic protection. Originally published on [1]. . . 51
4.6 Sodium acrylate–acrylamide, an example of anionic copolymer structure. Structure generated with Ref. [98]. 55
4.7 Copolymer of acrylamide and acryloyloxyethyltrimethyl ammonium chloride, an example of a cationic copolymer structure. Structure generated with Ref. [98]. . 55
4.8 Adsorbed polymer brush configurations. Figure obtained from Ref. [105]. 57
4.9 Normal plot of standardized effects. 64
4.10 Normal Probability plot of residuals. 65
4.11 Plot of residuals vs fit. 66
4.12 Plot of residuals vs. chronological order of data collection. 66

4.13 Contour Plots showing the degree of wear according to the model. 67
4.14 Interaction plots 68
4.15 Linear Polarization curves for the system while left still and under reciprocating motion. 71
4.16 Nyquist plots taken before, during, and after the onset of reciprocation. The data is presented in the form of scatter points while the lines represent the best fit according to parameters on Table 4.7 72
4.17 Bode plots showing the raw data collected during the same experiment as that of Fig 4.16 72
4.18 Direction of drift over time for (a) under reciprocation motions and (b) left undisturbed. Each trace corresponds to one PEIS scan. The arrow indicates the direction of growth over time. 73
4.19 Schematic of steel samples as seen from above. The sample in part (a) represents a sample where reciprocating motion has been allowed to take place. The sample in part (b) represents a sample where the wear track is absent because no reciprocation has taken place. 74
4.20 SEM imaging of a steel sample after a T-type test. 75
4.21 SEM imaging of a steel sample after a C_0-type test. 76
4.22 SEM imaging of a steel sample after a W_0-type test. 77
4.23 Hardness distribution in distance from the center of the wear scar in a T-type experiment. 78
4.24 Schematic of the porous nature of adsorbed coatings formed by inhibitors. Taken from [35]. 81

Chapter 1

Introduction

> If we knew what it was we were doing, it would not be called research, would it?
>
> Albert Einstein[1]

What Dynarate 6524, DWP 621-1, and CalGuard 3100 have in common is that they are slickwater additives manufactured by Calfrac Well Services Ltd, and are currently being utilized in the fracking industry. Through a partnership with Calfrac Well Services Ltd, these additives have been provided to conduct a Tribocorrosion study on the degradation of pipeline steel AISI 4715. The following pages of this thesis constitute a report on such study, the procedures used, and its findings.

1.1 Motivation

The activity of fracking (or hydraulic fracturing) for the extraction of hydrocarbons is, as described in a report by the Department of Energy of the United States [5], a process that targets deposits trapped in rock shale formations. First, a well is drilled vertically until the

[1]While the quote in the epigraph is usually attributed to the renown scientist Albert Einstein, the author of the present work has been unable to find a trustworthy source for the attribution. Regardless of origin, the quote is used here as it encapsulates the open ended nature of research work.

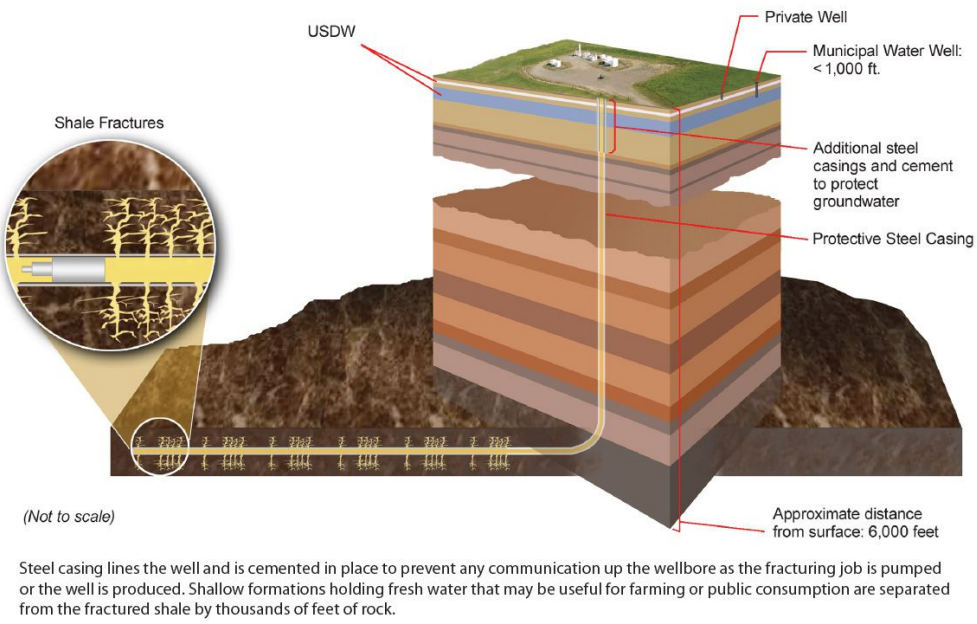

Figure 1.1: Schematic illustrating how a typical hydraulic fracturing operation takes place. Image obtained from Ref. [5]

rock formation is reached. Then, drilling continues horizontally across the rock formation in an attempt to maximize the number of natural fractures in the rock [5]. Once the pathway is set up, highly pressurized water is injected in the well which in turn fractures the surrounding rock [5]. Along with the water flow, some proppant particles are sent into the well to prop open the fractures [5]. Here, corrosion is an issue because because the thinning of the pipeline walls can lead to a weakened structure that is no longer safe to operate at high pressures. Thinning of the pipeline walls is further accelerate by the action of the proppant particles that impact and abrade the inner wall as they are carried by the water flow. An illustration of this process is provided in Fig. 1.1. This process can take place in as many as 25 fracturing stages per well [5]. The presence of these proppant particles in the water flow suggests that investigating the degradation of these piping systems is a issue of Tribocorrosion.

According to Wood [6], the term *Tribocorrosion* is rooted in the terms *tribos* (Greek word that means rubbing) and *corrodere* (medieval Latin word that means to gnaw with force). Therefore, tribocorrosion alludes to the study of surface degradation in the presence of both mechanical wear and corrosion processes [6]. As such, the study of tribocorrosion systems is

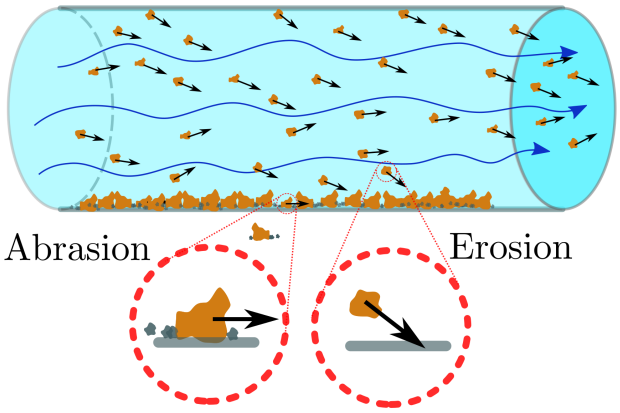

Figure 1.2: Schematic showing abrasive and erosive wear caused by proppant particles traveling along the pipeline.

usually separated into two broadly defined categories according to the mechanical actions induced by particles: sliding or rolling of solids, and impingement of particles [7]. The present study is concerned with the former case where proppant particles are assumed to slide along the inner surface of the pipeline resulting in abrasion as depicted in Fig. 1.2.

Tribocorrosion studies usually deal with highly complex systems resulting from the interaction of many interdependent factors. In examining the complexities of such systems, four broad categories have been defined to classify such factors: mechanical or operational, electrochemical, solution, and materials [8–10]. Fig. 1.3 highlights some examples of factors arranged according to these categories. It is the objective of the current study to investigate the effect that the additives provided by Calfrac Well Services Ltd have on altering the degree of wear of pipeline steel. For that purpose, in the present study, an effort has been made to keep consistency between as many of these factors as possible, where the only factors varied for experimental purposes are the load, solution composition, and applied potential.

1.2 Document Structure

The body of the document is organized in five main chapters: Introduction, Literature Review, Experimental, Results, and Conclusion and Recommendations. The *Introduction* chapter

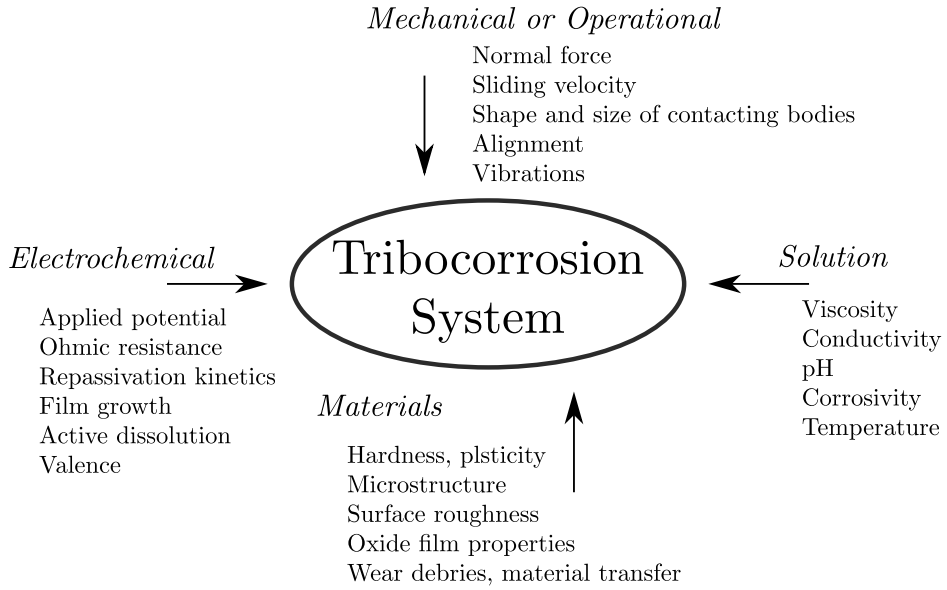

Figure 1.3: Factors influencing a tribocorrosion system. Adapted from Ref. [8].

presents a brief overview of the real world problem that this study attempts to model. The *Literature Review* chapter provides context as to the history and current understanding of the phenomenology that informs the development of the project. The scope of the chapter has been limited to published literature as well as the most substantial contributions in the field. The *Experimental* chapter provides ample detail regarding the methods used, instrument specifications, and data processing. The *Results* chapter is subdivided into three sections that mirror the three major batches of experiments conducted for the current work. Each subsection carries its own Discussion section that attempts to explain the experimental data. Finally, the *Conclusions and Recommendations* chapter summarizes the major findings of the study and provides some suggestions aimed to better inform future experiments and research avenues.

Chapter 2

Literature Review

2.1 Theoretical Background

2.1.1 Drag reducers

As recounted by Yang et al. [11], contemporary hydraulic fracturing uses large quantities of fracturing fluid in the realm of ≈ 120 bbl/min. Over the length of the hydraulic system, including pipelines and underground pathways, large friction losses can be produced. These losses in turn increase costs of operation and can even damage the pumping equipment due to the elevated pressures necessary to sustain such high flow rates [11]. To address this issue, one class of additives referred to as *Friction Modifiers* or *Drag Reducers* are mixed with the fluid. It is thought that these additives work by eliminating the energy losses associated with turbulent flow [11]. Fig. 2.1 illustrates how the morphology of the hydrocarbon chain is thought to dissipate eddy currents resulting in a more laminar flow. In line with the present study, one widely used class of such additives are those based on polyacrylamide polymers which are used in a quantities as little as 0.1 wt% [11].

In laboratory settings, it has been demonstrated that the introduction of polyacrylamide polymers, even in in small quantities, can indeed reduce the fanning friction coefficient for turbulent flows [12]. Moreover, in recent decades, studies have been specifically conducted

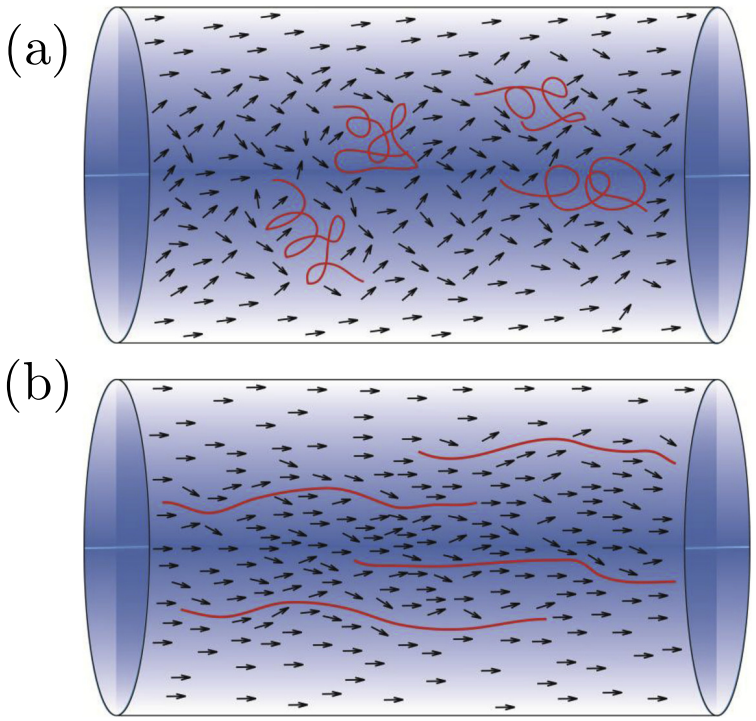

Figure 2.1: Schematic showing the interaction of drag reducing additives in fluid flow through a pipeline: (a) a coiled chain molecule slightly reduces eddy currents, and (b) a extended chain being more effective at making the fluid more laminar. Schematics obtained from Ref. [11].

towards documenting the rheological properties of polyacrylamide solutions [12–14]. In addition to their effect in altering turbulent flows, it has been found that polyacrylamide solutions tend to act as a thinner agents [13, 14]. That is, they have the effect of reducing the fluid viscosity as the shear rate is increased.

The implication is that, when acting as lubricants between solid contacts (i.e. proppant particles sliding along the pipeline surface), the effectiveness of polyacrylamide solutions should be reduced. Yet, despite the decrease in viscosity, there is an indication that such solutions may still offer some degree of lubricity between the proppant and the steel. This is because Kato et al. [15] have demonstrated that even dilute polyacrylamide solutions are able to form adsorbed boundary lubricating films.

In this sense, the phenomenon of lubrication in aqueous polyacrylamide solutions parallels that of lubrication in oil based lubricants where polymers are intentionally introduced as thinning agents [16, 17]. The reasoning behind this practice is that tight design tolerances

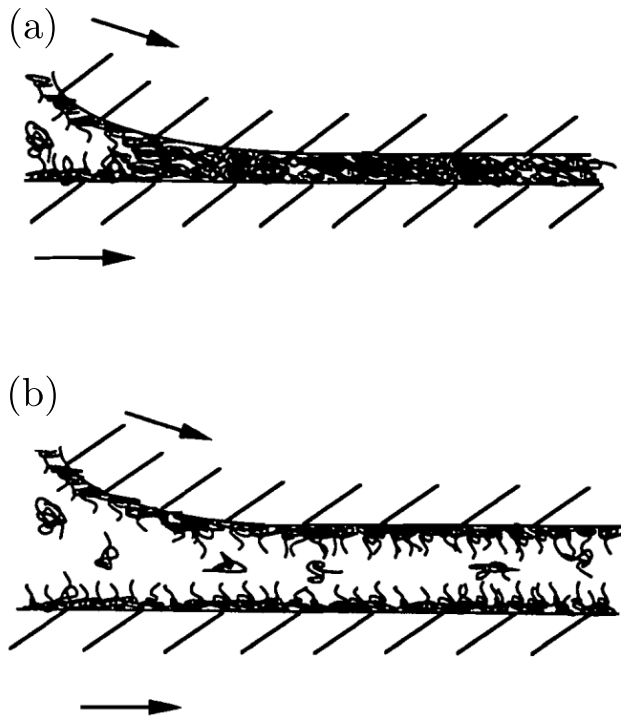

Figure 2.2: Films produced by polymer viscosity modifiers: (a) a layer of adsorbed polymer serves as a lubricant in the boundary regime, and (b) in the fluid friction regime the contacts are separated by the medium. Figure obtained from [19].

favor lubricants where the thickness of the fully developed film is as thin as possible [18]. Yet as Murdoch et al. point out [18], this practice often leads to the prevalence of the boundary and mixed lubrication regimes. It is in these close contact regimes that the film forming capabilities of the polymer additives come into place. Fig. 2.2 shows a schematic of solid contacts lubricated by a medium containing polymer additives. In part (a) in the figure, solid contacts in the boundary regime are depicted. In part (b), the conditions are such that a fully formed liquid flow separates the solid contacts. The key takeaway from this section is that polymer drag reducing agents can be effective at reducing friction in fluids by two mechanisms: in purely liquid flow they reduce energy losses by reducing eddy currents, and as lubricants between solid contacts where they can provide boundary lubrication.

2.1.2 Friction

In the textbook *Tribology on the Small Scale* [20], it is explained that the first recorded observation about the relationship between the tangential force required to move an object on a flat surface and the weight of said object are attributed Leonardo da Vinci (1452-1519). However, the first published work formalizing these observations corresponds to Guillaume Amontons, who in 1699 published what is now know as Amontons' first and second laws of friction in a work published in the Proceedings of the French Royal Academy of Sciences. A later work by Coulomb (1452-1519) complemented the first two laws with an new postulation regarding objects already in motion. Since then, these three laws are known as the Amontons' and Coulomb's laws of friction and are stated as follows:

1. The friction force is proportional to the normal load.
2. The friction force is independent of the apparent area of contact.
3. Kinetic friction is independent of sliding velocity.

The statement of the first law can be expressed in the form of Equation 2.1 where the Greek letter μ symbolizes the dimensionless coefficient of friction (COF). The second law uses the term *apparent* when referring to the area of contact because in most situations the friction between objects appears independent of their size [20]. However, as it is now better understood since the the times of Amontons and Coulomb, the real contact surface between solid objects does have an effect on their tribological properties [21].

$$\mu = \frac{\text{tangential force}}{\text{normal load}} = \frac{F}{L} = \frac{F_X}{F_Z} \tag{2.1}$$

The third law is a modification regarding the first law. It arises from the observation that objects tend to require a higher tangential force to initiate sliding than the force require to maintain movement. Therefore, a distinction is made between the static and kinetic friction coefficients [20]. Both of these friction coefficients are modeled through the same Equation

2.1, the only parameter that changes is whether the tangential force is measured at the onset of movement or while the object is already sliding [20]. In the context of the current study, the tangential force will be associated with the F_x term and the applied normal load with the F_z term. A caveat to this approach, pointed out in the *Encyclopedia of Tribology* [22], is that the kinetic friction coefficient is highly reliant on the specific experimental conditions. In addition, measurements can be affected by the *Running-in* effect, a transitional phenomenon that is characterized for a changing kinetic coefficient of friction over time [22, 23]. It is because of these later factors that ample detail will be provided in the Experimental section of the current study to facilitate replicability of the results.

2.1.3 Lubrication

The modern understanding of Lubrication has its roots in the experimental work published by Beauchamp Tower between 1883 and 1885 [24, 25]. While conducting experimental research in a custom rig designed to study journal bearings, he was the first to document the formation of a liquid layer of oil capable of separating solid contacts pressed together under load. Tower's experimental work was complimented by Osborne Osborne Reynolds whom in 1886 provided the theoretical framework to explain Tower's findings findings [26]. As recounted by Woydt and Wäsche [27], Stribeck used this theoretical framework to conduct detailed experiments measuring the evolution of the coefficient of friction with the rotational speed of journal bearings in 1902. It is after his work that the well known Stribeck curve is named. A schematic of a common Stribeck curve is provided in Fig. 2.3 along with one of Steinbeck's original experimental plots. As seen in the figure, the empirical measurements show a longer a predominance of Mixed and Fluid friction regimes. According to this theory, lubrication will occur as long as there is enough relative velocity between the solids to promote the formation of a thin liquid film.

However, as expressed by Deeley in 1919 [28], many scientists at the time were not satisfied with this explanation of the phenomenon of lubrication. It had been their experience that

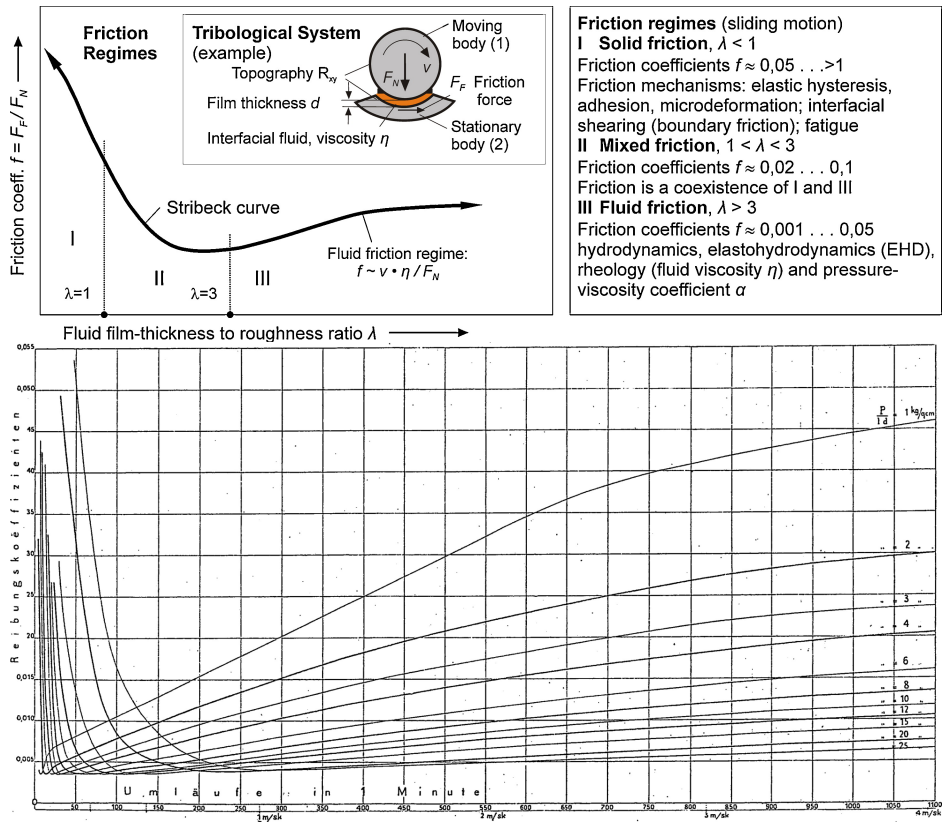

Figure 2.3: A schematic of the Stribeck curve is provided above. Below is one of the original figures published by Stribeck. The axes y and x axes read *Coefficient of Friction* and *Revolutions per minute*. The traces correspond to different loads with T = 25°C, ϕ shaft = 70 mm, P_{Geom} = 0.1-2.0 MPa, oil for gas powered engines $\eta \approx 180$ mPa·s. Graphs obtained from Ref. [27].

mineral oils tended to be outperformed by natural fats (oils derived from plant and animal sources) despite having similar rheological properties. One way to make sense of this gap between theory and practice was through the concept of *oiliness* [28], a loosely defined term that roughly describes the tendency of natural fats to more readily wet metallic surfaces. The pheonomeom of oiliness was therefore related to some other characteristic of the oil.

An important insight regarding the molecular make up of the oil is found in the work of Irving Langmuir in 1920 [30]. While studying wettability of liquids for the extraction of minerals from ores, he documented the drastic reduction of friction coefficients achieved by applying a single layer of oleic acid across several substrates. In this publication, Langmuir stipulates that the behaviour could be caused by the attraction of the carboxyl and double bond groups to the surface of the substrate that leave the rest of the alkyl chain exposed

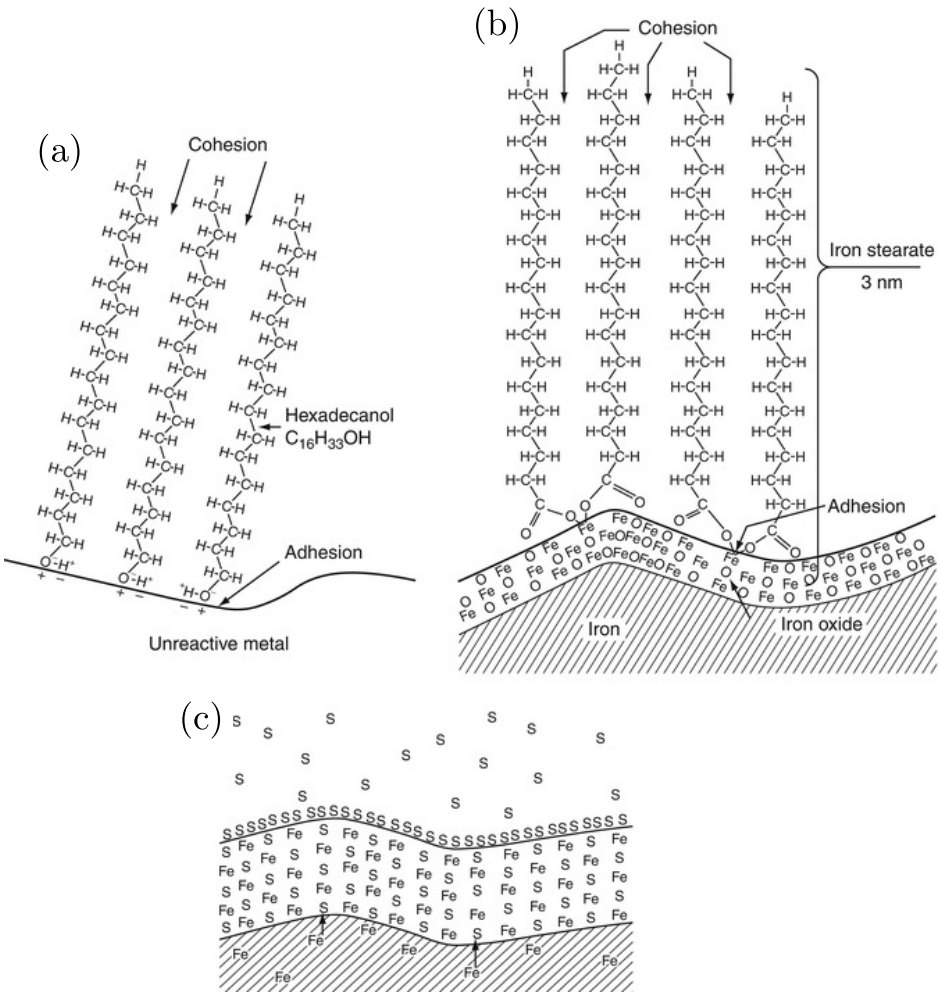

Figure 2.4: Examples of organic and inorganic films used as boundary lubricants: (a) hexadecanol on metallic surface, (b) stearic acid forming a monolayer of iron stearate, and (c) film formed by reaction of sulfur with steel. Figure obtained from Ref. [29].

forming a new surface. This insight was later used by Hardy and Doubleday who were interested in studying lubrication where the solids were not separated by a fully formed liquid film, a set of parameters they refer to as boundary conditions [31]. They found that the coefficient of friction is related to the length of the alkyl chain in that the longer the chain, the lower the coefficient of friction [31]. This concept of a thin lubricant film formed by adsorbed adsorbed molecules is still a relevant model found in more recent publications studying lubrication in the boundary regime [15, 32–36]. As reported on the *Encyclopedia of Nanotechnology*, the understanding of lubricating films in the boundary lubrication regime has undergone only slight changes over the years [29]. Fig. 2.4 shows schematics of organic

and inorganic films of substances commonly used as boundary lubricants.

2.1.4 The Synergism Approach to Tribocorrosion

It is thought that the main driver of tribocorrosion behaviour in passive metals is the degradation of the passive layer due to mechanical wear. This is because once the passive layer is thinned or removed, charges can more readily be exchanged between the substrate and the electrolyte [8, 9, 37]. This phenomenon of mechanical wear altering the electrochemical state of a corroding material has been clearly demonstrated by Ponthiaux et al. [38]. Fig. 2.5 summarizes their findings resulting from potentiodynamic and EIS (electrochemical impedance spectroscopy) measurements. In Fig. 2.5 parts (a) and (b), the Open Circuit Potential measurements on a material that is known to form a passive film, and the same measurements on a material known not to form a passive film are presented. While the onset of rubbing dramatically decreases the potential of the film forming material, there is no such effect in the non-film forming sample. For the material known to form a passive film, Fig. 2.5 (c) and (d) shows the Nyquist plots taken over the course of the experiment. It is readily seen that the capacitance is reduced during rubbing. Yet it also shows that despite similar similar open circuit potentials over segments 1 and 3 and 2 and 4, the underlying capacitance is different over all four segments. While these techniques have their origins in the study of passive metals, Berradja has pointed out that they can succesfully be applied for the study of inhibitors [10].

In assessing the degree of material loss, Muñoz [7] suggests that the above mentioned techniques are only complementary to a more comprehensive approach of which two empirical options are provided: the mechanistic approach, and the synergism approach. Briefly described, the mechanistic approach measures the total loss of material by some form of profilometry, and then seeks to infer which portion of the total is due to corrosion and mechanical wear based on electrochemical measurements [7, 8]. All of this with a single experiment. This approach, however, relies heavily on the assumptions that the corrosion

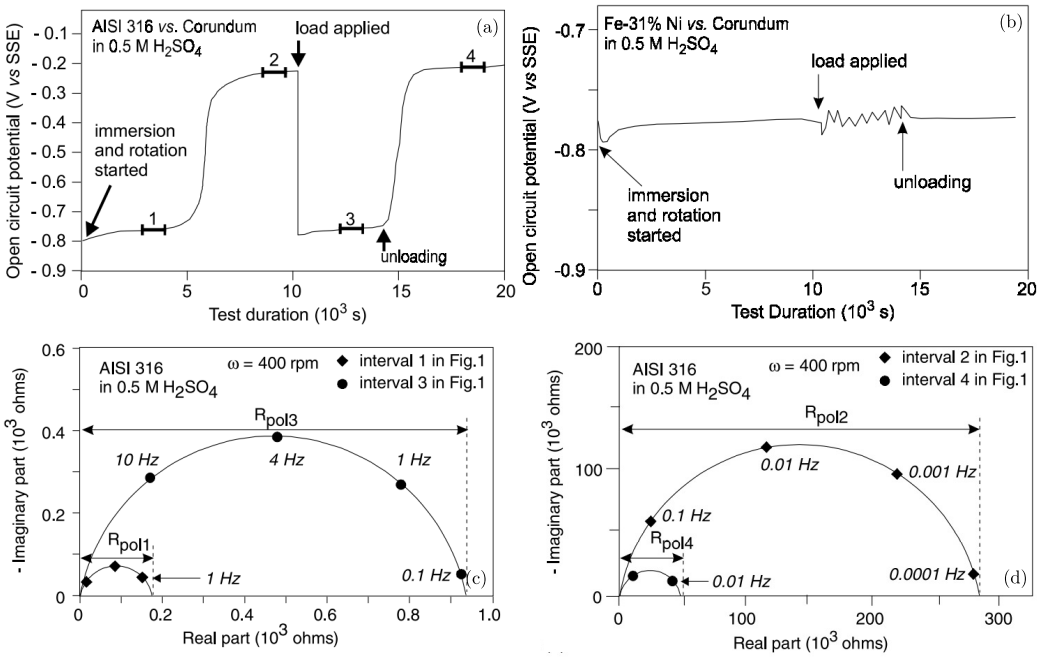

Figure 2.5: (a) Measurements conducted on a passive material where the onset of rubbing has a marked effect on the open circuit potential. (b) Measurements conducted on a material not exhibiting passive film formation. (c) and (d) Nyquist plots conducted on the passive material of part (a) along the segments labeled 1-4. Plots obtained from Ref. [38].

oxidation of the material is precisely known, and that the all current contributions originate in the sample (no side reactions) [7].

By contrast, the synergism approach takes separate measurements for the total loss of material (T) under tribocorrosion conditions, material loss inferred from purely electrochemical (C_0), and material loss measured after purely mechanical wear (W_0), resulting in at least three experiments per measurement [7]. The difference between the sum of the isolated contributions and the total material loss is captured by the synergism term (S). All together, this is approach can be summarized by Equation 2.2. This has now been incorporated in the ASTM standard G119 [39] and has, in recent decades, been used by researches to study sliding systems involving passive and coated materials [7].

$$T = W_0 + C_0 + S \tag{2.2}$$

2.2 Research opportunity

The current thesis studies hydraulic fracturing additives featuring functionalized polyacrylamide co-polymers. The intended use of the additives, in industry, is for the purpose of drag reduction where drag reduction is understood as reducing friction losses during pumping of fluid as outlined in subsection 2.1.1. This information has been communicated internally by Calfrac Well Services Ltd. Polyacrylamide based co-polymers have been used for decades in hydraulic fracturing operations due to their low cost, thermal stability, low environmental impact, and effectiveness in reducing flow drag [11, 40].

This is not to be confused with the effectiveness of the polymer at reducing friction as a lubricant as described in section 2.1.3. Ongoing research regarding this latter aspect is very limited. Yet, in a recent industry report *Water Soluble Polymers for Aqueous Lubricants* (presented at the 74$^{\text{th}}$ Annual STLE Meeting in Nashville) [41], it is shown that polyacrylamides belong to a well known set of commercially available water soluble lubricants. Furthermore, polyacrylamide polymers and their derivatives have been acknowledged as good inhibitors for the oil and gas industry [42]. Essentially, this means that the polyacrylamide backbone can be modified, usually by means of grafting, to exhibit functional groups that make it an even more effective inhibitor [42]. The state of the art in this regard over the past year has been concerned with producing capsaicin derived acrylamide monomers [43, 44]. However, while this is a procedure that produces a better inhibitor, the shortening of the chain can compromise its main function of reducing Eddy currents in the flow. To the author's best knowledge, no recent attempt has been made to assess the either of this two secondary qualities on a contemporary polyacrylamide based drag reducing agent.

For this assessment, the Synergism method described in subsection 2.1.4 is particularly useful in that the electrochemical techniques described there can easily be complemented with real time measurements of the kinetic friction coefficient as defined in subsection 2.1.2. Together, these can offer insight as to the inhibition of steel in the presence of the additives as well as the resistance to sliding movement produced in that environment. Despite its

criticisms, the method remains a staple of the tribocorrosion literature as evidenced by its use in recent publications exploring passive materials and coatings [10, 38, 45–47].

Chapter 3

Experimental

Following the evolution of the project, the overall methodology has been progressively adjusted to reflect iterative improvements. To prevent such changes from limiting the comparability of results, such changes have been implemented in a series of batches resulting in each batch of experiments been conducted under consistent conditions. A total of three batches were carried out during the development of this project. In this section, the overall experimental set up is broken down into discrete components. Changes corresponding to specific batches are addressed in each section.

Following the evolution of the project, the overall methodology has been progressively adjusted to reflect iterative improvements. To prevent such changes from limiting the comparability of results, such changes have been implemented in a series of batches resulting in each batch of experiments been conducted under consistent conditions. A total of three batches were carried out during the development of this project. In this section, the overall experimental set up is broken down into discrete components. Changes corresponding to specific batches are addressed in each section.

In the course of executing the experiments of this thesis, the methodology has been progressively adjusted to reflect the changes arising from lessons learned. To prevent such changes from limiting the comparability of results, such changes have been implemented in a series of batches resulting in each batch of experiments been conducted under consistent

conditions. In this section, the overall experimental set up is broken down into discrete components. Changes corresponding to specific batches are addressed in each section.

3.1 Sample preparation

Segments of carbon steel (AISI 4715) were provided by Calfrac Well Services Ltd. in the form of pipeline sections. Cuboid shaped segments of approximate dimensions 55 x 27 x 6 mm were machined from of these sections for testing. Care was taking during the machining procedure to perform the cuts with lubricant to mitigate work hardening effects. This is especially important when flattening the faces of the sample as to prevent curvature effects from altering the distribution of forces during testing.

Polishing of the samples was performed manually on a Leco GPX200 metallographic polisher. The rotating speed at the wheel was set to 300 RPM under constant water flow. Increasing grits of 60, 180, 320, 400, 600, and 800 silicon carbide sanding disks were used. The samples were held in position with visual inspection every 20 s. After confirming that the previous surface features from the machining process have been removed, the samples orientation on the wheel was flipped and polished successively until only the markings from the sanding process were visible. Once all the markings from the previous orientation have been removed, the grit was increased. The process was repeated for each sample individually. This method was used in all experimental batches.[1]

After polishing, the samples were rinsed with either acetone or ethanol. Compressed air was immediately blown over the samples to ensure that no moisture residue was left on the surface. Roughness analysis of the surface was performed with the use of a Hysitron TI Premier nanoindenter (Brüker Corporation). All samples had a root mean squared surface roughness of 20±5 nm. Because each operation of polishing, measuring, and ultimately

[1] A workaround had been developed in the lab to attach samples similar to the ones used in the current work to the provided instrument holder at the time of this project. This workaround allows for the automated operation of the instrument with multiple samples being processed simultaneously. However, manual polishing was chosen because the variable thickness of these samples resulted in uneven wear.

testing was carried out in different rooms, the samples were transported wrapped in delicate task wipes (Kimwipes). This procedure was applied to all the samples tested in this project.

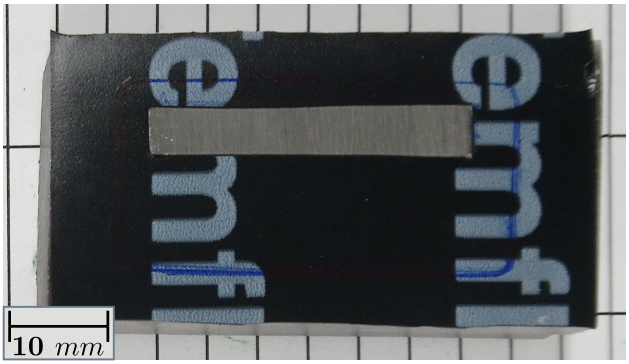

Figure 3.1: A sample of steel from batch 1 displaying the cutout area taken prior to testing.

Testing exposed the polished side of the sample to the electrolyte. To control the amount of exposed area, the polished side of the sample was covered with black electrical tape. Then, a rectangular cutout on the tape exposed only a portion of the total steel surface. This had the additional advantage of doubling the number of tests per sample. For batch one, markings of approximately the same size were traced on top of the tape. The markings were used to perform the cutout with a sharp utility blade. After removing the cutout for testing, the exposed area was calculated by taking the length and width of the rectangular shape with an electronic caliper. However, to improve consistency, a template of dimensions 18 x 6 mm was used to mark the cut-out area in batches two and three. The template for batch 3 was produced out of a piece of silicon carbide paper as it proved to be stiff enough to be constantly reused. An example of a sample from batch 1 is provided in Fig. 3.1.

3.2 Tribometer

All experiments were performed with a reciprocating tribometer. The in-house built apparatus was first designed by Wong [48], and is composed of three linear actuators positioned orthogonally, a rubbing pin, and a multi-axis pressure sensor. The actuators on the base plane are used to position the sample under the pin. During testing, the steel sample is

moved under the pin while the pin is slightly adjusted only on the vertical direction. Together with readings from the pressure sensor, the instrument allows for controlled abrasion and calculation of the friction coefficient. The actuators can be controlled directly by pressing physical switches, or automatically through a Windows 10 computer running LabVIEW™ 2017. The physical switches allow for operation of the linear actuators despite them being disconnected from the computer. The rationale behind this approach is that it allows for the instrument to be manually set into the starting position from which the automated program can take over the experiment. Table 3.1 shows the parameters used in each batch of experiments. A picture of the instrument is provided on 3.2.

Table 3.1: Experimental parameters

Batch Number	**Applied Vertical Force (N)**	**Number of Cycles**
Batch 1	10	1 000
Batch 2	15	3 000
Batch 3	20	1 000

3.2.1 Apparatus

Each linear actuator was acquired from IntelLiDrives as a pre-assembled unit [49]. The units are composed of a movable stage driven by a stepper motor by Arcus Technology. The vertical actuator (z-axis), as well as a horizontal one (y-axis), are stationary on the testing bench. The remaining actuator (x-axis) is mounted over the y-axis and provides the top surface on which the remaining components are attached. This six-axis load sensor, obtained from ATI Inudstrial Automation, is mounted such that its sensing orientations (x,y, and z) are aligned with the positioning of the actuators. Threaded holes on the sensor allow it to be properly aligned and mounted onto the surface of the linear actuator through the use of metallic plates machined with matching threaded holes. Details on the capabilities of the assembly are presented in Table 3.2. The steel sample together with the electrochemical cell assembly are attached on top of the sensor with the aid of an additional intermediate plate.

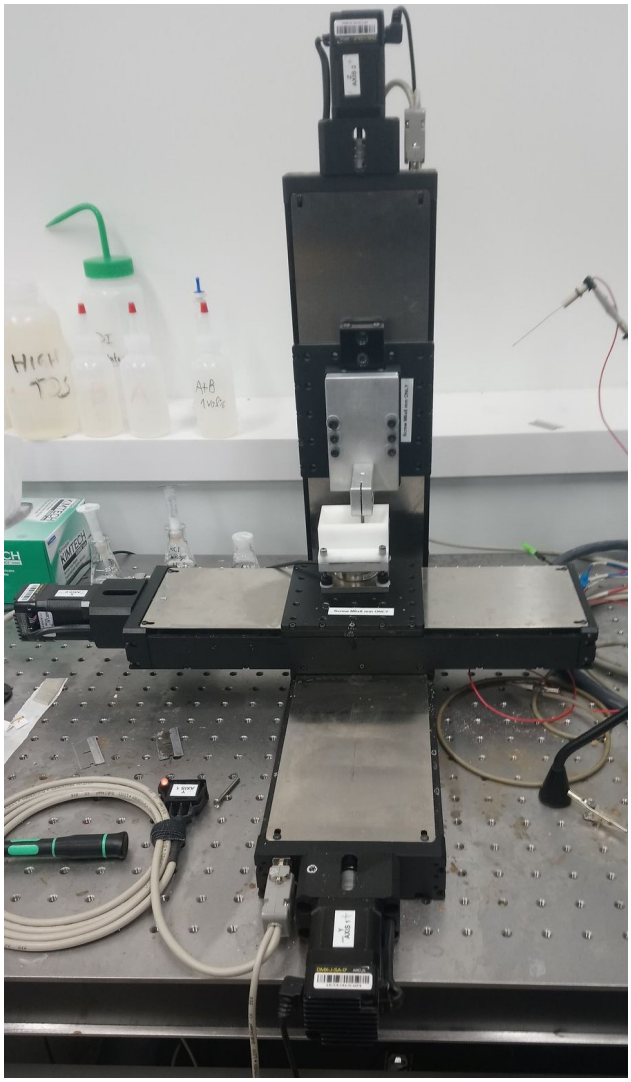

Figure 3.2: Reciprocating tribometer used.

Positioned this way, all reactive forces generated by the rubbing pin onto the steel sample are guaranteed to pass through the sensor.

The vertical actuator features an attachment that holds the pin in place through pressure fitting. This pin presses over the exposed sample during the experiment and is the only contact between the actuator and the sample. The body of the pin is made from a 1/8 in (3.175 mm) plain carbon steel rod. Rod segments were cut every 1.2 in (30.48 mm) for this purpose. The ends of the rod segments were flattened and deburred. Removal of the burr allows for the pin to be inserted into the pin holder; flattening of the pin allows for the attachment of a 6 mm diameter sapphire hemisphere on the other end. The hemisphere was

Table 3.2: Apparatus details

2-3 Stepper motor model	17 DMX-J-SA
Mounting size	NEMA 17
Resolution	3'200 (pulses/rev)
Linear Actuator model	BSMA-LY-140H
Ball screw head	4 (mm)
Repeatability	$\pm$10 (μm)
Load capacity	15 (kg)
Sensor model	ATI Mini40-E
Force range Fx,Fy	$\pm$ 20 (N)
Uncertainty Fx,Fy	1.25%, 1.00%
Force range Fz	$\pm$ 60 (N)
Uncertainty Fz	0.75%

attached using Super Glue manufactured by Gorilla and left to harden for at least one day. Once hardened, the exposed rod section starting at the rod-hemisphere junction and ending just before the other end was coated in off the shelf nail polish (Wet 'n Wild) as a means of electrical insulation in batches 1 and 2. For batch 3, the nail polish was replaced with a rubber coating Plasti Dip® by Performix.

3.2.2 Apparatus Control

The motors are equipped with two digital inputs each. Standalone operation requires that the motor memory is loaded with a script provided by the manufacturer. This script contains an infinite while loop that constantly checks for the state of these two inputs. Pressing the switch grounds the input which is read as indication that the input is activated. As long as the input is activated the motor moves the stage forward in the case of digital input 1 (DI1), and backward in the case of digital input 2 (DI2). This position method was used for all experiments in batch 1.

Thanks to the on-board driver that comes with the motors, low level instructions are not needed to operate them. The overhead required for ramping up and slowing down is automatically calculated. The only inputs that are needed for operation are the desired

operating speed (HSPD), a starting-stopping speed (LSPD), and an acceleration time (ACC) to accelerate or decelerate from one speed to the other. The speeds are specified in pulses per second (pps) and the acceleration in milliseconds (ms). For reference, the values used for stand alone operation in all batches were 20 000 pps, 100 pps, and 250 ms.

Automated operation of the machine was used in all batches to run the experiment under the prescribed conditions outlined on Table 3.1. For batch 1, a pre-existing VI was used to run the experiment. It featured a force control algorithm that takes the average Fz-force over a full reciprocating cycle and used the average to re-position the vertical stage. As a result, slight deviations from flatness in the samples resulted in areas across the scratch surface where the load largely deviated from the average. In addition, it was found that, as the buffer of data increased over the course of the experiment, the force correction tended to considerably lag behind, as demonstrated in Fig. 3.3 (a). There, the normal and lateral forces are portrayed for an uneven steel sample where deviation from flatness was more pronounced towards the right end. First, the instrument adjusted the load such that, on average, the total force over the cycle amounted to 10 N. On its own, this correction can result in higher mechanical wear on the right side of the sample rather than on the left side. Second, due to the increasing delay between processing of data and current cycle, the overall load deviated from 10 N. It should also be noted that, for this arrangement, the horizontal component seems less responsive to flatness variation than the vertical component. Despite these potential issues, this control has been used in previous works and was considered to be adequate enough for batch 1.

In its original form, the VI used the *Frames* feature in LabVIEW. Frames are well suited for programming sequences in which the algorithm follows a linear pattern. However, it was found that this linearity can also prevent the algorithm from being adequately responsive as all subcomponents rely are sequentially interdependent. To address these issues, the VI was rewritten for batches 2 and 3. The approach used for these batches makes use of *state machines*, a programming architecture better suited for separating the experiment into small tasks (states) that can be run depending on input either from within the program or from the

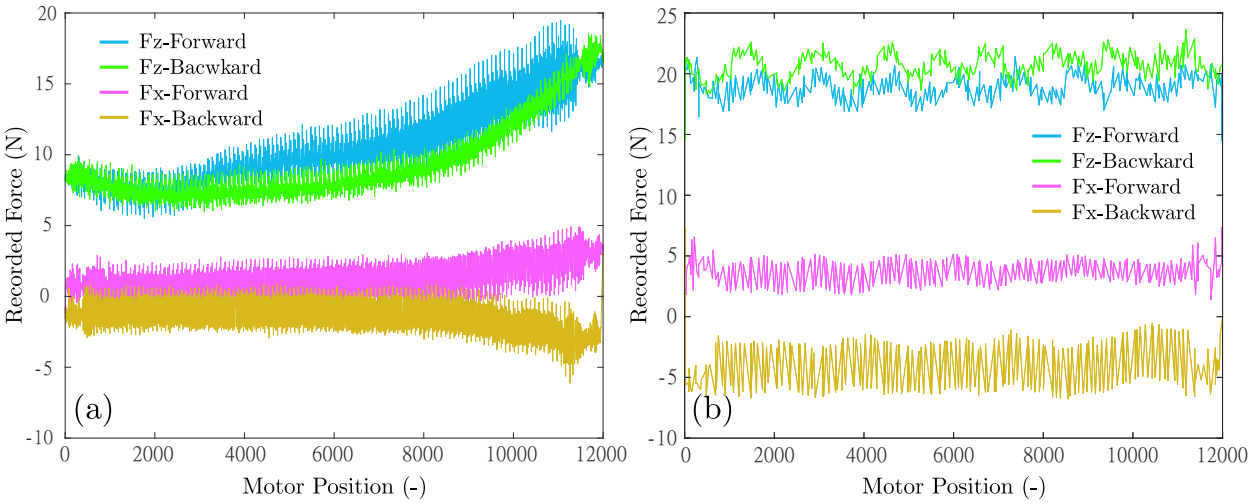

Figure 3.3: Examples of load control effects based on: a) average over a full cycle, and b) PID using recent data points.

user [50]. Furthermore, the overhead tasks of reading the load cell, controlling the motors, and interpreting the data were separated into three corresponding state machines. This separation achieves parallel operation which in turn enables responsiveness despite a busy data queue. Taking advantage of this responsiveness, the load is no longer adjusted based on the average value over a whole cycle. Instead, the control adjusts the load based on information regarding the most recent data points which prevents uneven load application due to deviations from flatness. These feedback is constantly updated thanks to a proportional, integral, and differential (PID) controller available in LabVIEW.

While the most recent approach described above addresses the issues associated with the unresponsiveness on the control side, and unevenness on the sample side, it introduces the issue of additional vibrations. These vibrations are produced by the stepper motor being constantly activated. An example of the interference of these vibrations on the application of vertical load can be seen in Fig. 3.3 (b). Despite the presence of such artifacts, this form of control is considered an improvement. It should also be noted that even small variations on the adjustment of the PID gains were found to produce major overcompensation or under-compensation. The sensitivity was so large that the gains used on a dry sample were not adequate for a sample immersed in electrolyte. As a consequence, the values were tuned

using trial and error. Table 3.3 reports the gains values used for batches 2 and 3.

Table 3.3: PID gains used for batches 2 and 3

K_c	T_i	T_d
0.020	0.100	0.001

3.3 Electrochemical cell

The electrochemical cell assembly for all experiments was composed of the sample holder, a potentiostat, and electrodes. The steel sample holder consists of a bottomless reservoir made of Delrin that was placed on top of the top of the steel sample. The amount of electrolyte used for all batches was approximately 5 mL. Double sided tape was used to seal opening between the walls of the reservoir and the steel sample. Because the tape is used on the surroundings of the testing area and away from the fastening screws, its compliance does not introduce uncertainty to the experiment. For batch 1, the reservoir was cleaned between experiments with acetone followed by rinsing under running water. Starting with batch 2, residual oxide debris were first removed from the reservoir with 6N HCl and thorough rinsing under running water before proceeding as before. A steel sample attached under the reservoir is shown on Fig. 3.4.

3.3.1 Electrochemical Tests and Parameters

Electrochemical measurements were taken with a BioLogic SP-150 potentiostat in a tree-electrode configuration: working electrode (WE), counter electrode (CE), and reference electrode (RE). In this arrangement, WE is the steel sample under study. For batch 1, a Pt mesh and a non-refillable Ag/AgCl reference electrode (model AG/AGCL 30MM by Redox.me) were used as CE and RE respectively. After repeated failures with the non-refillable Ag/AgCl electrode leading to the abortion of several experiments due to machine malfunctioning, the electrode was no longer used in the rest of experiments. Starting with

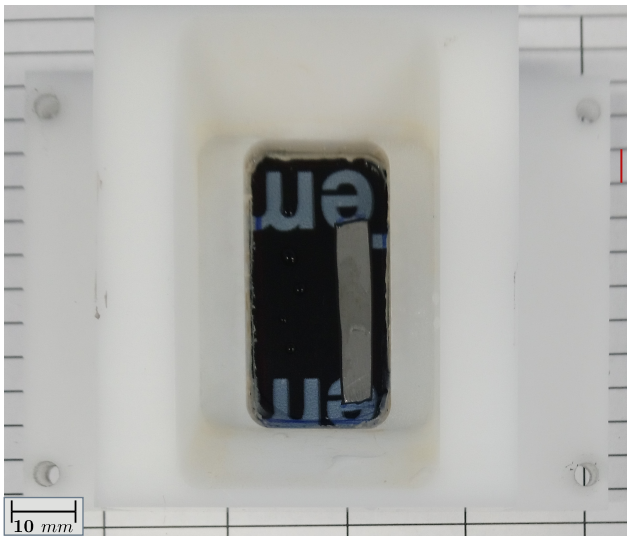

Figure 3.4: Delrin reservoir mounted on a steel sample from batch 1.

batch 2, the CE and RE were replaced with a Pt wire and a refillable standard calomel electrode (SCE) (model RE-4CP by BioLogic) respectively. Proper alignment between the load assembly and the pin, and adequate placement of electrodes were performed in a dry state prior to addition of the electrolyte. The alignment was meant to minimize the degradation of the sample while no measurement was being taken. In this manner, the electrolyte solution was the last component to be added just before running any experiment. After testing, the electrolyte was discarded. The sample was unmounted from the reservoir and rinsed under deionized water (DI-water) followed by ethanol or acetone, compressed air, and stored covered with electric insulating tape for later analysis.

Paralleling the work of Chen et al., the synergism method has been chosen to evaluate level of degradation in this project [51]. As such, four types of electrochemical experiments were conducted to assess the synergism between abrasion and corrosion while following the recommendations proposed on ASTM G119 [39]: T for total wear, W_0 for abrasive wear alone, C_0 for corrosive wear alone, and C_W equivalent to the total corrosive component of T. A resting time was allowed for the system to reach equilibrium prior to running each type of experiment. Based on a prior work by Panda et al. [52], a period of 30 min was chosen for this system. Further details for each experiment type are provided below:

- T: The system was monitored while during sliding. The open circuit potential (OCP) was recorded, and no potential biases were imposed during the length of the test.

- C_0: An initial resting time was used at the beginning of each experiment to enable the system to reach a stable OCP. For batch 1, a linear polarization resistance (LPR) curve was obtained at a continuous potential sweep rate of 0.167 mV s^{-1} (equivalent to 0.6 $\frac{V}{h}$ as recommended by ASTM G59 [53]) in the range ±30 mV with respect to OCP. Likewise, a potentiodynamic polarization curve was obtained at a continuous sweep rate of 0.167 mV s^{-1} (equivalent to 0.6 $\frac{V}{h}$ as recommended by ASTM G5 [54]) in the range of -100 to +1 000 mV with respect to OCP. This latter measurement was used to detect whether a sign of a passive region exists for the metallic coupon, and to calculate the Tafel slopes. Furthermore, the corrosion rate (CR) was calculated from i_{corr} according to Equation 3.1 as taken from ASTM G102 [55]. Here, K_1 is a constant used for unit compatibility ($K_1 = 3.27 \cdot 10^{-3}$ $\frac{mm \cdot g}{\mu A \cdot cm \cdot yr}$ for CR in $\frac{mm}{yr}$), ρ is the density in $\frac{g}{cm^3}$, EW is the equivalent weight "considered dimensionless in these calculations" [55], and i_{corr} is the corrosion current density in $\frac{\mu A}{cm^2}$ approximated from the LPR diagram according to ASTM G3 [56].

$$CR = K_1 \frac{i_{\text{corr}}}{\rho} EW \tag{3.1}$$

The measurement of the linear polarization resistance R_p from the LPR test was conducted according to ASTM G59 [53] through Equation 3.2. Here, i_{corr} is obtained from the Stern-Geary coefficient (B) in V, and the measured resistance (R_p) in Ω· cm^2. The anodic and cathodic Tafel slopes are calculated according to ASTM G3 [56] and are represented by β_a and β_c in units of V [53]. No reciprocating motion was allowed to happen for this type of measurement.

$$\begin{aligned} B &= \frac{\beta_a \beta_c}{2.303(\beta_a + \beta_c)} \\ i_{corr} &= 10^6 \frac{B}{R_p} \end{aligned} \tag{3.2}$$

- W_0: Reciprocating motion was allowed to happen under cathodic protection of -1V with respect to OCP as recommended by ASTM-G119 [39].

Additionally, potentiodynamic electrochemical impedance spectroscopy (PEIS) measurements were taken in batch 3 for a deeper understanding of the system before, during, and after testing. A potential sinusoidal wave was used with amplitude of 10 mV centered at OCP as suggested. A total of 40 points logarithmically distributed were used for scanning in a frequency range from 100 kHz to 10 mHz. These settings are adapted from tribology experiments by Fernandes et al. and Ponthiaux et al. [38, 57]. The total time taken for a single PEIS run with this arrangement was 14 min and 44 s.

In PEIS, the measurements are assessed indirectly by fitting the data to an equivalent circuit. While the possible circuits that can fit the data are not unique, some prior understanding of the system is commonly used to relate circuit elements to physical-chemical processes happening in the cell [58]. The simplest equivalent circuit representing an electrode immersed in solution is know as the Randles circuit portrayed in Fig. 3.5 (a). In the circuit, R_s stand for the solution resistance which means that it captures the effect of the conductivity of the electrolyte. On the upper side of the loop, the capacitance C_{dl} captures the near ideal capacitance associated with the electrical double layer. On the lower part of the loop, the terms R_t in series with Z_W together model the faradaic process [58]. Here, R_t models the charge transfer resistance at the interface, and Z_W the Warburg impedance generally associated with mass transfer [58].

While such a simple equivalent circuit yields a perfect semicircle on the Nyquist plot, the use of inhibitors tends to reshape such pattern. Based on the work of Mansfeld [59], corroding systems in the presence of organic inhibitors can be modeled with the same circuit used for failed coatings on steel. Such modification is given by the equivalent circuit of Fig. 3.5. The addition of C_f and R_f corresponding to the coating film capacitance and coating film resistance respectively. Furthermore, this circuit was chosen to fit the experimental data as it is now commonly used to study inhibitory effects on similar experiments with ferrous

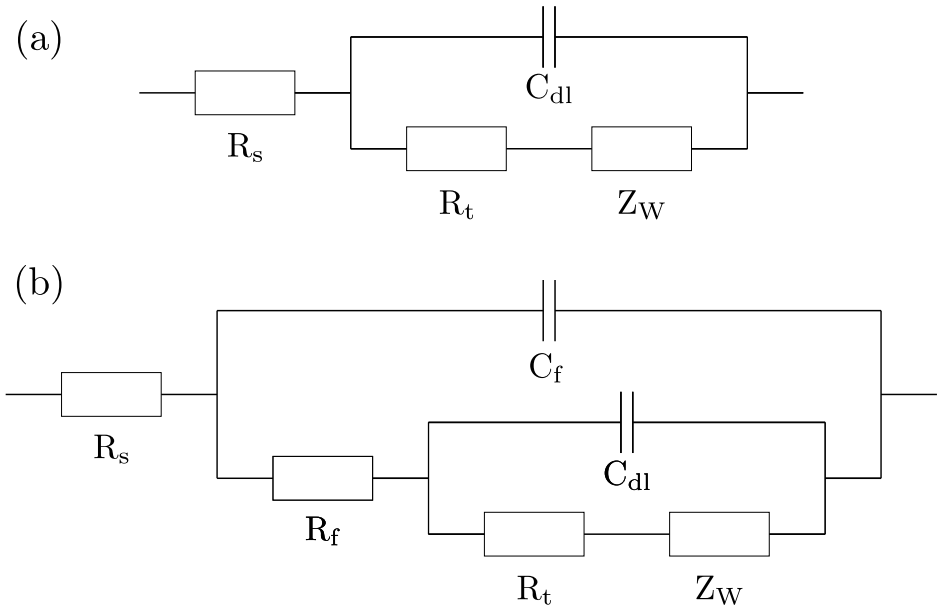

Figure 3.5: Equivalent circuits: (a) Randles Circuit, and (b) Modified Randles circuit for a porous coating.

materials [35, 60–67]. For fitting purposes, it is useful to define the Warburg impedance (Z_W). The specific expression used here is based on the finite length model (the case in which the film thickness is finite) according to Equation 3.3 [68]. Because the Warburg impedance varies with frequency, the equation introduces a couple of constant parameters for fitting purposes. The R_W term which is associated with the limiting diffusion resistance, and the τ_D term known as the diffusion time constant. The rest of the terms corresponding to the angular frequency (ω), and the imaginary number $i = \sqrt{-1}$. Lastly, fitting was achieved through the included software *EC-Lab* through its own implementation of the Simplex algorithm.

$$Z_W = R_W \frac{\tanh\left(\sqrt{i\omega\tau_D}\right)}{\sqrt{i\omega\tau_D}} \tag{3.3}$$

3.3.2 Electrolyte

The electrolyte consisted of water extracted from the field where Calfrac Well Services Ltdconducts hydraulic fracturing operations to which some additive or combination of additives were introduced. The water had a light yellow appearance when looked from a

clear container. Analysis of the water revealed a variety of dissolved ions including chloride, bicarbonate, sodium, and potassium with a count of total dissolved solids of 233 956 mg/L. Due to this latter fact, this liquid is further referred in the present research as HTDS water where HTDS stands for high total dissolved solids. The complete analysis is presented on Appendix A. By internal communication, it was revealed that the additives are added on a volume percent basis during operation. Therefore, this measure of concentration has been chosen for the current study. Likewise, for batches 1 and 3, a total concentration of additives of 0.3 vol% was used as it was also communicated that his concentration corresponds to real values used by Calfrac Well Services Ltd. The concentrations of additives for batch 2 are presented later as the concentrations are based on requirements of the statistical analysis. Due to the small quantity of additives used, in addition to the additives not known to act as either bases nor acids, it is assumed that the properties of the electrolytes remain similar to that of bulk HTDS water. Furthermore, due to the layout of the set up, the electrolyte is also assumed to be stirred and aerated.

3.3.3 Custom Lugging Probe

One concern that arose early on was the isolation of the RE from the solution to prevent cross-contamination. Starting with batch 2, a custom lugging probe was built to interface with the electrochemical cell set up. The probe was built from a 1-40 μm pipette tip bonded to the tip of a 3 mL syringe with epoxy resin (West System 105). A gel prepared from agar-agar (Milipore Sigma) saturated with KCl was used to fill the probe. KCl was chosen as the conducting salt due to its established equivalent ion mobility between potassium and chloride [69]. A mixture of 4wt% agar-agar is often recommended in the literature for similar applications [58, 70–72]. While increasing the concentration of agar-agar results in a firmer gel, it has been reported that the concentration also has the effect of reducing the pore size [73]. This was a concern because [74] has reported that very small pore sizes, around the Debye length of the ions in the electrolyte, could prevent ion mobility due to screening

effects. Therefore, preparations at lesser concentrations were prepared. It was found that at concentrations lesser than 4wt% the gel was too weak to support the RE.

The gel was produced by combining both the powder and salt with DI water (9.9 $\frac{\mu S}{cm}$) in a glass vessel. The top of the vessel was loosely covered aluminium foil to prevent excessive evaporation without raising the internal pressure. Uniform heating was achieved through the use of a secondary container in a water bath arrangement over a magnetic hot plate. The contents were heated above 90°C and left there for at least 5 minutes to ensure complete dissolution of the agar-agar powder. This change could be detected by a change in turbidity of the liquid as it became much clearer at this point. The solution was then allowed to cool to 60°C enough to be safely loaded into the lugging probe. To load the gel, the plunger in the syringe was first raised in the air to approximately one third of its travel length. Then, the tip was immersed in the gel. The plunger was slowly raised to allow for the gel to flow without creating air bubbles. While still immersed, the plunger was removed from the syringe leaving behind the probe half-filled with gel. Finally, the probe was allowed to cool down immersed in a vessel with DI water saturated with KCl for at least one day before usage. This vessel was also used as a storage medium in between experiments. To prevent cross-contamination, the probe was rinsed in DI water and gently wiped with Kimwipes after each experiment.

3.4 Data Processing

At its core, there are two main pieces of information obtained from processing data: friction coefficient, and wear quantification. It has been considered necessary to include this section due to the much more complex nature of these calculations. This is in contrast with Electrochemical data which requires little processing and is mostly reported as obtained from the software provided by the manufacturer of the potentiostat that have been shown previously. Accordingly, the following section introduces and expands on the technical details behind the post-processing of raw data used throughout this study from tracking the evolution of the friction coefficient over time to estimating the amount of removed material from the

steel samples after testing.

3.4.1 Friction coefficient

In its basic form, the friction coefficient (μ) is given by Amonton's Equation 2.1. One needs only divide the lateral force resisting sliding (F) by the normal load (L). This deceptively simple computation hides a large degree of complexity in estimating the friction coefficient of a system in motion. This complexity arises from microscopic imperfections and tilt bias that result in highly uncertain measurements. To address this issue, the procedure used to process the data is based on the works of Shmitz et al. [75], and Burris and Sawyer [76].

Schmitz's work was focused on tribological testing involving low dynamic friction coefficients. The set up was similar to the one used in this work in that it involved a reciprocating pin on disk tribometer. This sort of testing involves taking an average of many data points while the pin and counter surface are being rubbed against each other. The issue arises in that the raw data collected from a system in motion contains a high level of noise to signal ration for the reasons presented previously. For such a situation, Schmitz recommended the use of the standard error to assess the uncertainty of the measurement [75]. It could be argued that the *standard error* artificially reduces the uncertainty as compared to measuring the uncertainty through the *standard deviation*. However, this is appropriate when discussing the uncertainty surrounding the expected mean of a set of measurements according to the ASTM E2655 standard [77, 78] and the ISO Guide for Uncertainty of Measurement [79] where it is referred to as *standard error of the mean* and *experimental standard deviation of the mean* respectively. The expression, as taken from Ref. [79], is reported in Equation 3.4. There, q_k stands for each individual observation, $\bar{q}$ for the mean of observations, n for the

number of observations, and u for the uncertainty.

$$\begin{aligned} s^2(q_k) &= \frac{1}{n-1}\sum_{j=1}^{n}(q_j - \bar{q})^2 \\ s^2(\bar{q}) &= \frac{s^2(q_k)}{n} \\ u(\bar{q}) &= \frac{s(q_k)}{\sqrt{n}} \end{aligned} \tag{3.4}$$

With the uncertainty defined, the next issue is that of hysteresis. During testing it was observed that the loads in the forward direction were consistently different from the loads registered in the reverse direction. Because the load was applied through the PID controller described above, it could be argued that this observed hysteresis was caused by improper tuning of the PID controller. However, this hysteresis in the load was also observed by Burris [76] and Schmitz [75] who attribute it to the misalignment angle. Schmitz first addressed this issue by deriving an expression that is dependent on knowledge of the angle of misalignment. In this respect, Burris improves over Schmitz's work in that he introduced the concept of a reversal technique, a method that "completely eliminates misalignment sensitivity without requiring knowledge of the misalignment angle" [76]. This technique, is presented by Equation 3.5 where, thanks to the elimination of terms, the measured friction coefficient ($\bar{\mu}'$) represents the actual interfacial friction coefficient (μ) of the system. Here, F_X and F_Y stand for the average values of the friction force and vertical load respectively; the subscripts f and r stand for the forward and reverse directions respectively.

$$\bar{\mu}' = \frac{\frac{1}{2}(F_{Xf} - F_{Xr})}{F_{Z(\text{Average})}} = \mu \tag{3.5}$$

Because Equation 3.5 calculates $\bar{\mu}'$ as an average of averaged quantities, the combined standard uncertainty u_c is calculated through the propagation of uncertainty rule presented in Equation 3.6 as suggested by Burris [76]. Here, $u_c(M)^2$ is the combined variance of M, and M is the function composed of individual x_i quantities [79]. For this application, the composed function is the measured average friction coefficient $\bar{\mu}'$, and the composing quantities are the

individual averages of the forces both vertical, horizontal, and in the reverse and forward directions F_i. Equations 3.4, 3.5, and 3.6 were implemented in a Matlab script to calculate the friction coefficients for the experiments. A detailed step by step break down of Equations 3.5, and 3.6 is provided on Appendix B.

$$\begin{aligned} u_c\left(M\right)^2 &= \sum_{i=1}^{n}\left(\frac{\partial M}{\partial x_i}\right)^2 \cdot u\left(x_i\right)^2 \\ u_c^2\left(\bar{\mu}'\right) &= \sum_{i=1}^{n}\left(\frac{\partial \bar{\mu}'}{\partial F_i}\right)^2 \cdot u^2\left(F_i\right) \end{aligned} \tag{3.6}$$

When reading the raw data, the Matlab script identifies each individual reciprocation cycle based on information about the location of the horizontal stage at the time of measurement. This allows for evaluation of the friction coefficient over time. Furthermore, to avoid edge effects at the ends where the motor has variable speed and reverses direction, only a window at the middle of the reciprocating cycle is used for performing calculations. For visualization purposes, Fig. 3.6 shows many pseudo friction coefficients computed using a moving average over the track length during the duration of a test.

Fig. 3.6 shows some change in friction over time. It also shows that the quantities in the window are relatively stable regarding the rest of the reciprocating cycle. By using the data inside this window and processing it according to Equations 3.4, 3.5, and 3.6, it is possible to track the change in friction coefficient over the duration of the experiment. A representation for the same test as in Fig. 3.6 is presented in Fig. 3.7. The corresponding friction coefficient for each cycle is presented with a grey mark. The overall trend is plotted in green using the *Robust quadratic regression* algorithm (rloess) available in Matlab. It can be seen that there is a run-in at the beginning of the experiment where the friction coefficient is maximum followed by a more stable region that extends for the remainder fo the experiment. This behaviour is consistent with results obtained by Schmitz and Burris [75, 76].

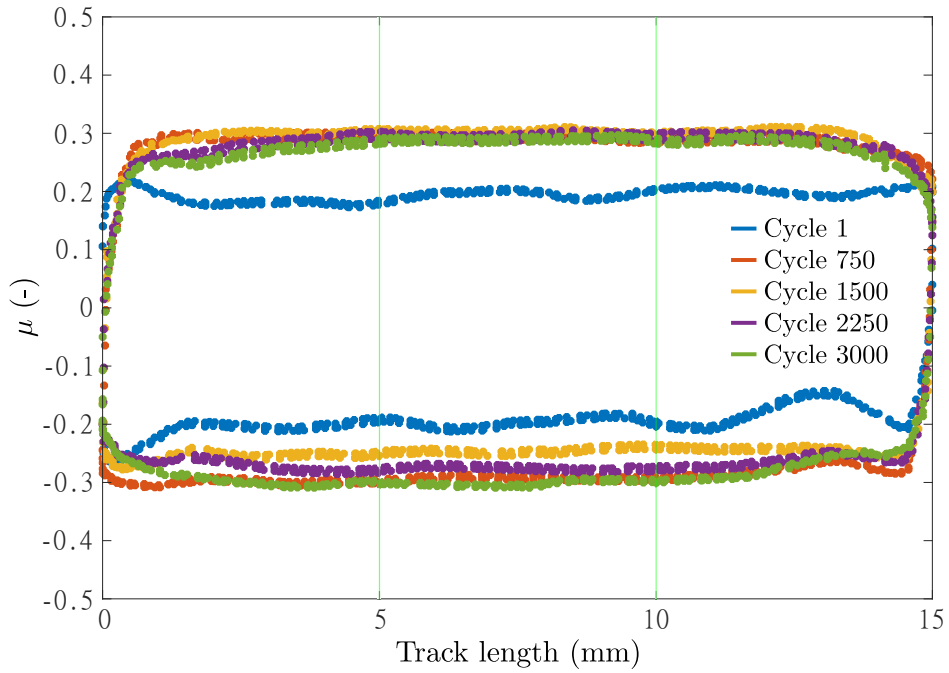

Figure 3.6: Friction loop where the positive and negative data points correspond to the forward and backward direction of reciprocation. A visualization of the window used to trim the ends of the data is shown as the middle section delimited by thin vertical green lines.

3.4.2 Wear Assessment

The issue of wear is ubiquitous for the current work. Previously, in Section 3.3.1, the methods used to estimate the mass lost due to corrosion through CR have been presented. In finalizing the discussion surrounding wear, this section is dedicated to presenting the two techniques used to estimate the amount of material lost based off physical measurements: optical profilometry, and scanning probe microscopy (SPM). By making the assumption that the level of wear is uniformly distributed throughout the length of the wear track, the measurements performed with these techniques over a section of the wear track can be interpreted as representative of the wear track as a whole. This assumption is justified based on the geometric set up of the instrument described Section 3.2.1. Further support for the validity of this assumption was found by carefully performing the measurements described in the current section over several segments of the wear track for selected steel samples.

Assessing wear by these methods makes it possible to obtain an estimate in T and W_0-type of experiments. Taking it all together with the corrosion measurements for C_0-type

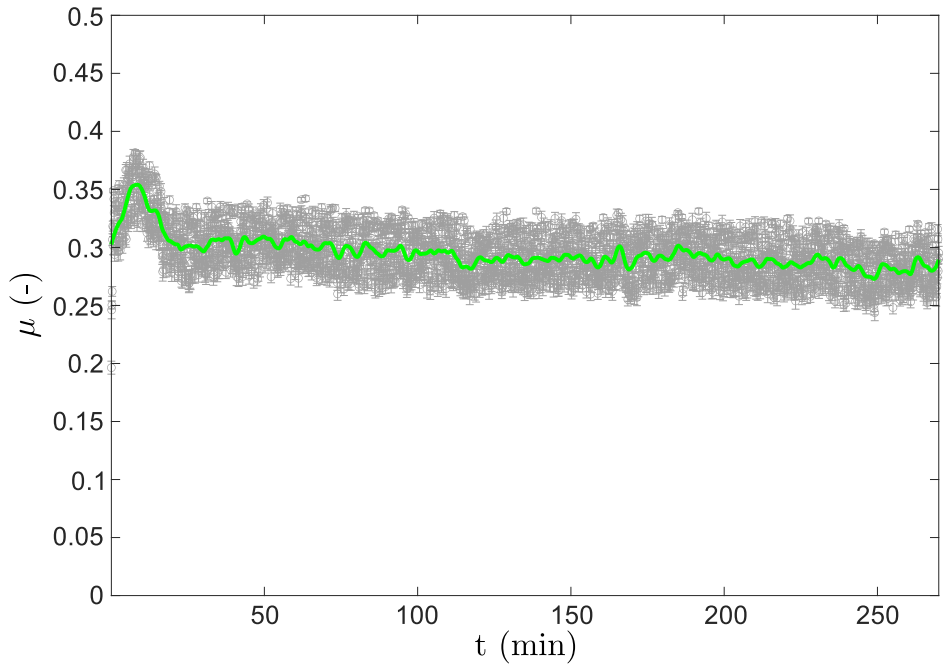

Figure 3.7: Evolution of friction coefficient over the course of a test.

experiments described previously, it is now possible to apply the synergism model as provided in Ref. [39] through Equation 2.2 revisited. The implication of this equation is that if the total measured wear T is greater or lesser than the simple addition of W_0 and C_0, the difference can be explained through the synergism term S. A positive synergism would suggest enhancement of material removal under both conditions; a negative synergism would suggest an antagonistic effect resulting in the protection of the material [39]. Additionally, the terms W_C and C_W are used to separately quantify total mechanical wear in the presence of corrosion and total corrosion in the presence of mechanical wear through Equations 3.7 and 3.8 respectively.

$$T = W_0 + C_0 + S$$
$$S = \Delta C_W + \Delta W_C \qquad \text{(2.2 revisited)}$$

$$W_C = W_0 + \Delta W_C \tag{3.7}$$

$$C_W = C_0 + \Delta C_W \tag{3.8}$$

3.4.2.1 Wear by Optical Profilometry

In optical profilometry, the topographical information of a surface can be obtained by shining a beam onto the surface. The features are then calculated based on the reflection collected by the instrument [80]. A salient feature of this method is that is a nondestructive technique as there is no contact against the sample under study. Measurements for batch 1 were performed using the apparatus Zeta-20 (KLA instruments). To set up the instrument, the cleaned steel samples were placed under the optical lens of the apparatus such that the middle of the wear track was located at the center of the optical view. Then, the height was adjusted so that the surface of the sample was clearly focused. Fig. 3.8 a) Shows a color image of a region of the steel sample under measurement as captured from the accompanying Zeta-20 software. The wear track is seen as darker strip running across the image from the lower left corner to the upper right corner. Through this software, a set of 10 line profiles were taken across the wear track. Each of these profiles are visualized as white lines superimposed over the section of the wear track.

Each line profile contains information about the relative height of the surface features below. A visual representation of these features over the span of the line profiles is provided in Fig. 3.8 b). Notice that in the figure there are also present 4 additional lines orthogonal to the profiles. These lines are used to highlight 2 regions of interest over the span of the profiles. From left to right, the first pair of vertical lines serves to highlight a portion of the steel surface that is know not to have been affected by the abrasion process. It should be understood that the non-affected area extends beyond this region and is also present on both sides of the wear track. The second pair of vertical lines serves to delimit the borders of the wear track where it is understood that all the wear from the abrasion process is located.

Quantification of the worn region was achieved externally to the Zeta-20 software through a Matlab scrip following a method adapted from a previous work by Chen et al. [51]. Specifically, the line profiles were combined into a representative average profile. Using this new profile, a base line was fitted through the unaffected portions to the left and right of the

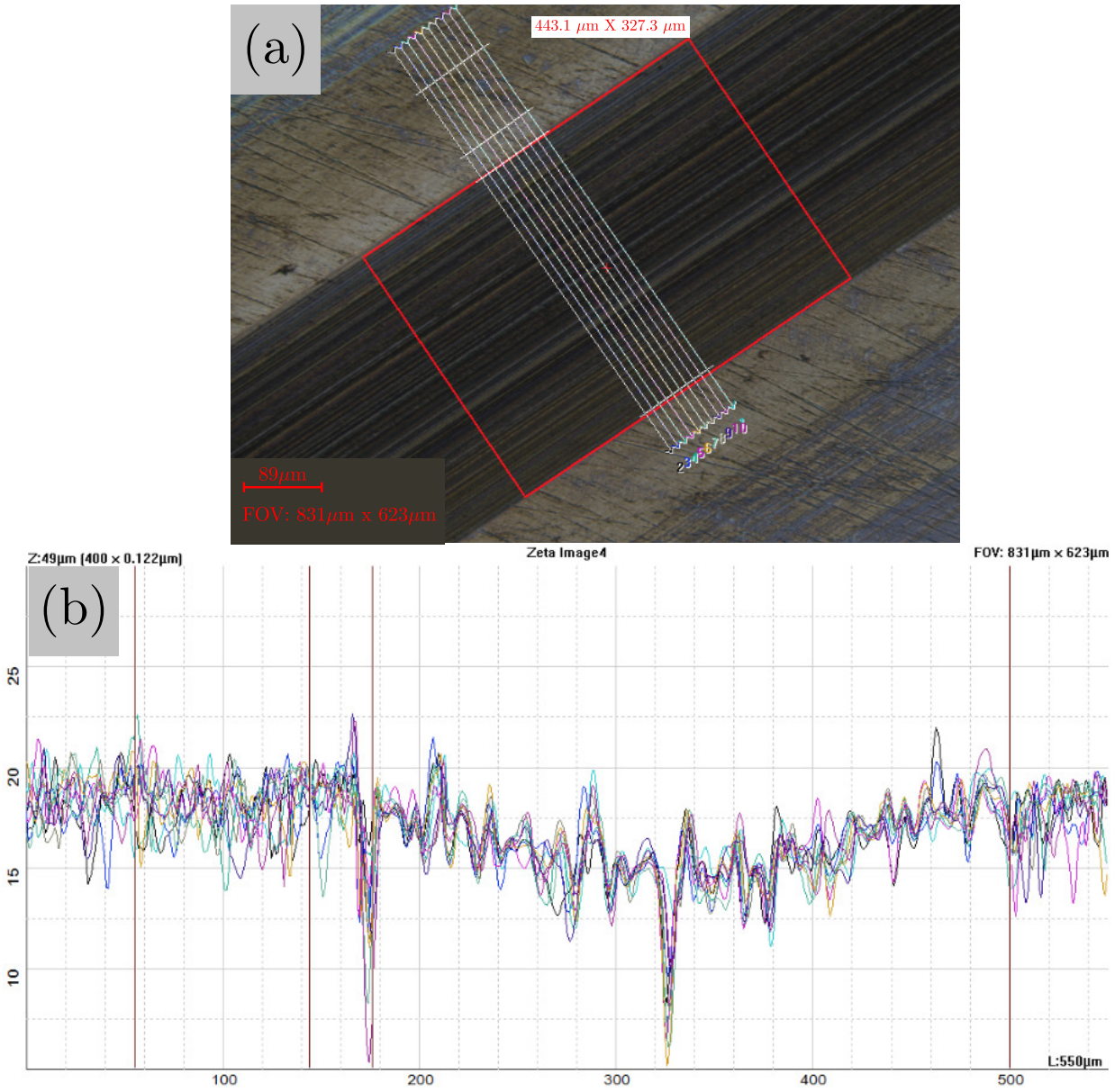

Figure 3.8: Wear track measurement according using Zeta-20 apparatus. (a) A portion of the metallic sample under the optical lens. The wear track is seen as a darker strip running from the lower left corner to the upper right corner. (b) Profiles over the wear track corresponding to the crossing white lines on part (a).

wear track to establish a reference zero position. Then, the area above the wear track curve was numerically integrated through the trapezoid method according to Equation 3.9. In the equation, $h(x)$ represents the height of the features over the length x of the line profile, and 0 and a delimit the start and the end of the wear track region. The result of this numerical integration yielded a representative cross-sectional area A_c of the wear track. The total

volume of the removed material can be easily computed by multiplying this cross-section by the length of the wear track. However, in order for this measurement to be compatible with Equation 2.2 revisited, which uses corrosion rates as calculated in Section 3.2.1, the amount of worn material must be expressed in terms of a penetration rate PR. This computation is achieved by using Equation 3.10 where W stands for the width of the wear track of each sample, and t stands for the time during the experiment over which the reciprocating motion took place.

$$A_c = \int_0^a h\,(x)\,dx \tag{3.9}$$

$$PR = \frac{A_c}{W \cdot t} \tag{3.10}$$

On a final note, a closer examination of the line profiles in Fig. 3.8 b) shows a large level of background noise in the form of sharp peaks and troughs. Based on understanding the reciprocating tribometer described in Section 3.2, it seemed unlikely that the these marked features on the figure could correspond to real physical features on the surface of the sample. After examining supplementary material provided by the manufacturer, it was found that similarly looking artifacts can occur upon depth discontinuities, and boundaries between high contrast areas. While this phenomenon is not usually an issue for typical samples measured with this instrument, it is likely a contributor to the exacerbated surface roughness of the steel samples in the present study where the wear track presents both, a marked difference in contrast between the wear track and the surrounding material, and several depth discontinuities in the form of grooves running along the wear track. A demonstration of such optical artifacts is provided in Appendix C where a sample of known topology was examined. The presence of these artifacts motivated the use of SPM described in the following section for the remainder of the study.

3.4.2.2 Wear by Scanning Probe Microscopy (SPM)

Looking to address the issue of optical artifacts in the measurement of material loss, scanning probe microscopy (SPM) replaced optical profilometry entirely for batches 2 and 3. In SPM, a probe is swept over the surface under study while keeping close physical contact. Along the travel of the probe, the upward and downward displacements are recorded. Later, this information is used to reconstruct a topographical map of the surface. The instrument used in the present work is a nano-indeter TI Premier (by Brüker). A feature of this indenter is that it allows the user to construct a topographical image of the indented surface through SPM. Using this instrument introduces two challenges: first, the maximum scan area is a square of 77 μm per side. Due to this limitation, SPM was used during batch 1 only for the purpose of scanning the bottom of the wear track complimenting the optical profilometry method described above. Second, the range of the probe is limited to a total vertical displacement of 5 μm. The first challenge means that the instrument can only capture portions of the wear track that, according to Fig. 3.8 a), can be as wide as approximately 327 μm in width. The second challenge implies that any surface feature higher than the allowed displacement of the probe could result in damage to the sample or to the instrument, while a feature lower than the displacement would be left undetected.

Just like before, addressing the first challenge requires post processing through an external Matlab script. This was made possible because due to the ability of the instrument to export raw data in plain ASCII format in addition to its default proprietary encoding. Through careful programming, the instrument was set up to scan adjacent areas across the wear track. As a result, several files were generated for every single steel sample. Best results were obtained when setting the probe sweep rate to 180 μm/sec with a contact force of 10 nN and the gain adjusted to 480 units. When the files were combined together in the script, it was possible to obtain a topographical composition larger than the width of the wear track. This procedure offers the added benefit that, by scanning single portions of the wear track at a time, it is possible to scan at a larger depth than the allowed physical displacement of

the probe provided that the wear track gradually deepens as opposed to being an abrupt discontinuity between the highest point somewhere in the surrounding surface and the lowest point at the center of the wear track. Fortunately for this study, the former is the case and, as such, the second challenge is indirectly addressed. As a comparison, Fig. 3.9 shows topographical maps as taken through optical profilometry and SPM for the same steel sample.

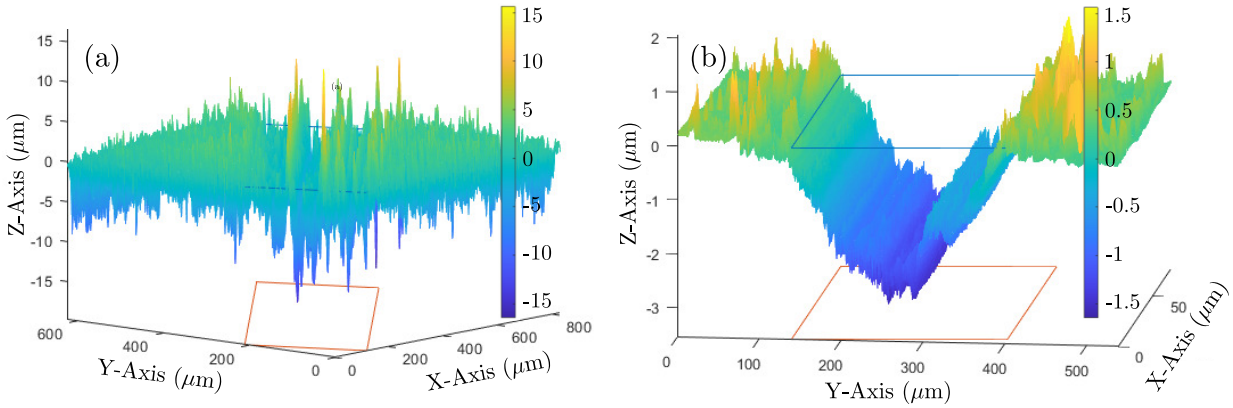

Figure 3.9: Comparison between topographical maps of the wear track on the same sample of steel. a) Topography obtained from optical data. b) Topography obtained from SPM data.

Because producing these maps made use of all the data captured by the instruments rather than just the profiles of the cross-sections, it presented an opportunity to calculate the amount of wear in a more comprehensive manner. Portrayed in the maps of Fig. 3.9 there are two rectangular regions suspended in space. These areas serve to highlight the borders of the wear track. The blue lines are coplanar to the plane of best fit of the surface on each side of the wear track that represent the reference zero position. The red lines are a projection of the blue lines on the base plane to aid in the visualization of the 3-dimensional region under study.

In constructing the rectangular regions, the edges of the wear track are first visually identified to ensure that the borders of the rectangular region overlap exactly with the edges of the wear track. This is achieved by manually highlighting a clear portion of one border and placing a dot on the other. The script then extends the lines all the way to the edge of the image to capture as much information as possible. Then, the remaining two orthogonal lines are drawn as to guarantee that the quadrilateral region is a perfect rectangle aligned with

the wear track. Performing the measurements in this manner also takes care of correcting any misalignment due to positioning of the steel sample. An example of the procedure is found in Fig. 3.10 which represents an intermediary step in generating the topographical map in Fig. 3.9 a).

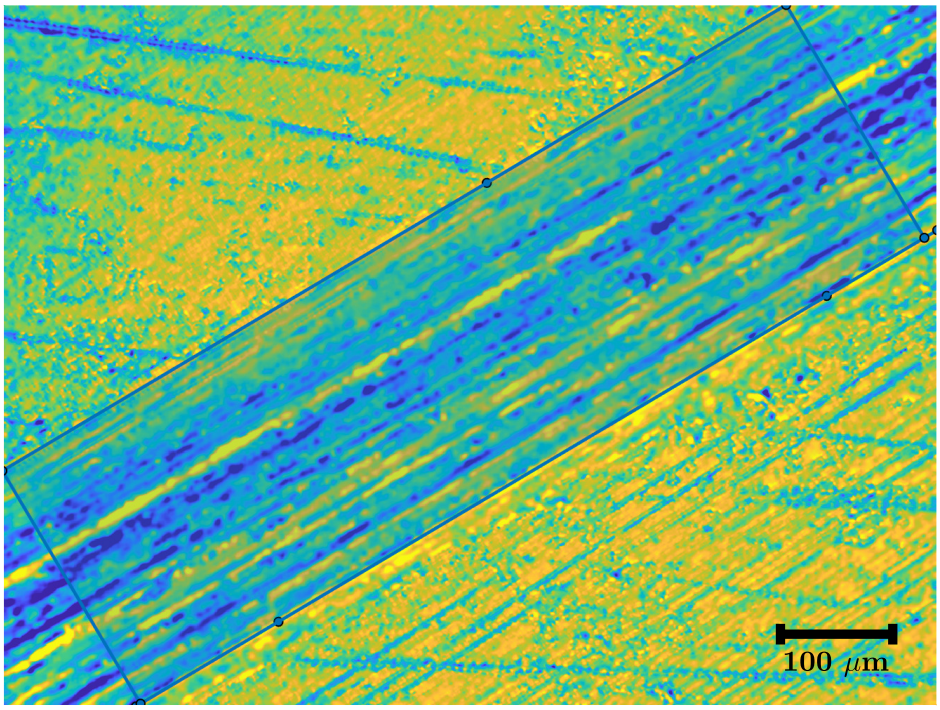

Figure 3.10: Illustration of the construction of the rectangular region.

The calculation once again takes advantage of the assumption of uniform wear over the length of the wear track. Unlike in the line procedure in the previous section, this approach evaluates the quantity of material lost over the entire rectangular region according to Equation 3.11. There, d stands for the average depth per pixel inside the region, A_p stands for the spacial resolution of each pixel or the projected surface area that corresponds to a single pixel, N_p stands for the number of pixels counted inside the region, and L_r stands for the length of the region parallel to the wear track. Since no optical imaging is involved in batch 2, the word pixel here is used loosely to refer to each data point in the topographical map generated by SPM. The result of this calculation could be considered as a representative cross-sectional area of the track similarly to the result of the line profile method. However, since no actual cross section profile is used in this case, it is more appropriate to refer to it

a linear wear volume W_L which has units of volume per length ($\frac{\mu m^3}{\mu m}$ or simply μm^2). The results of this calculation for batch 2 are reported on the last column of Table 3.4.

$$W_L = \frac{d \cdot A_p \cdot N_p}{L_r} \tag{3.11}$$

3.4.3 Optimization of Additive Combinations

The total amount of additive in solution up to this point has been set to 0.3 vol%. However, it is worth exploring whether different volume fractions, and ratios of additive mixtures could be the most effective at reducing the amount of wear in the sample. Finding such optimal combination is an issue of optimization and is the core of experimental batch 2. One method to explore the combinatorial space while incurring in the least number of experiments is the response surface methodology (RSM). The RSM has been selected both for its experimental efficiency, and due to its validated usage in research regarding testing of additives in the context of corrosion [81–83].

RSM is an optimization technique that represents the response in the form of an n-dimensional hypersurface in an (n+1)-dimensional space corresponding to an n number of factors [84]. The curvature of this hypersurface is then used to identify regions of global minima or maxima which consequently minimize or maximize the response. RSM achieves this by means of a polynomial regression in conjunction with the incorporation of statistics to analyze the degree to which the results are significant. In keeping with the usual convention, the confidence interval has been set to 95% which is equivalent to a P-value of 0.05. In this context, the response to minimize is the wear of the pipeline steel, and the factors or variables are each of the three additives under study.

The specific form of RSM used in the present document is the face-centered Central Composite Design (CCD). In CCD, the factors are taken in two levels representing the maximum and minimum settings plus a center point in between them, and two extreme points per factor. Each of these experimental points is referred to as a treatment combination

(tc) [85]. The number of tc's can be expressed through Equation 3.12 where k stands for the number of factors, as adapted from [85].

$$\text{Number of tc's} = 2^k + 2 \cdot k + \text{number of center points} \tag{3.12}$$

In processing the factors, the maximum and minimum values in each factor are standardized to $+1$ and -1 abbreviated as $+$ and - respectively. This step is performed to take in physical units X and transform them into dimensionless design units X_{UD}. Equation 3.13, as taken from [85], is used to perform this transformation where X_{hi}, X_{lo}, and $\bar{X}$ represent the highest, lowest, and their average respectively.

$$X_{DU} = \frac{X - \bar{X}}{\left(\frac{X_{hi} - X_{lo}}{2}\right)} \tag{3.13}$$

Once the higher and lower limits of the design have been established in design units, the extreme values are determined through the α-value. The α-value is a scalar number in design units that determines how far from the center point the tc is positioned. A visual representation of all the tc's in a three-factor CCD is presented in Fig. 3.11. In the present case of the face-centered CCD, the α-value is taken as 1 so that the the extreme points are located at the center of each face of the experimental cube. The reasoning behind such approach is that the range of combinations is limited in that 0 vol% is the lowest amount of additive that can be tried while 1 vol% is approximately as much additive as can be added before the additives segregate out of solution.

The tc's in Fig. 3.11 are abbreviated using lower case symbols. This corresponds a labeling convention referred to as Yates order. Yates order is used here because each combination of lower case letters uniquely identifies a tc regardless of the actual order in which the experiments are conducted. This is important as the order in which the experiments were conducted was randomized. Randomizing the order of experiments achieves eliminating systematic sources of variation by making them appear randomly distributed [85]. As such,

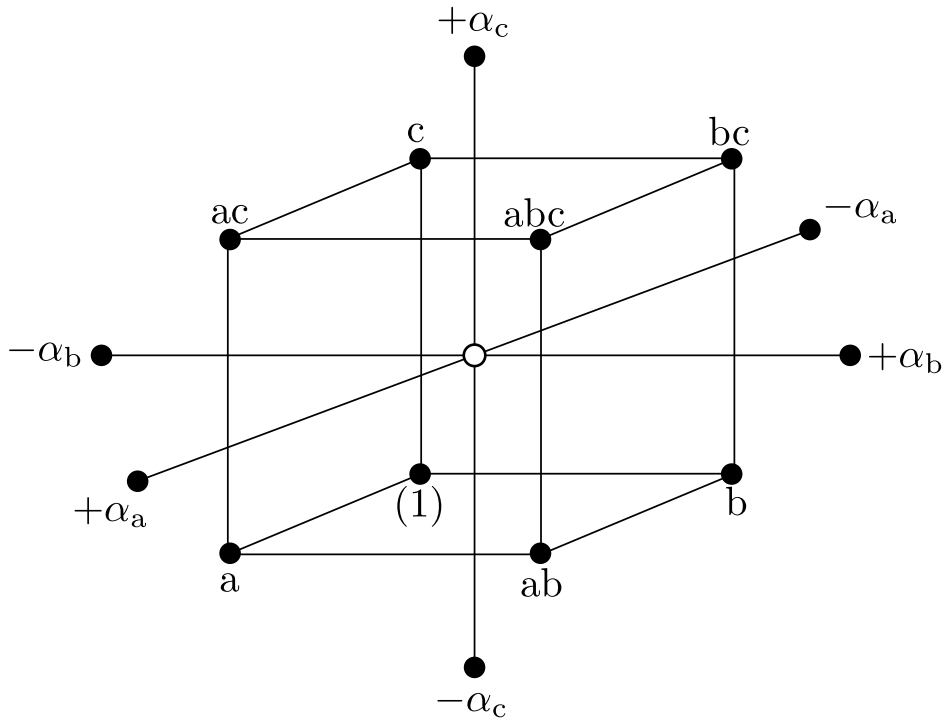

Figure 3.11: 3-dimensional representation of the Face-Centered Central Composite Design labeled in Yates order. Based on [85].

the final design for the current experiment is summarized in Table 3.4. There, the additives have been abbreviated as follows: Dynarate 6524 (A), DWP 621-1 (B), and CalGuard 3100 (C). Notice that the total number of tc's is 20 as there are 6 replicates of the zero center point. This is commonly done to increase the certainty in the results [85]. Lastly, the response (Wear) as measured from the experiments is presented on the last column of Table 3.4. Details on how this response was measured are presented in the following section.

Optimization is possible by constructing a mathematical model that best fits the response. In the case of a three-factor CCD, the model is given by a quadratic polynomial equation that can be thought of as representing a 3-dimensional surface in 4-dimensional space (3 dimensions per factor + 1 dimension corresponding to the response). The template for such mathematical model is presented in Eq. 3.14. Here the response is given by the function y while the coefficient b_0 correspond to the intercept that fixes the hypersurface, and b_i and b_{ij} are the regression coefficients corresponding to the expected change per regression variable. The terms X_i, X_i^2, and X_iX_j are the regression variables that quantify the effect of

Table 3.4: Face-centered CCD experimental design for batch 2.

Stdandard	**Yates**	**Design Units**			**Physical Units [vol%]**			**Wear**
Order	**Order**	**A**	**B**	**C**	**A**	**B**	**C**	$[\mu m^2]$
1	(1)	-	-	-	0	0	0	693.94
2	a	+	-	-	1	0	0	242.79
3	b	-	+	-	0	1	0	457.07
4	ab	+	+	-	1	1	0	381.39
5	c	-	-	+	0	0	1	800.63
6	ac	+	-	+	1	0	1	498.97
7	bc	-	+	+	0	1	1	772.68
8	abc	+	+	+	1	1	1	864.48
9	$-\alpha_a$	-	0	0	0	0.5	0.5	835.37
10	$+\alpha_a$	+	0	0	1	0.5	0.5	678.37
11	$-\alpha_b$	0	-	0	0.5	0	0.5	403.99
12	$+\alpha_b$	0	+	0	0.5	1	0.5	628.92
13	$-\alpha_c$	0	0	-	0.5	0.5	0	543.41
14	$+\alpha_c$	0	0	+	0.5	0.5	1	862.05
15	zero	0	0	0	0.5	0.5	0.5	509.77
16	zero	0	0	0	0.5	0.5	0.5	685.95
17	zero	0	0	0	0.5	0.5	0.5	489.55
18	zero	0	0	0	0.5	0.5	0.5	601.00
19	zero	0	0	0	0.5	0.5	0.5	603.06
20	zero	0	0	0	0.5	0.5	0.5	701.07

each factor alone, with itself, and their two-way interactions respectively. Lastly, the term ε captures the error in the model [86].

$$\begin{aligned} y =& b_0 + \sum_{i}^{k} b_i X_i + \sum_{i=1}^{k} b_{ii} X_i^2 + \sum_{i=1}^{k-1} \sum_{j=i+1}^{k} b_{ij} X_i X_j + \varepsilon \\ y =& b_0 + b_1 X_1 + b_2 X_2 + b_3 X_3 + b_{11} X_1^2 + b_{22} X_2^2 + b_{33} X_3^2 + \\ & b_{12} X_1 X_2 + b_{13} X_1 X_3 + b_{23} X_2 X_3 + \varepsilon \end{aligned} \tag{3.14}$$

Chapter 4

Results

This chapter contains the information for each batch of experiments. The information is accordingly reported into its own subsection. A discussion for each of these subsections is likewise provided. As a shorthand, the names of the additives in the present chapter will, on occasion, be represented as Dy for Dynarate 6524, Dw for DWP 621-1, and C for CalGuard 3100. Furthermore, the letters A, B, and C respectively are also used respectively in keeping consistency with Table 3.4. Ultimately, these abbreviations are used in lieu of the full name of the additives where doing so would result in obscure text.

4.1 First batch: overall additive effects

The kinetic coefficient of friction (COF) is reported in Fig. 4.1 for T-type tests where no external potential or current was applied to the steel sample. Each line represents the medium in which the test was conducted. This includes solutions prepared with one or more additives as well as pure HTDS (H) and DI-water (D). The number of reciprocating cycles is represented on the abscissa with each individual cycle lasting approximately 5 s. The ordinate displays the COF values which are dimensionless as they represent a ratio between the lateral and normal forces. At the onset of rubbing, the COF is erratic for approximately the first 100 cycles for all the tested media except for pure H which becomes stable after

approximately 500 cycles, or the latter half of the duration of the experiment. The plot shows that almost all of the solutions tested, including D, result in roughly thee same COF over time. Remarkably, after achieving stability, the COF for pure H is much larger than the COF for all of the other media. The second greatest outlier is the solution composed of Dw and C additives into H which remains higher than the rest despite achieving stability early on during the experiment.

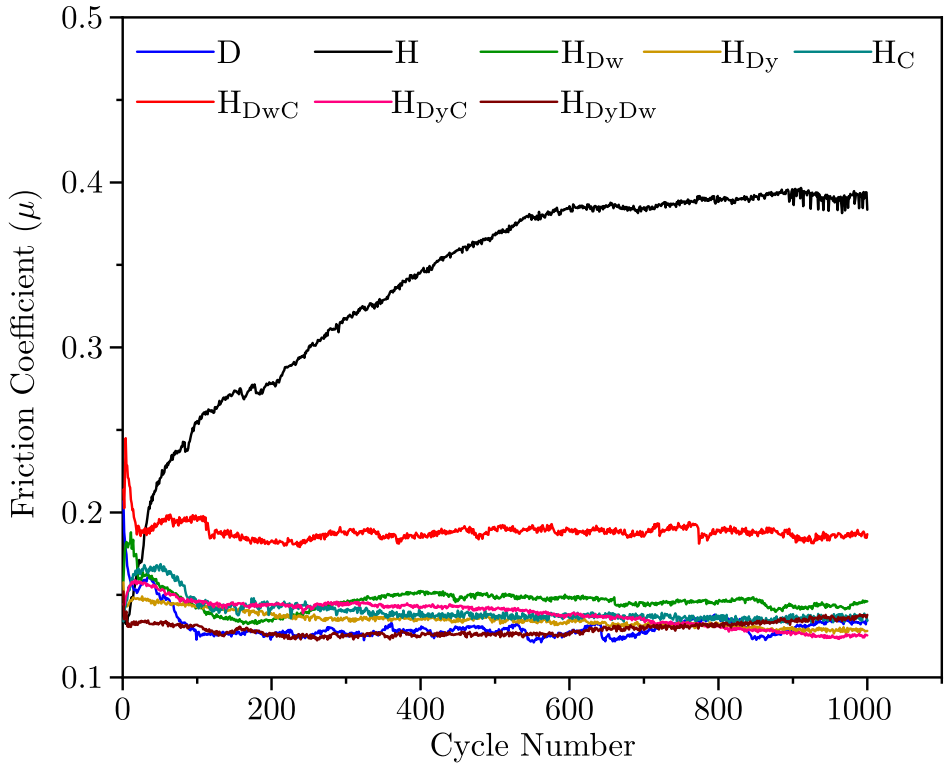

Figure 4.1: Kinetic Coefficient of Friction (COF) measured over the course of T-type experiments. Each colour represents a different testing medium where D stands for DI-water and H stands for HTDS water. The subscripts, where present, indicate the additives in solution. Originally published on [1].

The kinetic coefficient of friction (COF) is reported in Fig. 4.2 for W_0-type tests (Section 3.4.2) where cathodic protection was applied for the duration of the experiment. Similarly to Fig. 4.1, a region of instability can be observed lasting no more than the first 100 cycles. However, after achieving stability, it differs in that the figure shows a tighter grouping of COFs for the W_0-type tests. Although less marked, the black trace, representing the pure H medium, still exhibits a later onset of stability although not as delayed as in the T-type

case. Likewise, pure H still results in the largest COF among that of all the other media. Regarding the rest of the traces, a general tendency towards higher COF values than before is observed.

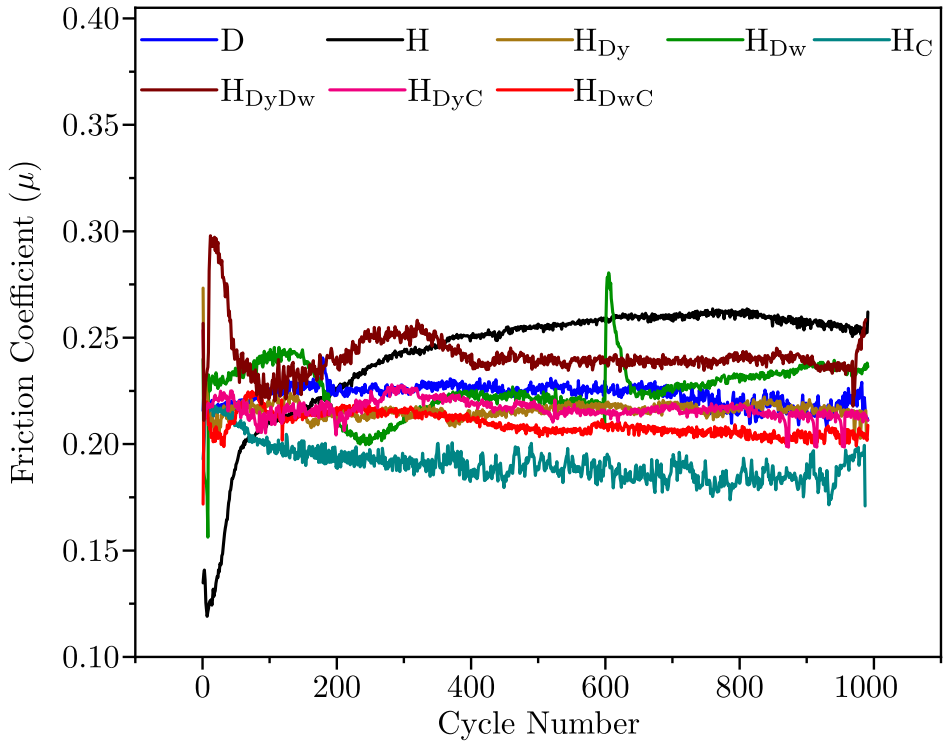

Figure 4.2: Kinetic Coefficient of Friction (COF) measured over the course of W_0-type experiments. Each colour represents a different testing medium where D stands for DI-water and H stands for HTDS water. The subscripts, where present, indicate the additives in solution. Originally published on [1].

The open circuit potential (OCP) recorded during T-type experiments is presented in Fig. 4.3. Each color coded line represents the electrolyte used for each test. The ordinates show the recorded potential in V with respect to the Ag/AgCl reference electrode. Fig. 4.3 shows a general tendency towards a decrease in the initial potential for all samples on the onset of rubbing. Later on the potential remains mostly constant for all electrolytes. Fig. 4.3 shows the OCP potentials recorded during T-type experiments. Fig. 4.3 shows on the onset of rubbing, there is a general tendency towards a decrease in the initial potential for all samples. The potential then remains mostly constant for the remainder of the experiment. Most of the electrolytes result in potentials clustered around a region at approximately -0.6

V. The greatest outliers here are the pure electrolytes D and H represented in blue and black respectively. D shows the most electroposive potential out of all the samples while H shows the most electronegative in this type of test.

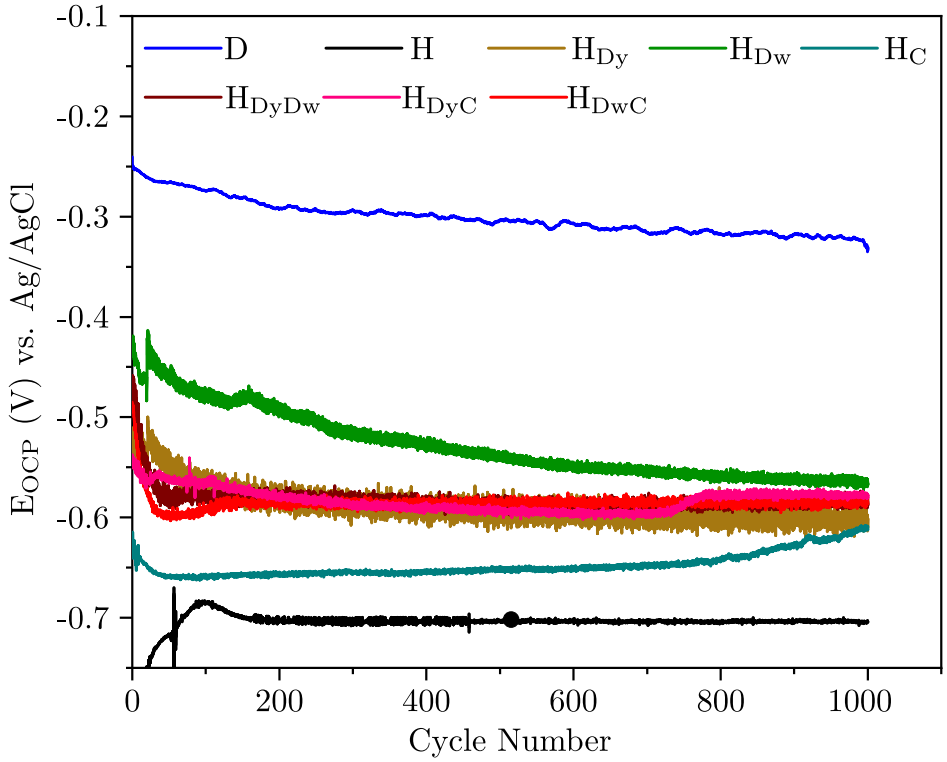

Figure 4.3: Open circuit potential OCP for steel samples undergoing reciprocating abrasion under several electrolytes. Each colour represents a different electrolyte where D stands for DI-water and H stands for HTDS water. The subscripts, where present, indicate the additives in solution. In the figure, 1000 cycles is approximately equivalent to 90 minutes. Originally published on [1]

The potentiodynamic polarization curves for the steel samples immersed in varied media are presented in Fig. 4.4. Displayed on the abscissa is the common logarithm of the current in mA while the ordinates display the working electrode potential E_{WE} in V with respect to the Ag/AgCl reference electrode. The polarization curves show a linear Tafel behaviour near the corrosion potential in all cases. However, as the potential is raised towards more electropositive values, the current increases in a non-linear trajectory. As the potential keeps increasing beyond -0.1 V, the current becomes rather constant and is even seen to slightly decrease in magnitude before returning to its highest value towards the upper end of the

graph. Similarly to OCP, the corrosion potential is highest for D and lowest for H with all the solutions containing additives centered in a cluster in between these two extremes.

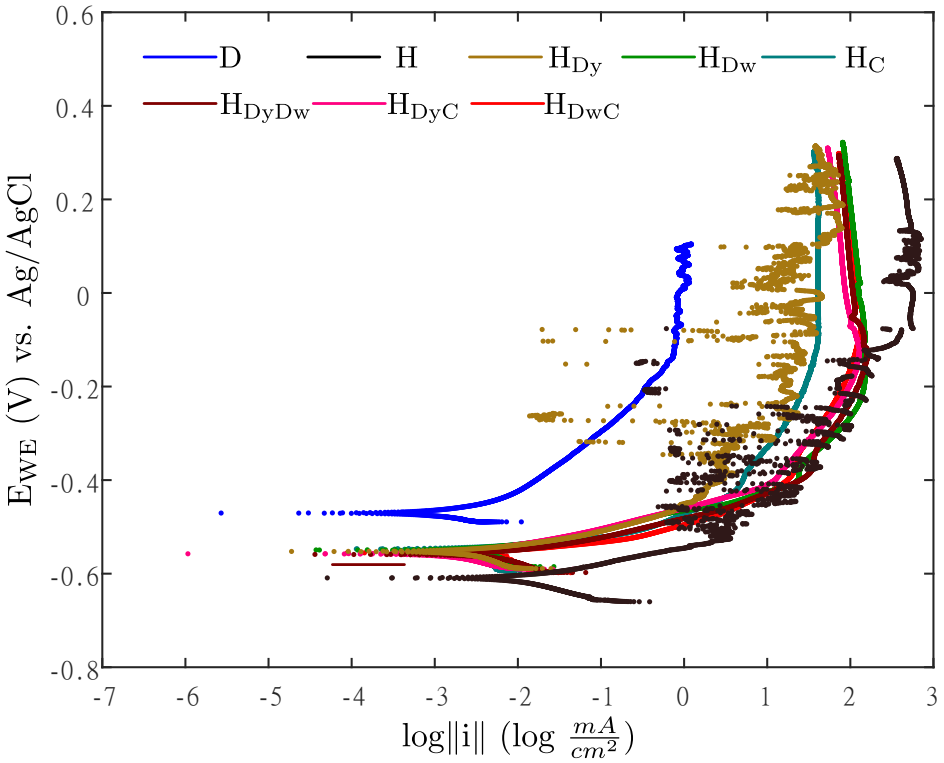

Figure 4.4: Potentiodymaic polarization curves. Originally published on [1].

Regarding the amount of material lost, Fig. 4.5 shows the a graphic comparison between the total wear and the independent mechanical and chemical contributions to the material degradation in different media. For all samples except D, the total amount of wear from T-type experiments is vastly greater than the simple addition of wear from C_0-type and W_0-type experiments. Across all samples, the individual contribution of corrosion to the wear loss rate from C_0-type experiments is much lesser than that from the other two. The case of D is the only occurrence where measurements from both T-type and W_0-type experiments are in relative agreement with each other with the contribution from C_0-type experiments being the lesser in the whole set.

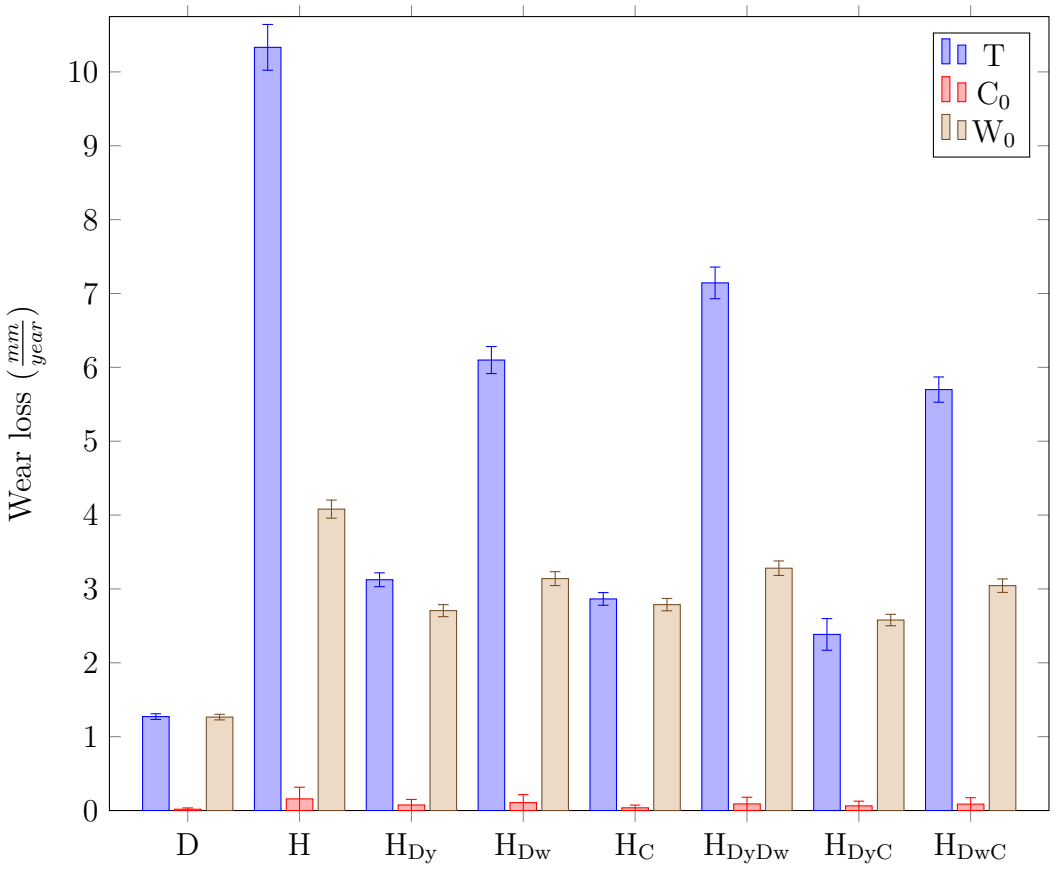

Figure 4.5: Results from batch 1. Hhe electrolytes used are portrayed as follows: D for DI water, and H for HTDS water. The additives are represented by subscripts as follows: Dy for Dynarate, Dw for DWP, and C for CalGuard. The wear conditions are represented as follows: T for normal conditions, C_0 for corrosion wear only, and W_0 for abrasion under cathodic protection. Originally published on [1].

4.1.1 Discussion

The significance of Figs. 4.1, 4.3, and 4.4 lies in the shared pattern across the COF and the measurements of potentials in which the results for all electrolytes are bounded between those produced in the presence of D electrolyte and H electrolyte respectively. To understand this pattern, let us first lay out features of the environment and the involved.

Fist, a look at the corrosion of steel in an oxygenated aqueous environment. In such an environment, the degradation of the metal occurs via an electrochemical process. On the surface of the steel, active anodes spontaneously form where the iron is continually oxidized

according to the anodic half-cell reaction

$$\mathrm{Fe} \rightarrow \mathrm{Fe}^{2+} + 2\mathrm{e}^{-}. \tag{4.1}$$

At the same time, the coupled cathodic half-cell reaction takes place at cathodic sites on the surface of the steel. The electrons liberated by the anodic reaction, as shown in Equation 4.1, are consumed to reduce dissolved oxygen in a process commonly referred to as oxygen depolarization as follows.

$$\frac{1}{2}\mathrm{O}_2 + \mathrm{H}_2\mathrm{O} + 2\mathrm{e}^{-} \rightarrow 2\mathrm{OH}^{-}. \tag{4.2}$$

While iron is readily available in the anodic sites, the cathodic reaction is limited by the availability of dissolved oxygen. Because both reactions are coupled, oxygen depolarization becomes the limiting step and therefore controls the rate of the reaction. Taken together, the overall reaction yields ferrous hydroxide as follows.

$$\mathrm{Fe} + \mathrm{H}_2\mathrm{O} + \frac{1}{4}\mathrm{O}_2 \rightarrow \mathrm{Fe}\left(\mathrm{OH}\right)_2. \tag{4.3}$$

Once formed, the ferrous oxide ($\mathrm{FeO}{\cdot}n\mathrm{H}_2\mathrm{O}$) or ferrous hydroxide [$\mathrm{Fe(OH)}_2$] forms a thin surface film that decreases the rate at which dissolved oxygen can reach the underlying metal. The exposed part of the film can be further oxidized in the presence of oxygen into ferric hydroxide

$$\mathrm{Fe}\left(\mathrm{OH}\right)_2 + \frac{1}{2}\mathrm{H}_2\mathrm{O} + \frac{1}{2}\mathrm{O}_2 \rightarrow \mathrm{Fe}\left(\mathrm{OH}\right)_3. \tag{4.4}$$

Before continuing, it should be clarified that the fundamentals exposed above, including Equations 4.1 through 4.4, have been summarized from Ref. [87]. These two oxides of iron can be easily distinguished by their colour. Ferrous hydroxide is normally found as a greenish or greenish-black substance due to incipient oxidation. By contrast, the common orange to reddish brown colour associated with rust is characteristic of ferric hydroxide [87–90]. In handling the samples it was noticed that no orange colour was visible on them across all types of experiments including at the end of C_0-type experiments where the potential was maintained at high levels for an extended period of time. Instead, a liquid black substance was detached from the samples every time at the end of the experiments. This layer would quickly

turn vivid orange upon exposure to air which suggests that the latter oxidation reaction to $Fe(OH)_3$ given by Equation 4.4 is not an influential factor in the current discussion.

In the absence of additives, the baseline corrosion potential of the immersed steel is given by DI water (D electrolyte in Figs. 4.3 and 4.4). At this potential, the steel is actively being corroded. However, it is also limited in that the low conductivity of pure water results in the short range coupling between the anodic and cathodic sites. The close proximity of these sites enables the formation of an adhesive film of ferrous oxide according to Eq. 4.3 that acts as a diffusion barrier to the dissolved oxygen species [87, 91].

Moreover, the presence of ions in the electrolyte H promotes corrosion in two steps. First, the increased conductivity of the water enables the formation of anodic and cathodic sites further apart from each other. Second, because the half-cell reactions given by Eqs. 4.1 and 4.2 are separated, their products generate Na(OH) at the cathodes and $FeCl_2$ at the anodes [87, 92]. Only when these later products diffuse away from their original sites can they react to form $Fe(OH)_2$ in solution. However, because this last reaction occurs away from the steel surface, $Fe(OH)_2$ is no longer adherent and can no longer form an effective diffusion barrier [87]. Simultaneously, the Cl^- ions penetrate into the hydroxide layer compromising the diffusion barrier in the process [88]. Regarding the COF in T-type experiments, the consequences are two fold. On one hand, the higher permeability of oxygen explains why there is a substantial potential drop when H is used in Fig. 4.3. On the other hand, the compromised integrity of the adsorbed oxide film could explain the increasing COF as portrayed on Fig. 4.1.

The presence of this film is crucial in understanding how the additives under study mediate the contact between the indenter and the metallic substrate. That is because adherence of polymers to the surface of metals is strongly dependent on the hydrogen bond formed between functional groups and the oxide layer of the steel [36, 93]. This is specially relevant in the present discussion because sliding contacts produce nascent surfaces, that is, surfaces where bare metal exposed to the surrounding environment and that have shown to prevent attachment of polymer additives [94].

From the water analysis provided on Appendix A, it can be seen that a large variety of ions are present in the H electrolyte. From such analysis, it is inferred that other classes of salts are also present in solution. According to Ref. [87], the main effect of other added salts parallels that of NaCl except for the case of alkaline salts that are thought to improve Fe(OH) stability by raising the pH of the solution. However, since the pH of the H electrolyte is slightly acidic, this effect is not considered influential in the present work. A study on the effect of other cations species in chloride solution shows that while there is a slight difference in the type of cation present, the effect closely follows that of Na^+ [60]. Therefore, for the purpose of the present discussion, the solutions prepared with HTDS water (H electrolyte) are treated as simple NaCl solutions where any deviations from purity are assumed to be constant across experiments.

Specific details about the formulation of the additives have not been disclosed by Calfrac Well Services Ltdas they are trade secrets. However, through internal communication some key characteristics are known about these formulations. D_y and D_w are long chain co-polymers of polyacrylamide prepared in emulsion for faster dissolution upon contact with water. The main difference between them is their overall charges in that D_y is a cationic polymer and D_w is an anionic polymer. A common molecular structure of such polymers is presented in Figs. 4.6 and 4.7 based on Refs. [13, 95–97]. Notice the use of n and m to indicate the ratio of the acrylamide functional group to the complementary ionic functional group. A seen in the figures, the degree of charge in the polymer is controlled by the relative quantity of the carboxyl group for an overall negative charge, and a vinyl quaternary ammonium compound for an overall positive charge.

The degree of charge in the polymer chain is considered an important factor because it affects the level of hydration of the polymer. It is through the ionic character introduced by co-polymerization with these functional groups that the backbone chain is enabled to readily unravel in water, a polar solvent [99]. However, in incorporating charges to into the structure, the polymer also becomes sensitive to the presence of dissolved ions in the solution which can also affect chain extension by affecting chain self-complexation [100]. This latter point is

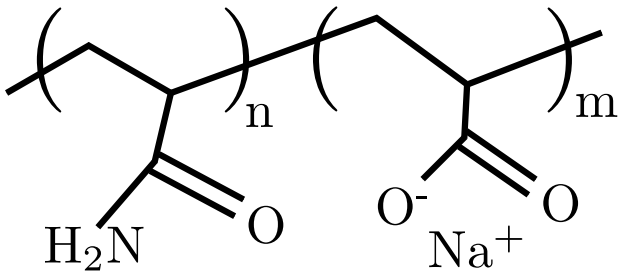

Figure 4.6: Sodium acrylate–acrylamide, an example of anionic copolymer structure. Structure generated with Ref. [98].

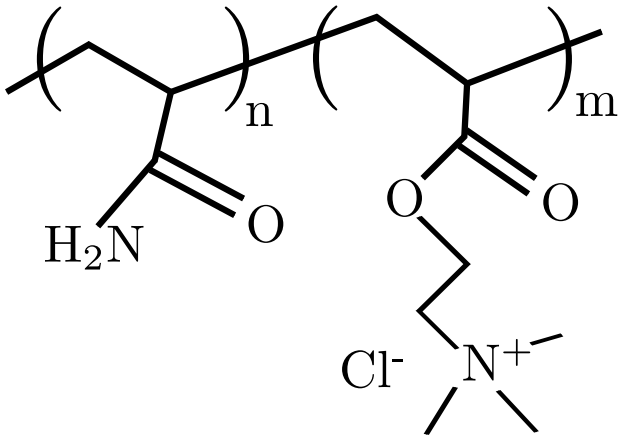

Figure 4.7: Copolymer of acrylamide and acryloyloxyethyltrimethyl ammonium chloride, an example of a cationic copolymer structure. Structure generated with Ref. [98].

raised because the third additive in the present study, C, is a saturated solution of sodium sulfite (Na_2SO_3) that provides additional Na^+ ions in solution. In principle, the intended use of Na_2SO_3 is that of an environmental conditioner that decreases the concentration of dissolved oxygen according to Equation 4.5 [87, 101]. No information is given as to whether catalysts for this reaction have been introduced in the formulation of additive C.

$$Na_2SO_3 + \frac{1}{2}O_2 \rightarrow \ Na_2\ SO_4 \tag{4.5}$$

Gathering it all together, the data suggests that the reason behind the shared upper and lower bounds for the COF in T-type experiments, OCP and E_{WE} is related to the integrity of the adsorbed hydroxide layer on the surface of the steel. One bound corresponding to exposure to the D electrolyte that provides adequate conditions for the formation and maintenance of an adherent hydroxide film; the other bound corresponding to the H electrolyte where any existing surface film is exposed to Cl^- attack, and the hydroxide byproducts are formed away

from the steel surface where they cannot form an adherent film.

In this view, the additives can be thought of as serving a primary and a secondary function. Primarily, the additives serve to protect the adsorbed hydroxide layer. In this sense, the additives compensate for the hostile environment offered by HTDS water in all H-based electrolytes but are limited in that they cannot surpass the performance of the undisturbed layer alone. Secondly, to the extent that this layer is protected, the adsorption of the organic molecules explains slight variations in the data for all solutions containing additives.

A closer look at these secondary effects presents a couple of problems. One of the problems is that although the COF in T-experiments is improved in the presence of additives, it does not become lower than the one obtained when only DI-water is present. This is an unexpected result because, in sliding contacts, the presence of a lubricant should reduce the COF below that of any contacting solids on their own [102]. The other issue is that despite the different chemical nature of the three additives, all three have a similar effect on the recorded potentials OCP and E_{WE}.

A possible explanation for the lack of lubricity lays in the structure of the polymers themselves. While the lubricant effect of functionalized polymers is often attributed to having a polar head attached to the substrate (steel and sapphire in this case) and an extended alkyl chain into the bulk of the liquid, it is perhaps not a good model for the large molecules in D_y and D_w. This is because the functionalized groups can be found a different positions all over the length of the chain. As a consequence, instead of the extending itself into the liquid, a more likely configuration for the adsorbed chain is that of a pancake structure [103–105]. An illustration comparing these structures in presented in Fig. 4.8. Because the lubrication effectiveness is related to the physical arrangement of the molecule, the pancake formation offers a good explanation regarding the poor effectiveness of the organic additives as lubricants.

In contrast to the minor influence on lubricity, the pancake structure can explain the marked effect that the organic additives have on the potentials OCP and E_{WE}. This is because organic molecules displaying functional groups are known to inhibit corrosion by

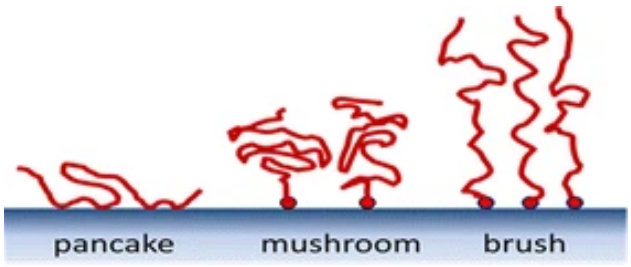

Figure 4.8: Adsorbed polymer brush configurations. Figure obtained from Ref. [105].

blocking active cathodic and anodic sites on the surface of corroding metals, and effect widely reported in the literature [42, 65, 94, 101, 105–108]. However, since the molecules can only block sites where they get adsorbed, and their adsorption mostly happens on regions where the hydroxide film is still present on the steel, the inhibitory effect is constrained to already covered areas which, in turn, offers limited protection to exposed regions. This fundamental constraint of the underlying substrate explains why the E_{WE} potentials in Fig. 4.4 overlap over each other while the OCP potentials in Fig. 4.3 display a more stratified spread. The cause of the spread being the different affinities of the molecules to adhere to the nascent surfaces exposed during the sliding motion in T-type experiments. On a final note regarding the effect of the additives on potentials, it should be mentioned that an anomaly exists regarding additive C with respect to the potentiodynamic polarization curves obtained in C_0-type experiments. Experimental potentiodynamic polarization curves show that the effect of a pure Na_2SO_3 solutions on E_{WE} is that of slightly shifting the curve towards cathodic values [62, 109]. While this effect does not contradict the idea that the primary difference between the potentials is caused by the integrity of the hydroxide layer, it shows that minor effects can be suppressed by experimental conditions. Here in particular, it is thought that despite being open to the atmosphere, the lack forceful mixing in C_0-type experiments undermines the effect of salinity thus resulting in a considerable shift towards anodic values.

Consistent with the idea that the primary factor responsible for the changes in COF is the COF data portrayed in Fig. 4.2. This set of data was gathered under W_0-type experiments which means that cathodic protection was applied to the samples. The intended effect of

cathodic protection is to apply a cathodic potential to the steel sample (working electrode) such that oxidation of the metal is thermodynamically unfeasible [87]. However, the same principle is used to remove rust from the surface of metals [110]. As a consequence, the hydroxide layer disappears and the surface of the metal responds rather independently of the additives in solution. This is therefore put forward as the explanation for the overall erratic behaviour in COF exhibited in this type of test. It includes the elimination of the boundaries discussed previously as well as the clustering of COF values around a higher value than in T-type experiments.

The data from all types of experiments related to wear is reported in Fig. 4.5. Two tests can be applied to the data to characterize the system: the synergism test according to Equation 2.2 revisited, and the dominant regime test according to Refs. [39, 111, 112] that define four wear regions based on the W_c/C_w ratio outlined in Equations 4.6a to 4.6d. The experimental data along with the results from both tests are reported in Table 4.1.

$$\frac{C_w}{W_c} < 0.1 \quad \text{wear dominated} \tag{4.6a}$$

$$0.1 \leq \frac{C_w}{W_c} < 1 \quad \text{corrosion-wear dominated} \tag{4.6b}$$

$$1 \leq \frac{C_w}{W_c} < 10 \quad \text{wear-corrosion dominated} \tag{4.6c}$$

$$\frac{C_w}{W_c} \geq 10 \quad \text{wear dominated} \tag{4.6d}$$

Table 4.1: Synergism and Dominant Wear tests

Fluid	**T**	**C_0**	**W_0**	**S**		**W_C/C_W**	
D	1.27	0.02	1.27	-0.01±0.05	inconclusive	71.5±4.2	wear dom.
H	10.33	0.16	4.08	6.09±0.33	synergistic	25.9±1.5	wear dom.
H_{Dy}	3.12	0.08	2.71	0.34±0.12	synergistic	36.0±2.1	wear dom.
H_{Dw}	6.10	0.11	3.14	2.85±0.21	synergistic	29.2±1.7	wear dom.
H_C	2.86	0.04	2.79	0.04±0.12	inconclusive	75.7±4.4	wear dom.
H_{DyDw}	7.14	0.09	3.28	3.77±0.24	synergistic	36.5±2.1	wear dom.
H_{DyC}	2.38	0.06	2.58	-0.26±0.11	antagonistic	40.7±2.4	wear dom.
H_{DwC}	5.70	0.09	3.04	2.57±0.19	synergistic	35.0±2.0	wear dom.

From Fig. 4.5, it is evident that the degree of synergism exhibited by exposure to most electrolytes is rather large with the exception of H_C and D where the total material loss presents the least fluctuation. This is confirmed by the synergism test where the experimental error is large enough that it is inconclusive to determine whether a synergistic or antagonistic effect took place in these two cases. The considerable degree of synergism in the H electrolyte is attributed to the exceptionally active corrosion potential found during the potentiodynamic tests discussed previously. Accordingly, this effect is diminished in the presence all the other electrolytes containing additives to the extent that electrolyte H_DyC displays an antagonistic effect.

In regard to the dominant regime test, the ratio between W_C and C_W as defined in Equations 3.7 and 3.8 is used to identify the dominant wear regime [39, 111, 112]. As suggested in Ref. [112], under the current experimental conditions, the calculation can be simplified by the approximation of W_C as W_0 and C_W as C_0. This is because the the experimental conditions are such that the pH and potential of the system suggest active dissolution of the steel [112]. Overall, a ratio greater than 10 is generally accepted as an indication that wear in the system is dominated by mechanical wear. Therefore, the test suggests that exposure to all solutions results firmly places the system in a predominance of material loss by mechanical action.

In summary, the outcome of the experiments and analyses from batch 1 is as follows. The adsorbed hydroxide layer on the surface of the steel is the major contributor to the corrosion potentials and COF. This assessment is inferred from key experimental data where the reciprocating motion produces the largest spread of potentials in Fig. 4.3 while the application of cathodic protection reduces friction related with the use of additives as seen in Fig. 4.2. Likewise, it has been found that, despite the existence of some synergism due to the combined action of corrosion and mechanical wear, the latter is the main contributor to wear in all solutions tested.

4.2 Second batch: optimization for least material loss

In exploring the optimal combination of additives, the present section deals with the results obtained from the model set up in Table 3.4. A key feature of the model is the determination of linear coefficients that fit a linear regression to the response surface which takes the general form of Equation 3.14. In the present case, the coefficients that best fit the experimental data are reported in Table 4.2. From left to right, the table consists of 6 columns. The first column, titled *Term*, displays the name of the variable used in the model which corresponds to the name of each of the three additives used plus a *Constant* term that serves the purpose of fixing the surface in the combinatorial space.

The next two columns correspond to the coded coefficients (Coef) and their respective standard error (SE Coef) respectively. The output uses the numbers under Coef to represent the mean change in the response associated with the high and low values as standardized through Equation 3.13. The column SE Coef serves to contextualize such numbers in providing an interval of confidence. The T-Value column reports the values corresponding to a t-distribution and is obtained by dividing Coef over SE Coef. Likewise the P-Value column is related to the T-Value column in that it reports the significance level of each variable according to the cut-off value at the tail of the t-distribution from the T-Value column. Lastly, the VIF column reports the *Variance inflation factor* which indicates how much multicollinearity exists in the regression analysis. A VIF of 1 is the result of no multicollinearity with higher VIF numbers up to 5 being acceptable for a useful analysis [85, 113]. The regression for the response in physical units is displayed in Equation 4.7.

$$\begin{aligned}\text{Lin. wear vol. } (\mu m^2) = 684.5 \; - \; 807 \; D_y + \; 396 \; D_w - \; 33 \; C + \\ 357 \; D_y \cdot D_y - \; 605 \; D_w \cdot D_w + \; 141 \; C \cdot C \; + \; 384 \; D_y \cdot D_w + \\ 158 \; D_y \cdot C \; + \; 218 \; D_w \cdot C \end{aligned} \quad (4.7)$$

The model itself is assessed with the statistical tool known as Analysis of Variance

Table 4.2: Analysis of coded coefficients

Coded Coefficients					
Term	**Coef**	**SE Coef**	**T-Value**	**P-Value**	**VIF**
Constant	626.1	27.8	22.54	0	
Dynarate	-89.4	25.6	-3.5	0.006	1
DWP	46.4	25.6	1.82	0.099	1
CalGuard	148	25.6	5.79	0	1
Dynarate*Dynarate	89.3	48.7	1.83	0.097	1.82
DWP*DWP	-151.1	48.7	-3.1	0.011	1.82
CalGuard*CalGuard	35.1	48.7	0.72	0.487	1.82
Dynarate*DWP	96.1	28.6	3.36	0.007	1
Dynarate*CalGuard	39.6	28.6	1.39	0.196	1
DWP*CalGuard	54.5	28.6	1.91	0.086	1

(ANOVA), the components of which are presented in Table 4.3. As before, from left to right, there are six columns. The first column, *Source*, identifies the terms associated with the interactions between the variables used in the model of Equation 4.7 as well as the error associated with the model. The next column, *DF*, stands for the degrees of freedom that each term uses. The total degrees of freedom for the sample of a population is one less than the number of observations taken [85]. In this case, the model uses 9 out of the total 19 available degrees of freedom. The remaining 10 degrees of freedom are associated with repeated observations (zero-point in the combinatorial space), and higher level interactions not included in the model. These remaining degrees of freedom are useful in that they allow for the calculation of the *Lack-of-Fit* and *Pure Error* terms.

The *Adj SS* column stands for the adjusted sum of squares which measures the contribution of each term to the total variation in the model. Conversely, the *Adj SS Error* is the sum of the squared residuals and quantifies the variation that the model cannot explain. The information in this column is used to calculate the P-Value in the last column and the R-sq statistic in the Model Summary shown in Table 4.4. The *Adj MS* in the forth column stands for the adjusted mean square. This column quantifies the amount of variance with respect to the degree of freedom of each term. The last two columns *F-Value* and *P-Value* columns show the signal to noise ration and the probability against the null hypothesis respectively.

Table 4.3: Analysis of Variance

ANOVA					
Source	**DF**	**Adj SS**	**Adj MS**	**F-Value**	**P-Value**
Model	9	496959	55218	8.46	0.001
Linear	3	320519	106840	16.36	0
Dynarate	1	79867	79867	12.23	0.006
DWP	1	21549	21549	3.3	0.099
CalGuard	1	219103	219103	33.56	0
Square	3	66231	22077	3.38	0.062
Dynarate·Dynarate	1	21921	21921	3.36	0.097
DWP·DWP	1	62809	62809	9.62	0.011
CalGuard·CalGuard	1	3397	3397	0.52	0.487
2-Way Interaction	3	110209	36736	5.63	0.016
Dynarate·DWP	1	73907	73907	11.32	0.007
Dynarate·CalGuard	1	12558	12558	1.92	0.196
DWP·CalGuard	1	23744	23744	3.64	0.086
Error	10	65295	6530		
Lack-of-Fit	5	27356	5471	0.72	0.636
Pure Error	5	37939	7588		
Total	19	562254			

By convention, the null hypothesis is the hypothesis that there is no difference between the means, or in this case, that the contribution of the individual components does not explain the variation in the response [85]. The lower the P-value of a term, the more likely it is that the term is significant in explaining the variation. At the confidence interval of 95%, the model as a whole explains the variation with a P-Value of 0.001. Individually, the table shows that there are significant contributions from Linear, Square, and 2-Way Interaction terms. In regard to the Lack-of-Fit term, the equivalent null hypothesis here is that the model correctly establishes a relationship between the variables and the response. At a P-Value of 0.636, it is concluded that the Lack-of-Fit is not significant, and therefore the constructed model is adequate.

It has been suggested that when there are not significant interactions in the model, as in this case, good practice is to reduce the model by systematically eliminating the terms and recalculating the results [85, 113]. However, in doing so, the statics of the model were

weakened in comparison with the non-reduced model. As will be shown later, both versions of the model coincide in their optimization result. As consequence, the calculations based on the reduced model are presented in Appendix D while the current discussion regards the non-reduced model. This choice is further justified in that, despite the presence of non-significant terms, the non-reduced model has been used in similar studies involving corrosion inhibition additives [81, 83].

The significant contributions as outlined in Table 4.3 are clearly visualized on the Normal plot of standardized effects in Fig. 4.9. Shown on the figure are all the interactions in the model plotted along with a linear distribution for the case when the effects are zero [113]. Only the effects that significantly depart from the distribution according to the set confidence interval are given a label in the plot. Effects to the right of the distribution line are said to have a positive effect on the response. The larger the effect, the larger the response. Conversely, effects to the left of the distribution are said to have a negative effect on the response. Reflected on the plot is also the importance of each effect in that the further it departs from the distribution on the x-axis, the higher its importance in the response according to the model.

The Model Summary is provided in Table 4.4 presents some key statistics about the constructed model. The first statistic, *S*, stands for the standard deviation of the difference between experimental and fitted values, and is reported in physical units. The lower the value of S, the better the better the model describes the response. The *R-sq* term (also known as R^2), is the percentage of the variation of the response that is explained by the model. The higher the value of R, the better the model fits the data. the *R-sq(adj)* statistic is similar to R2 with the caveat that it is adjusted by the number of predictors in the model with respect to the number of observations. This statistic is important in that it addresses the statistical tendency of 2 to increase with the number of predictors regardless of real improvement of the model [85]. In the current study, the values of 88.39% and 77.94% respectively suggest that the model is adequate to the extent that it accounts for more than three quarters of the variance in the response. Finally, the *R-sq(pred)* recalculates R^2 by systematically

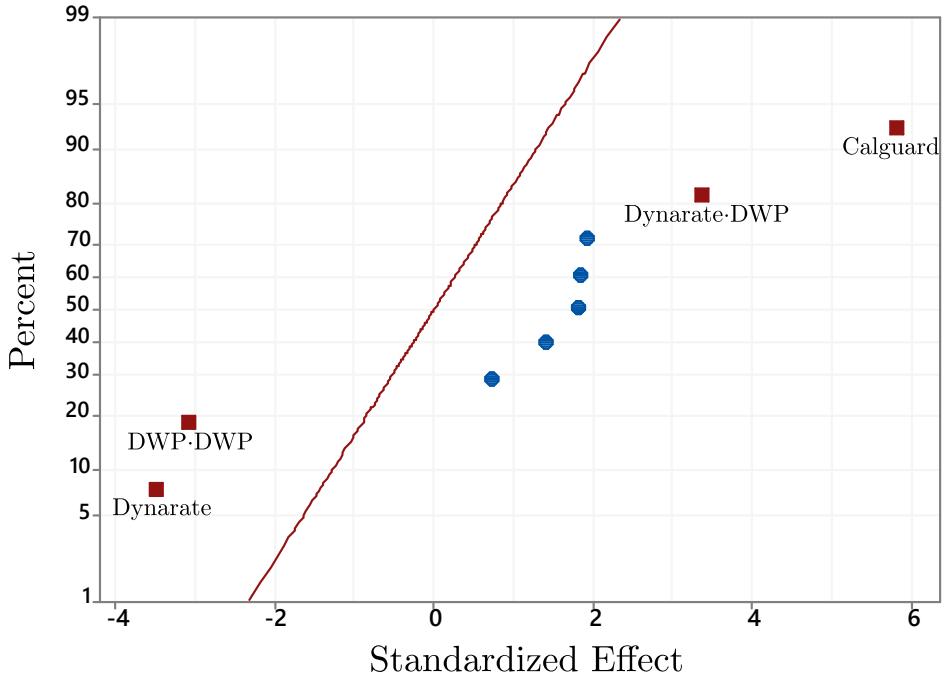

Figure 4.9: Normal plot of standardized effects.

removing each observation, refitting the model, and then measuring the distance between the new model and the removed data point. This statistic is used to measure the predictive ability of the model with regard to new observations; larger R-sq(pred) values are associated with better predictive ability. A considerable low R-sq(pred) could indicate that the model is over-fitted to the data. At 63.52%, the R-sq(pred) of the current model suggests that over-fitting may be a concern.

Table 4.4: Summary Statistics for the CCD Model

Model Summary			
S	**R-sq**	**R-sq(adj)**	**R-sq(pred)**
80.8053	88.39%	77.94%	63.52%

In addition to the statistical measures discussed above, the residual plots offer a complimentary piece of information for the assessment of the model. One of such plots is the Normal Probability Plot presented in Fig. 4.10. This plot shows the residuals with respect to the their expected positions assuming that they are normally distributed. The graph shows a couple of outlier data points along with a generally linear trend exempt from skewness

or curvature. This suggests that the selected confidence interval is sufficiently accurate for the model. Another important graph is that of the Residual vs Fitted Value plot in Fig 4.11. Plotting data according to these axes highlights any variance present in the regression. This plot is used to verify the assumption that the residuals are randomly distributed with constant variance. Such assumption is justified in that the data points in Fig. 4.11 appear randomly distributed on both sides of the zero line without any clear outlier in the y-axis nor the x-axis. The last residual plot presented is that of Fig. 4.12. Here, the residual is plotted with respect to the chronological order in which the data was collected. This plot verifies the assumption that the measurements are independent of one another. In this case the assumption is justified because, just like in the previous case, the data points fall randomly on both sides of the zero line. Overall, the plots of the residuals show that the underlying assumptions of normal distribution, constant variance, and non-correlation are met by the model.

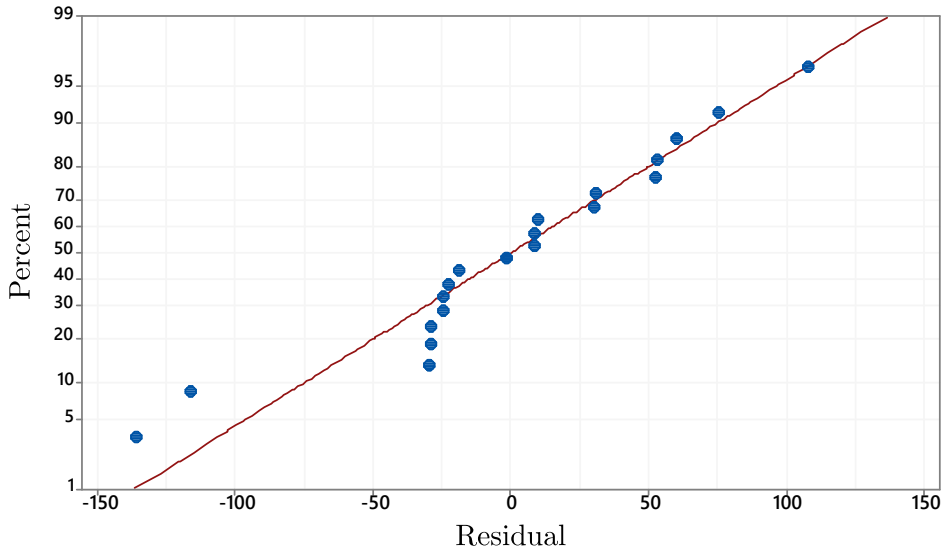

Figure 4.10: Normal Probability plot of residuals.

A visual representation of the response according to the model is presented in Fig. 4.13. Because the combinatorial space is results in a hypersurface spanning four dimensions, the response is depicted in the form of three contour plots. For each contour plot, one variable is systematically held constant at its mid-vale (labeled in the figure as Hold Value) in order

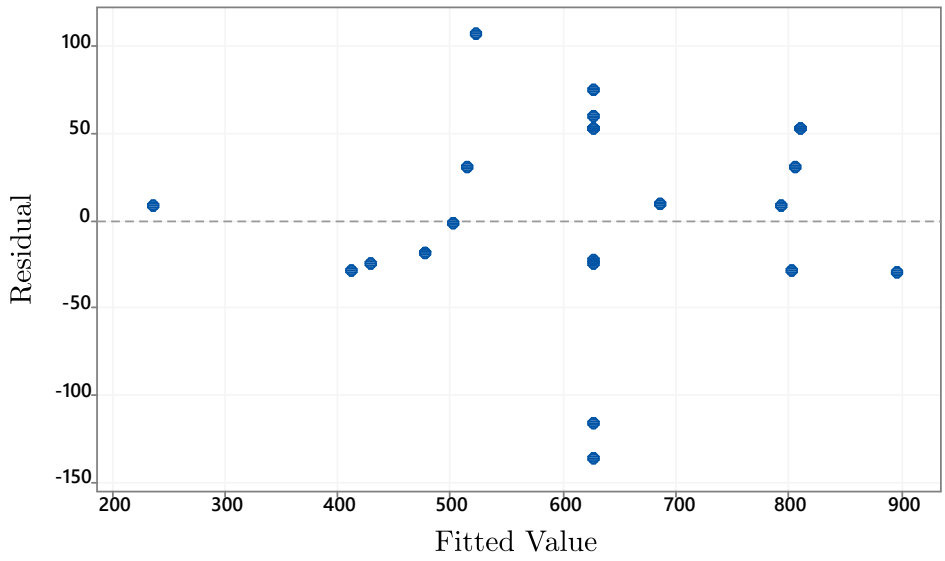

Figure 4.11: Plot of residuals vs fit.

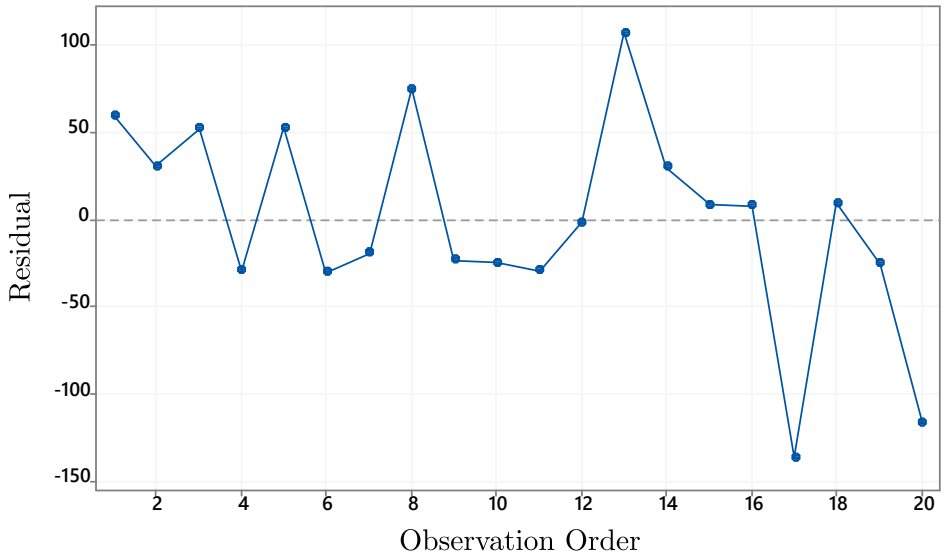

Figure 4.12: Plot of residuals vs. chronological order of data collection.

to observe how the response changes in regard to the other two variables. In essence, each contour plot shows a three dimensional slice of a four dimensional surface. The presence of a curvature is clearly identified in all three contours which shows the non-linearity of the effects caused by the interaction between variables.

While the contour plots show the response across the combinatorial space, the effect of pairwise interaction between the additives is not clearly identifiable. For such purpose, the interaction plots in Fig. 4.14 use the mean of the response to clearly outline the relationship

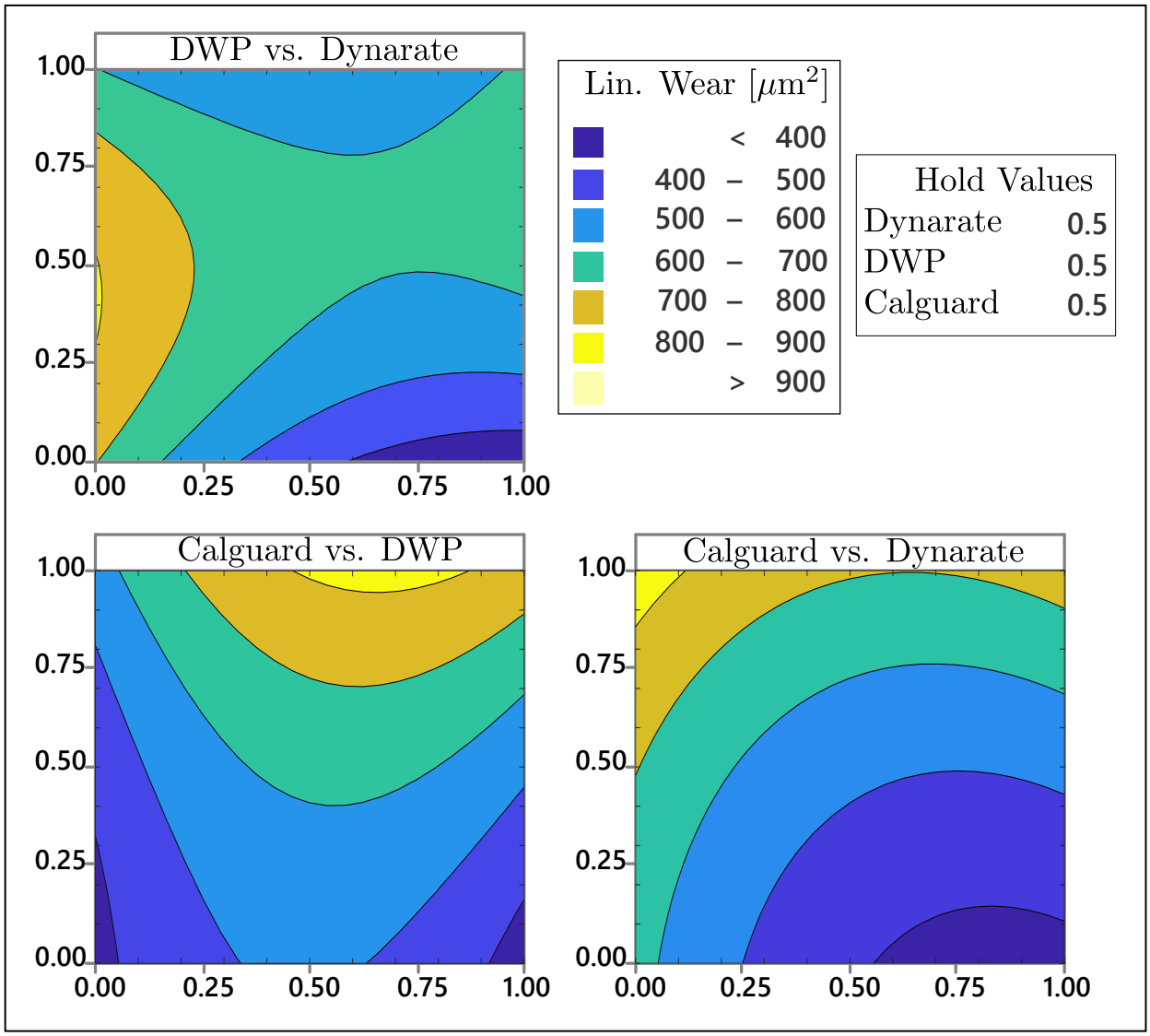

Figure 4.13: Contour Plots showing the degree of wear according to the model.

between pairs of additives at different levels. The interpretation of these iso-plots is as follows. One variable is held constant at specific values, namely the high (1), low (0), and mid-points (0.5) while the other variable is allowed to change freely. Simple additive effects are identified bye the offset of the same patter as the quantity of the hold additive is set at different values. Superadditive effects are identified by an increase (or decrease) in the response at points where both additives are found together and the resulting value is greater (or lower) than when only one factor is used [85]. Such effects are present in all the plots in Fig. 4.14 which necessitates software processing for an overall optimization of the response.

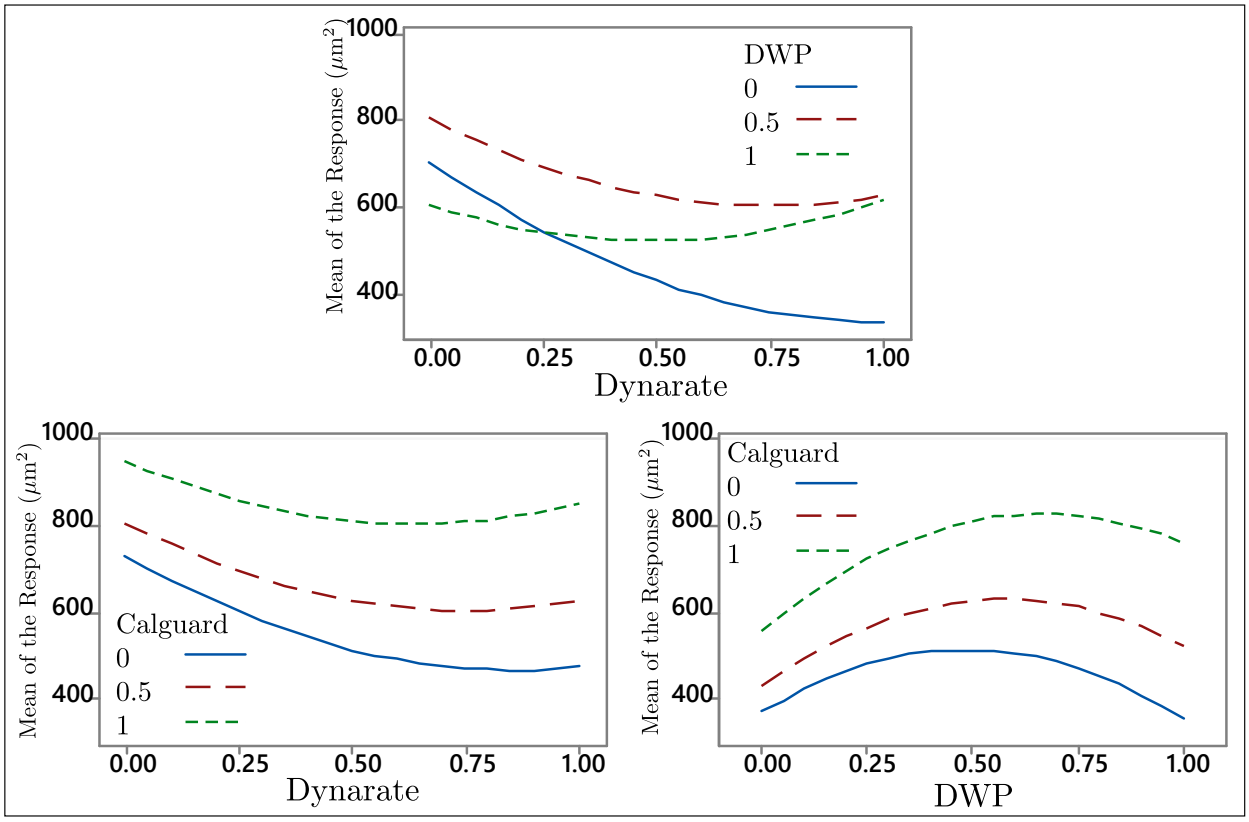

Figure 4.14: Interaction plots

Table 4.5: Optimal additive combination

Variable	Setting
Dynarate	1
DWP	0
CalGuard	0

Table 4.6: Predicted response at optimal parameters

Response	Fit	SE Fit	95% CI	95% PI
Lin. Wear (umˆ2)	234.3	72	(74.0, 394.7)	(-6.8, 475.4)

Consequently, the last step in the statistical model is to estimate the combination of factors that optimize the response. Because the response in the current study models the amount of wear on the samples, to optimize the response means to find the combination of variables that result in the least material loss. Table 4.5 shows the combination of variables as collected by the output of the software. It is clear that despite the curvature shown in the

model, Dynarate alone is estimated to result in less wear than when any amount of either DWP or CalGuard is present. Statistics about the response when this settings are used are presented in Table 4.6. The *Fit* value is the expected response average in the presence of Dynarate. The *SE Fit* stands for the standard error of the estimated response and is equivalent to one standard deviation in response units (μm^2). The last two terms, *CI* and *PI* stand for the confidence interval and prediction interval respectively. The ranges below each of these two terms are lower and upper boundaries of the intervals.

4.2.1 Discussion

The procedure involved in obtaining a result from the CCD design in the RSM methodology has been outlined in the preceding section. Through the process of outlining the individual aspects that constitute the model, terms with P-values lesser than the the established threshold for significance have been encountered both in Tables 4.2 and 4.3, and Fig. 4.9. This along with the large intervals provided for the optimal combinations in Table 4.6 suggest a large degree of uncertainty in the model. As seen in Appendix D, a systematic elimination of non-significant terms has little effect in improving this uncertainty, and perhaps, is counterproductive to improving the model. A hint that the set up of the model has been conducted properly is provided by the residual plots in Figs. 4.10-4.12 that show well behaved patterns. Therefore, it is likely that the variability present in the model is rooted in the physical features of the system itself. Rather, the available information suggests that the additives themselves present a large variability within themselves compared to between them. In other words, while the model suggests that one additive, namely Dynarate 6524 is the most effective at reducing wear, Dynarate 6524 itself is not much distinct in its effectiveness from the other additives tested.

Regardless of their similarity, the additives are distinct enough to offer some insight into the interaction between them. In examining Figs. 4.13, 4.14, and contrasting them with the numerical data in Table 4.3, it is clear that the main source of curvature (non-linear effects)

is the presence of CalGuard. The superadditivity of polymer mixtures is in fact a well known phenomenon that originates in the thermodynamics of mixtures and affects other properties such as the ability of the mixture to present low fiction coefficients [114]. As elaborated on the Discussion section 4.1.1, CalGuard may present two competing effects. On one side, it can affect the salinity of solution by contributing additional Na^+ ions which can affect the extension of the carbon chains of the other two additives. On the other side, by acting as an oxygen scavenger it can improve the adherence of the hydroxide layer on which the other additives are adsorbed. Consequently, this makes Calguard an important factor to control in any further studies or applications in the presence of organic additives.

4.3 Third batch: Exploration into Dynarate 6524

As established through the RSM methodology, Dynarate 6524 or Dy is the better performing additive at reducing wear. After the initial tests presented in Section 4.1, the following tests serve to further the understanding of the system under the influence of this additive. From batch 1, both the electrochemical and abrasive components were taken separately to find quantify their synergism. The present section takes a closer look at the system now that the scope has been reduced to the better performing additive. As a representative illustration of the changes to the system when the conditions are not isolated, Fig. 4.15 shows linear polarization resistance plots comparing the system left still to the system under reciprocating motion.

In pursuing further characterization, more testing has been conducted. Potentiodynamic electrochemical impedance spectroscopy (PEIS) is the first of such tests. Fig. 4.16 shows the Nyquist plot for three experimental runs taken before the initialization of reciprocation, mid-way through the reciprocation, and immediately after reciprocation. Each of these runs is color coded and labeled. Raw data is presented on the plot as scatter points while the fit according to the equivalent circuit is displayed using solid lines. The fitting parameters as obtained from the EC-Lab are shown in Table 4.7. Notice that the Z_W element represents

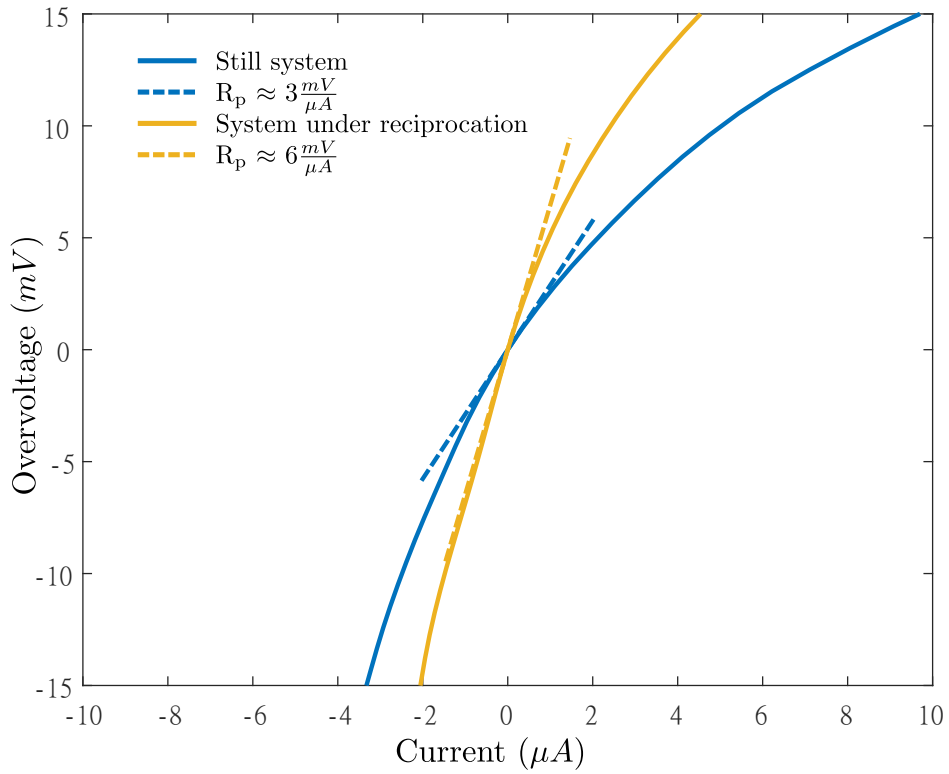

Figure 4.15: Linear Polarization curves for the system while left still and under reciprocating motion.

the Warburg impedance and therefore is a modeled through through the parameters R_W and τ_D according to Equation 3.3. The units for each parameter are provided where resistances are given in Ohms (Ω), capacitances in micro Farads (μF), and time in seconds (s).

Table 4.7: Fitting PEIS parameters for the equivalent circuit.

Data Fit			
Parameters	**Before**	**During**	**After**
$\mathbf{R_s}$ **(Ω)**	7.55	0.01	0.09
$\mathbf{C_f}$ **(μF)**	36.90	57.37	76.57
$\mathbf{R_f}$ **(Ω)**	1914.00	1334.00	2494.00
$\mathbf{C_{dl}}$ **(μF)**	51.47	76.78	2.44
$\mathbf{R_t}$ **(Ω)**	2344.00	1421.00	15.60
$\mathbf{R_W}$ **(Ω)**	1534.00	895.10	3209.00
$\boldsymbol{\tau_D}$ **(s)**	3.64	1.64	1.38

Complementary data is provided in the form of the Bode plots of Fig. 4.17. Fig. 4.17 (a) shows the modulus of the total impedance of the equivalent circuit plotted against the

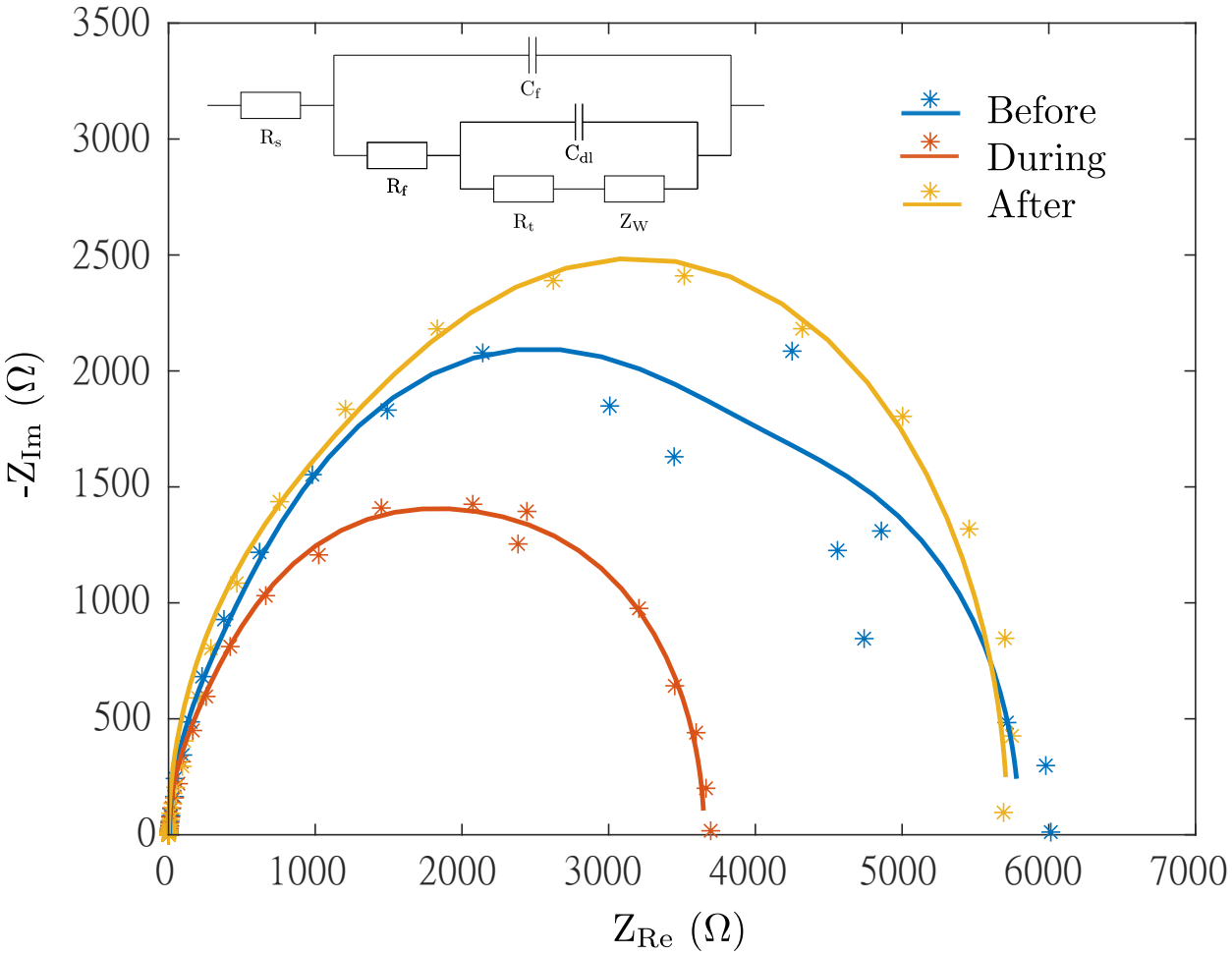

Figure 4.16: Nyquist plots taken before, during, and after the onset of reciprocation. The data is presented in the form of scatter points while the lines represent the best fit according to parameters on Table 4.7

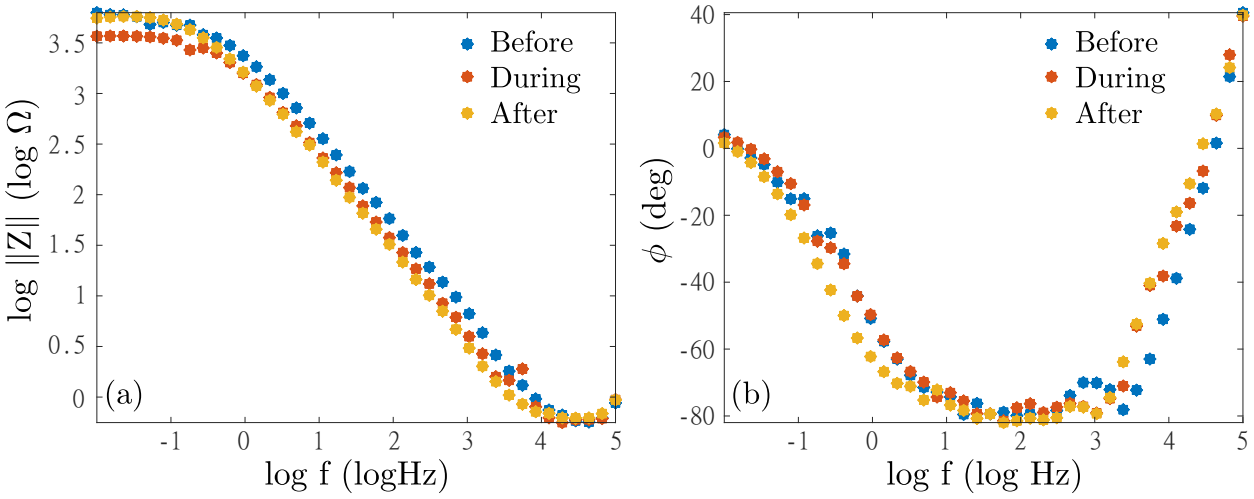

Figure 4.17: Bode plots showing the raw data collected during the same experiment as that of Fig 4.16

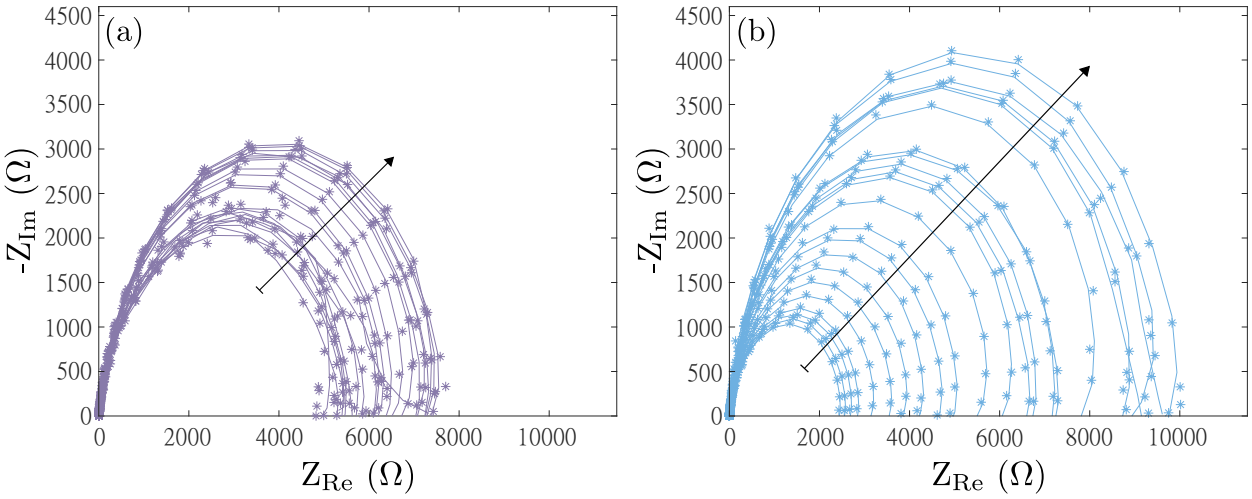

Figure 4.18: Direction of drift over time for (a) under reciprocation motions and (b) left undisturbed. Each trace corresponds to one PEIS scan. The arrow indicates the direction of growth over time.

frequency, both on a logarithmic chart. Fig. 4.17 (b) shows the phase angle of the total impedance plotted against the frequency in a semi-logarithmic chart. Additionally, the drift tendency of the system is illustrated in Fig. 4.18 through Nyquist plots of repeated test runs. Both Nyquist plots in Fig. 4.18 portray the same number of runs equivalent to a total testing time of approximately 4.4 hours or three times the duration of a single test in batch 1. This comparison regards solely experimental time by excluding the resting time allocated at the beginning of all experiments. Fig. 4.18 (a) shows the evolution of the system over time while the reciprocating tribometer is engaged. This test is equivalent to an extended T-type test. Fig. 4.18 (b) shows the evolution of the system while no reciprocating motion is applied.

After testing, SEM and EDX imaging was conducted on the samples from this new batch. These steel samples have the unique characteristic that they feature small and large areas of interest. The large areas of interest can only be partially shown because they exceed the size limitations of the available instrumentation. While the smaller areas are well withing the capabilities of the instrumentation, it is also important for a meaningful discussion to clearly identify where on the sample these measurements were taken. Therefore, the following diagram of Fig. 4.19 will be superimposed on the SEM and EDX figures. The black region represents the area of the sample that would have been covered with electrically

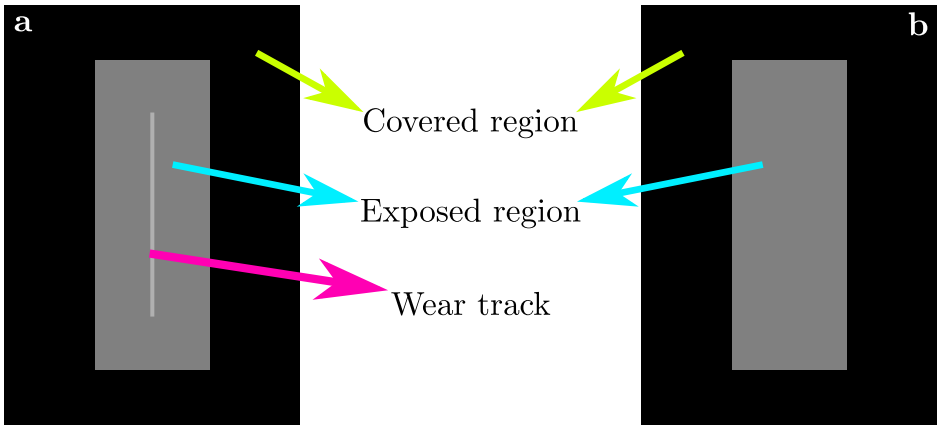

Figure 4.19: Schematic of steel samples as seen from above. The sample in part (a) represents a sample where reciprocating motion has been allowed to take place. The sample in part (b) represents a sample where the wear track is absent because no reciprocation has taken place.

insulating tape as demonstrated in Fig. 3.1. It should be pointed out that although the sample was covered during testing, the tape was removed for imaging purposes. The gray region represents the exposed area where the steel was in contact with the electrolyte. Finally, the wear track is present only where reciprocation took place and corresponds to a smaller region within then exposed metal.

In keeping with the theme of the types of experiments conducted in the current research, the following figures correspond to SEM imaging conducted on repeat experiments from batch 1 to ensure sample freshness. Fig. 4.20 corresponds to a sample conducted during a T-type experiment where no external potential was applied to the sample. Seen in the figure are the wear track, the exposed region, as well as part of the covered region. A compositional map of carbon and iron is included in the figure as well as a plot of EDX energies measured from the same region. Peaks characteristic for specific elements have automatically been highlighted in the figure. Figure 4.22 shows a close look at the wear track for a sample from a W_0-type test where cathodic protection was applied. Here, the compositional map highlights calcium, oxygen, and iron. Lastly, Fig. 4.21 shows a sample exposed to a C_0-type test. The compositional map highlights the presence of iron and carbon and is split into two regions with their corresponding EDX energy plots provided in the same figure.

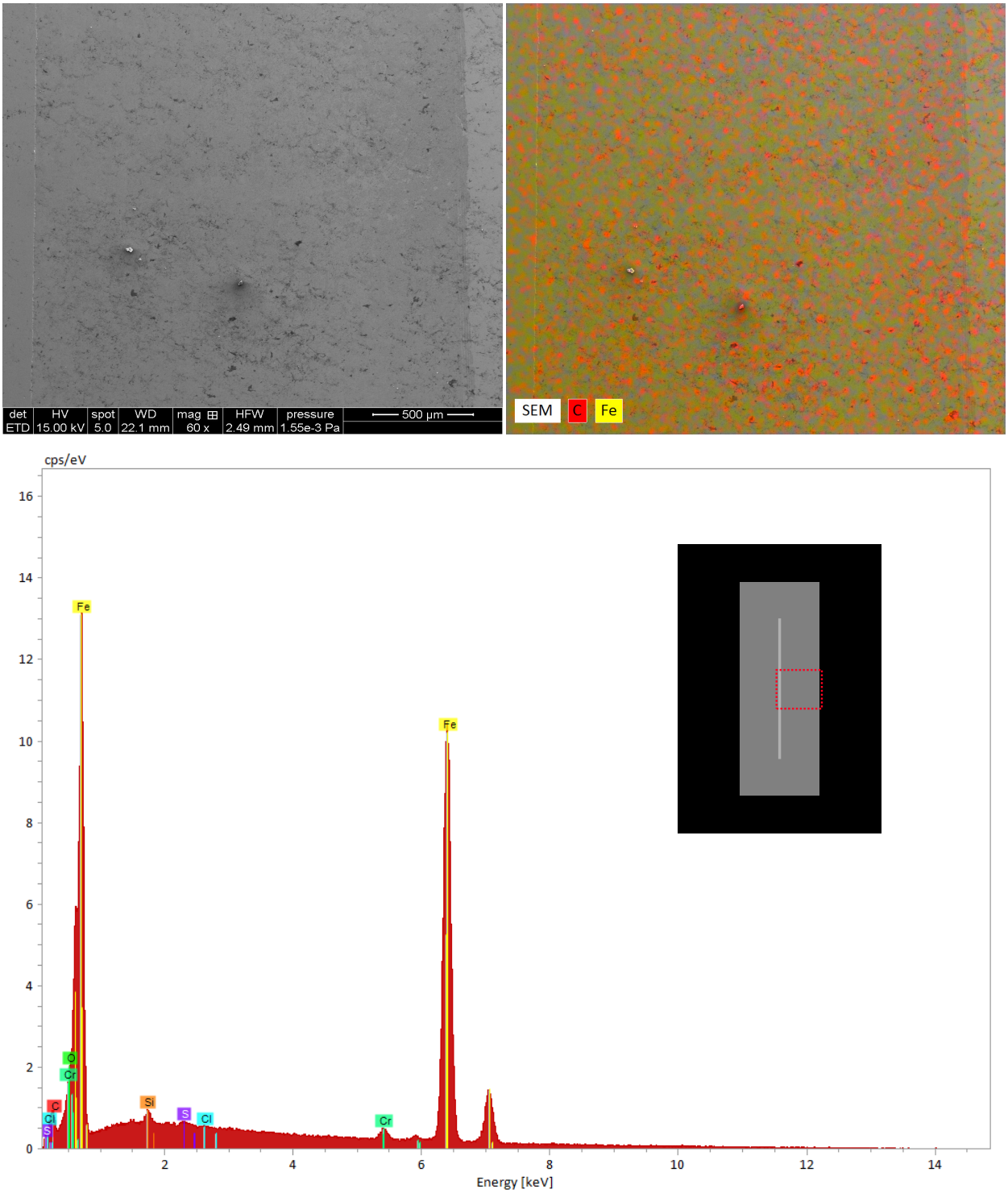

Figure 4.20: SEM imaging of a steel sample after a T-type test.

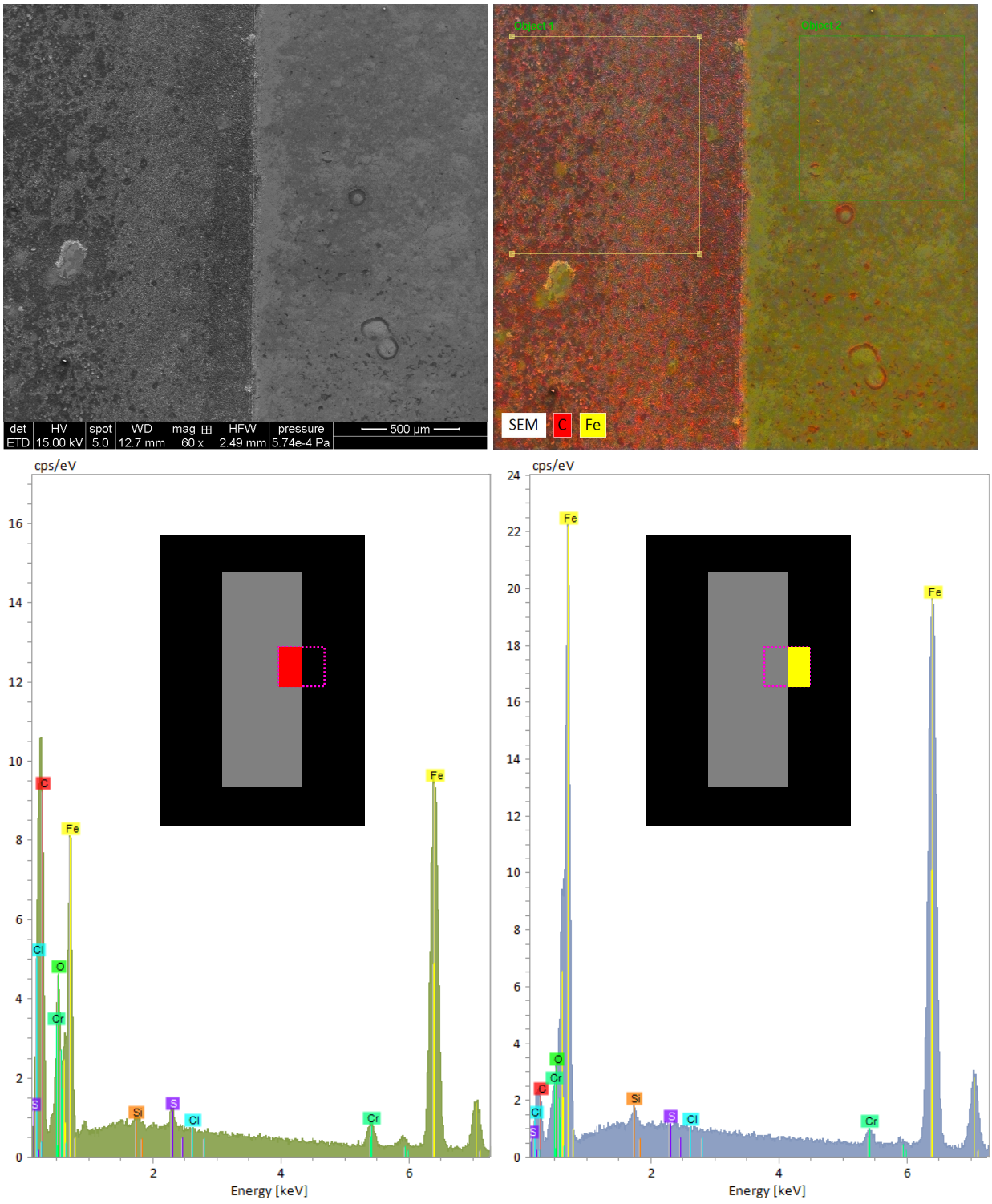

Figure 4.21: SEM imaging of a steel sample after a C_0-type test.

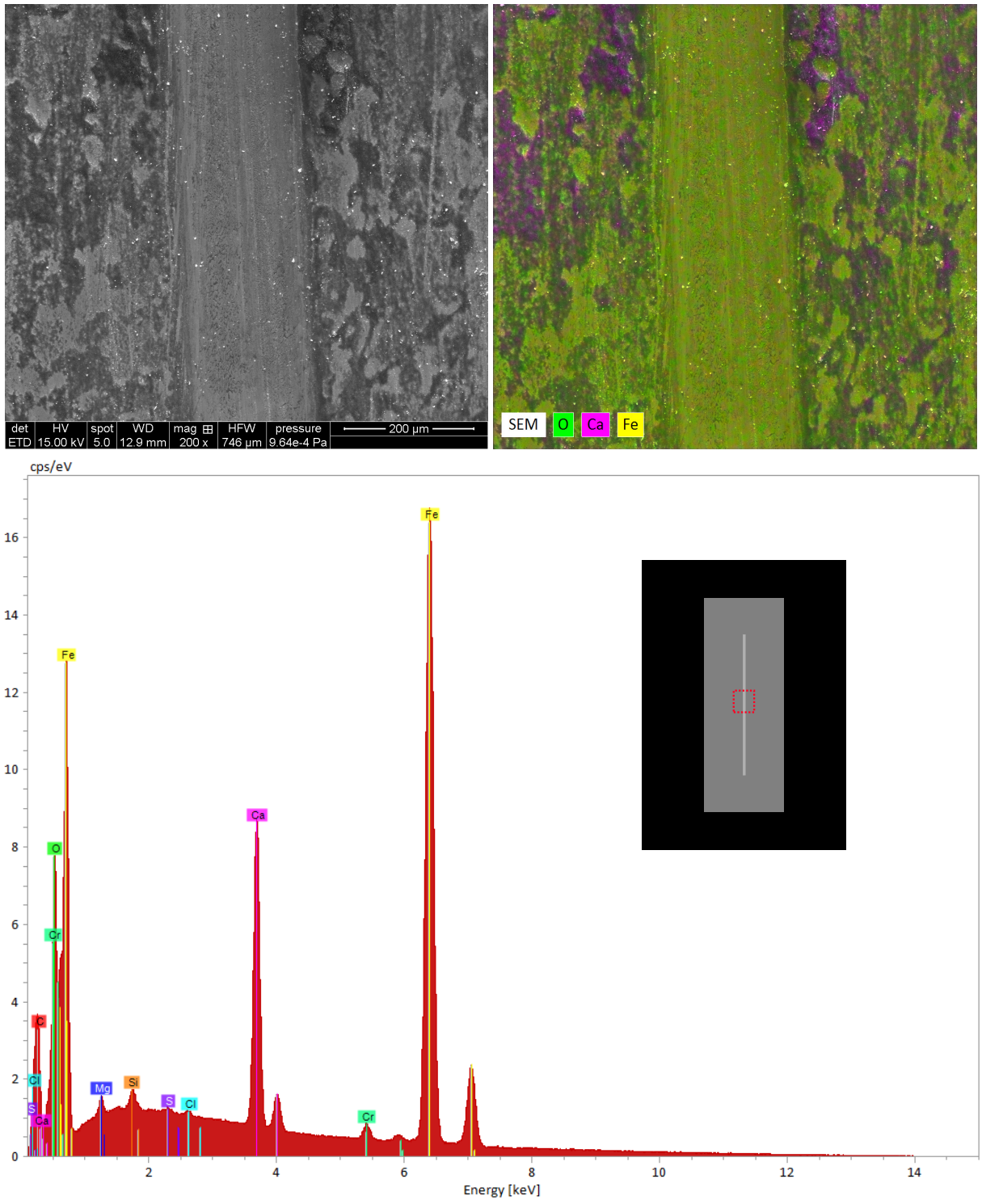

Figure 4.22: SEM imaging of a steel sample after a W_0-type test.

The last figure of the section corresponds to a hardness test conducted with the same nano-idnentation instrument used for SPM measurements as described in Section 3.4.2.2. With this instrument reports the hardness of a material in the units of applied stress as seen in Fig. 4.23. The figure illustrates the variation in hardness by taking measurements across the wear track, where the middle position corresponds to the center of the wear track while the other four correspond to points located to the left and right and right of the wear track. The measurements were repeated seven times, each time moving the instrument to different positions along the wear track. The standard deviation for the aggregate of measurements at the labeled positions away from the wear track is represented by the error bars.

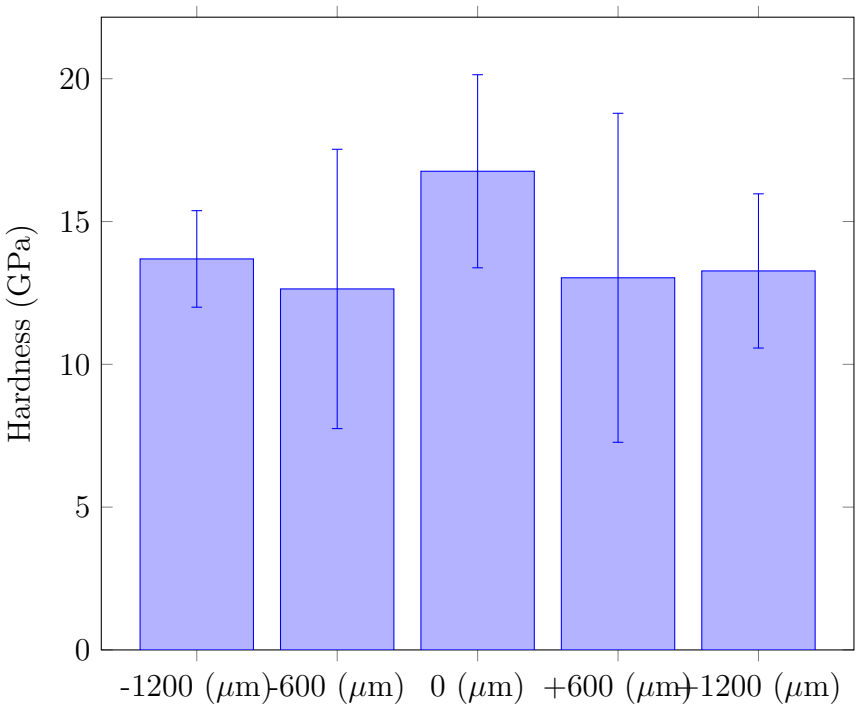

Figure 4.23: Hardness distribution in distance from the center of the wear scar in a T-type experiment.

4.3.1 Discussion

It has been stated that this section seeks to expand on the understanding of the tribocorrosion system. Fig. 4.15 serves as the link between the previous sections and the present one. The polarization resistance of the system is readily observed as it corresponds to the slope of the

plot as the overvoltage approaches zero, or more formally, according to Equation 4.8 where ε stands for the overvoltage, and i_{app} for the applied current [115].

$$R_p = \left[\frac{d\varepsilon}{di_{app}}\right]_{\varepsilon\to 0} = \left[\frac{\Delta\varepsilon}{\Delta i_{app}}\right]_{\varepsilon\to 0} \tag{4.8}$$

However, this is not the only representation of R_p. Assuming the case of the simple Randles circuit shown in Fig. 3.5 (a), R_p can also be readily visualized from the a Nyquist plot such as that presented in Fig. 4.16. Here, R_p corresponds to the segment along the Real axis bounded by the intersection of both endpoints of the capacitive arc [115]. Because at high frequencies (the left end of the arc), the intersection with the real axis is almost at zero, R_p can be readily estimated by just looking at the intersection point of the data at low frequencies (right end of the arc). Since the equivalent circuit used for fitting the data is a variation on the Randles circuit as shown in Fig. 3.5, it is assumed that this general principle of estimating R_p still applies for this test. By comparing R_p values from Figs. 4.16 and 4.15, and realizing that the units of Ω are equivalent to $\frac{mV}{\mu A}\cdot 10^3$, it can be established that the measurements from both techniques are consistent and are therefore meaningful representations of the tribocorrosion system.

In a Nyquist plot such as the one shown in Fig. 4.16, the real contributions to the impedance are thought to correspond to the resistors in the equivalent circuit, whereas the imaginary contributions to the impedance are attributed to the capacitive components. Therefore, the reduction in size of the capacitive arcs from blue to orange, can be directly attributed to coating degradation due to reciprocating wear. A remarkable feature of this plot is that it shows that the adsorbed organic inhibitor can readily cover the worn surface as evidenced by the yellow trace taken immediately after the rubbing portion of the experiment had ended. Furthermore, by observing the Bode plots of Fig. 4.17, it is clear that no fundamental change to the corrosion mechanism has occurred as all the data points show a near perfect overlap in regard to the Impedance magnitude $\|Z\|$ as well well as the phase angle ϕ.

Perhaps the most unexpected result comes form the drift Nyquist plots taken with PEIS and portrayed in Fig. 4.18. Because it is not possible to take more than one measurement immediately before and immediately after testing, the original intent of the drift plots was to provide information about experimental error to determine whether a change in the size of the capacitive arcs is significant or just experimental noise. Instead, it was found that within the timescale of the current experiments, the system does not reach equilibrium. In fact, a supplementary test provided in Appendix E and consisting of multiple sequential runs over night suggests that this trend continues for an extended period of time. Another highlight of this phenomenon is that it appears to take place even in the presence of reciprocation motion as seen in Fig. 4.18 (a). This suggests that the film is not entirely removed by the reciprocating action and that some residual inhibitor may be accumulating over time.

This finding about drift and non-equilibrium state is only possible thanks to the use of PEIS because under the open circuit potential (OCP) conditions, the contrary would be suggested: that the system achieved equilibrium within one hour of exposure to the solution. This assumption was based on the seemingly stable OCP plots for several additives provided in Fig. 4.3 that remain generally stable even during a T-type experiment, as well as the suggestion from ASTM G5 that prescribes a resting time of 55 minutes prior to testing for a corrosion system to be electrochemically stable[54]. One way to reconcile these seemingly contradictory pieces of information is through porosity. When the inhibitor is adsorbed on the surface of the steel, it tends to attach itself to cathodic and anodic sites, as exposed during Section 4.1.1, resulting in an immediate inhibitory effect. Then, as laid out in a previous work by Chen et al. [35], the increase in capacitance of the corrosion system over time can be attributed to the degree of porosity of the coating. A schematic of such porous inhibitor coating is provided in Fig. [35]. Furthermore, the porosity was found to decrease (and therefore having the effect of increasing capacitance) with an exposure time on the order of hours which is consistent with the findings of the current work.

The compositional maps presented in Figs. 4.20 through 4.22 are intended to show changes to the surface of the steel as a consequence of the tribocorrosion process. In comparing the

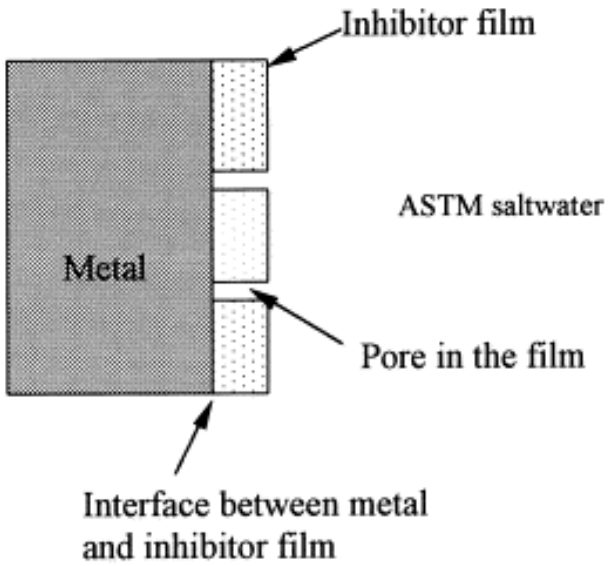

Figure 4.24: Schematic of the porous nature of adsorbed coatings formed by inhibitors. Taken from [35].

surface of the steel after a regular tribocorrosion test (T-type experiment where no external potential had been applied), and that of a severely corroded sample (C_0-type experiment where the sample was exposed to anodic polarization for an extended period of time) the most prominent energy peaks have been used to determine which elements to highlight on the compositional map. In the case of Figs. 4.20 and 4.21, the characteristic peaks that stand out from the background noise are iron and carbon. The compositional map from Fig. 4.20 shows no appreciable change in the distribution of the relative amounts of these elements across any of the three regions: covered, exposed, and exposed plus abrasive wear. By contrast, the compositional map form Fig. 4.21 shows a marked change in composition between the exposed and covered regions. The covered area and its corresponding EDX energy plot shows a composition more in line with that of Fig. 4.20 while that of the exposed region suggest a much higher carbon content. This feature could be explained through relative enrichment of carbon already present in the alloy. It is hypothesized that as iron in the carbon steel is dissolved into the electrolyte, the pre-existing carbon in the material is left behind in increasingly higher concentrations. A supporting reason for this assessment is that any other external source of carbon such as dissolved impurities in the electrolyte, or trace amounts of

the organic additive, would also be displayed in Fig. 4.20 on any of the exposed regions.

Following the same approach of identifying elements of interest based on the EDX energy plot, in Fig. 4.22 the chosen elements for the compositional map are oxygen, calcium, and iron. The purpose of studying this sample is that of assessing the assumption that cathodic protection (W_0-type experiment) can isolate the effect of mechanical wear. However, by the presence of the characteristic peaks from calcium and oxygen, and the distribution of calcium spots around the wear track, the compositional map suggests the presence of calcareous deposition. This finding is noteworthy because solid precipitates could lead to increased wear due to third body interactions.

The last factor examined in this section is the degree to which the sample undergoes work hardening. This factor is important in how relevant the data gathered under laboratory conditions is in regard to field applications. If the degree of work hardening is highly pronounced and focused on the wear track, it might be an indication that the forces were highly localized which in turn could lessen the degree to which steel sample loses material by abrasive action. In this sense, Fig. 4.23 shows that, although there is a general trend towards increase in hardness at the center of the wear track, the standard deviation across measurement (portrayed by the overlapping error bars) suggests that there is not a significant difference in sample hardness.

Taken together, the findings of the current section suggest that although there is evidence that the porosity of the film continues to evolve past the time frame allocated for this experiment, it is nonetheless possible to use the the relative size of the capacitive arcs to assess the effectiveness of Dynarate 6524 as a corrosion inhibitor. It has also been shown that the composition of the steel surface is dependent on the degree of corrosion, and that wear in the absence of corrosion could be overestimated due to the presence of calcareous deposition. Lastly, the low degree of work hardening suggests that the forces used in the experiment do not compromise the transferability of these findings into the field.

Chapter 5

Conclusion and Recommendations

5.1 Conclusions

In conclusion, the present study provides evidence that all three additives manufactured by Calfrac Well Services Ltdare effective in reducing the quantity of material loss under tribocorrosion conditions regardless of their chemical make up. Through experimentation, it is inferred that this beneficial behaviour is related to the ability of the additives to favor the formation of an adsorbed hydroxide layer on the surface of the steel. Although this thin layer does not provide proper passivation as it would be observed in stainless steel, it is thought that it acts as a diffusion barrier that slows down the rate at which dissolved oxygen reaches the active metal surface.

In studying these additives, the individual contributions from mechanical wear and electrochemical degradation were measured in independent tests to assess the level of synergism between the two factors. In addition, the dominant wear regime test has been used to identify the main contribution to total material loss. It was found that, within the scope of the study, the contribution from mechanical wear accounts for a majority of the material loss in the metallic samples. This occurs, in part, due to only a slight reduction in the coefficient of friction (COF) measured in the presence of additives versus just HTDS water alone. This effect is thought to arise from the better integrity of the hydroxide film rather than from

direct action of the additives. Regarding the two organic additives, their poor performance in acting as boundary lubricants is attributed to their chemical make up that has been reported to favour the formation of adsorbed pancake structures rather than brushes on the surface of the steel.

Through the use of the statistical RSM model, it was found that Dynarate 6524 was the most successful additive at mitigating total material loss when used alone rather than in combination. A caveat to this analysis is that it also shows that there is a large variance between the different solutions tested. This is attributed to the solutions all having comparable levels of effectiveness. Nonetheless, the analysis also shows a curvature in performance associated with various concentrations of sodium sulfite (Na_2SO_3). This non-linear effect is attributed to the dissociation of the molecule in solution that contributes Na^+ ions, which affect the salinity of the electrolyte, and which in turn affects the extension of the carbon chains that make up the organic additives.

The last finding concerns the evolution of the inhibitor coating over time. In addition to the immediate inhibitory effect, some secondary longer term effects have been found. It has been postulated that this phenomenon is likely related to the tendency of the coating to reduce its porosity over time. Nonetheless, such effect has been found to take place on a time scale longer than the scope of the current study.

5.2 Recommendations

Based on the experience attained through the current work, the following recommendations are provided with the aim to improve experimental procedures as well as to inform future avenues of research:

- Measuring the exposed area is important. A procedure should be implemented to make precise measurements of any exposed area to the electrolyte. If the sample is exposed through cut outs as in the current study, the use of a cutting template is suggested to

improve consistency.

- There is a possibility that some artifacts can appear in topographical measurements taken through optical profilometry. When studying an unfamiliar system, the researcher is encouraged to verify whether such artifacts are present in the data through a complementary technique such as scanning probe microscopy (SPM).
- When the synergism approach is utilized, it is advised to reduce the cathodic overpotential as to prevent excessive calcareous deposition that could result in overestimation of wear produced by mechanical abrasion.
- The data gathered from electrochemical impedance spectroscopy suggests that the inhibitor coating is still undergoing changes even after the open circuit potential has seemingly stabilized. A future work could be focused on performing an in-depth study of such phenomena that is hinted to occur over an a time scale of several days.
- When designing novel additives for slickwater formation, boundary lubrication properties should be taken into account to reduce damage due to abrasion. There is an opportunity for developing water soluble drag reducer that can also decrease the coefficient of friction between solid contacts. Ideally, the additive would contain organic molecules that can readily form brushes or brush-like structures when adsorbed to the surface of steel.

Bibliography

[1] J. Panda, E. Yanez, and A. Mohanty, "Tribo-corrosion inhibition of AISI 4715 steel pipe carrying hydraulic fracturing fluid," *Tribology International*, vol. 161, no. March, p. 107066, 2021, doi: 10.1016/j.triboint.2021.107066.

[2] D. E. Knuth, *The TeXbook*. Boston: Addison-Wesley, 1986.

[3] L. Lamport, *LaTeX: A Document Preparation System*. Reading, Mass.: Addison-Wesley, 1986.

[4] P. Wilson, "The memoir class for configurable typesetting," 2016. [Online]. Available: https://ctan.org/pkg/memoir?lang=en

[5] NETL, "Shale Gas: Applying Technology to Solve America's Energy Challenges," National Energy Technology Laboratory, Tech. Rep., 2011. [Online]. Available: https://www.hsdl.org/?abstract&did=8711

[6] R. Wood, "Tribocorrosion," in *Shreir's Corrosion*. Elsevier, 2010, pp. 1005–1050, doi: 10.1016/B978-044452787-5.00041-X.

[7] A. Igual Muñoz and N. Espallargas, "Tribocorrosion mechanisms in sliding contacts," in *Tribocorrosion of Passive Metals and Coatings*. Elsevier, 2011, pp. 118–152, doi: 10.1533/9780857093738.1.118.

[8] D. Landolt, S. Mischler, and M. Stemp, "Electrochemical methods in tribocorrosion: A critical appraisal," *Electrochimica Acta*, vol. 46, no. 24-25, pp. 3913–3929, 2001, doi: 10.1016/S0013-4686(01)00679-X.

[9] D. Landolt, "Electrochemical and materials aspects of tribocorrosion systems," *Journal of Physics D: Applied Physics*, vol. 39, no. 15, pp. 3121–3127, 2006, doi: 10.1088/0022-3727/39/15/s01.

[10] A. Berradja, "Electrochemical Techniques for Corrosion and Tribocorrosion Monitoring: Fundamentals of Electrolytic Corrosion," in *Corrosion Inhibitors*. IntechOpen, 2019, doi: 10.5772/intechopen.85392.

[11] B. Yang, J. Zhao, J. Mao, H. Tan, Y. Zhang, and Z. Song, "Review of friction reducers used in slickwater fracturing fluids for shale gas reservoirs," pp. 302–313, 2019, doi: 10.1016/j.jngse.2018.12.016.

[12] M. P. Escudier and S. Smith, "Fully developed turbulent flow of non-Newtonian liquids through a square duct," *Proceedings of the Royal Society A: Mathematical, Physical and Engineering Sciences*, vol. 457, no. 2008, pp. 911–936, 2001, doi: 10.1098/rspa.2000.0698.

[13] W.-M. Kulicke, R. Kniewske, and J. Klein, "Preparation, characterization, solution properties and rheological behaviour of polyacrylamide," *Progress in Polymer Science*, vol. 8, no. 4, pp. 373–468, 1982, doi: 10.1016/0079-6700(82)90004-1.

[14] Y. Hu, S. Q. Wang, and A. M. Jamieson, "Rheological and Rheooptical Studies of Shear-Thickening Polyacrylamide Solutions," *Macromolecules*, vol. 28, no. 6, pp. 1847–1853, 1995, doi: 10.1021/ma00110a019.

[15] T. Kato, N. Kozaki, and A. Takahashi, "Lubrication by thin liquid films of aqueous polymer solutions," *Polymer Journal*, vol. 18, no. 2, pp. 111–116, 1986, doi: 10.1295/polymj.18.111.

[16] N. Marx, L. Fernández, F. Barceló, and H. Spikes, "Shear Thinning and Hydrodynamic Friction of Viscosity Modifier-Containing Oils. Part I: Shear Thinning Behaviour," *Tribology Letters*, vol. 66, no. 3, p. 92, 2018, doi: 10.1007/s11249-018-1039-5.

[17] ——, "Shear Thinning and Hydrodynamic Friction of Viscosity Modifier-Containing Oils. Part II: Impact of Shear Thinning on Journal Bearing Friction," *Tribology Letters*, vol. 66, no. 3, p. 91, 2018, doi: 10.1007/s11249-018-1040-z.

[18] T. J. Murdoch, E. Pashkovski, R. Patterson, R. W. Carpick, and D. Lee, "Sticky but Slick: Reducing Friction Using Associative and Nonassociative Polymer Lubricant Additives," *ACS Applied Polymer Materials*, vol. 2, no. 9, pp. 4062–4070, 2020, doi: 10.1021/acsapm.0c00687.

[19] M. Smeeth, H. Spikes, and S. Gunsel, "Boundary film formation by viscosity index improvers," *Tribology Transactions*, vol. 39, no. 3, pp. 726–734, 1996, doi: 10.1080/10402009608983590.

[20] C. M. Mate, "Friction," in *Tribology on the Small Scale*. Oxford University Press, 2007, doi: 10.1093/acprof:oso/9780198526780.001.0001.

[21] J. Gao, W. D. Luedtke, D. Gourdon, M. Ruths, J. N. Israelachvili, and U. Landman, "Frictional forces and Amontons' law: From the molecular to the macroscopic scale," *Journal of Physical Chemistry B*, vol. 108, no. 11, pp. 3410–3425, 2004, doi: 10.1021/jp036362l.

[22] P. J. Blau, "Friction Coefficient," in *Encyclopedia of Tribology*. Springer US, 2013, pp. 1304–1306, doi: 10.1007/978-0-387-92897-5˙169.

[23] ——, "Running-in," in *Encyclopedia of Tribology*. Springer US, 2013, pp. 2967–2969, doi: 10.1007/978-0-387-92897-5˙213.

[24] B. Tower, "First Report on Friction Experiments," in *Proceedings of the Institution of Mechanical Engineers*, vol. 34, no. 1. SAGE PublicationsSage UK: London, England, 1883, pp. 632–659, doi: 10.1243/PIME˙PROC˙1883˙034˙028˙02.

[25] ——, "Second Report on Friction Experiments," in *Proceedings of the Institution of Mechanical Engineers*. ASME, 1885, pp. 95–106, doi: 10.1243/PIME˙PROC˙1885˙036˙011˙02.

[26] O. Reynolds, "I. On the theory of lubrication and its application to Mr. Beauchamp tower's experiments, including an experimental determination of the viscosity of olive oil," *Proceedings of the Royal Society of London*, vol. 40, no. 242-245, pp. 191–203, 1886, doi: 10.1098/rspl.1886.0021.

[27] M. Woydt and R. Wäsche, "The history of the Stribeck curve and ball bearing steels: The role of Adolf Martens," *Wear*, vol. 268, no. 11-12, pp. 1542–1546, 2010, doi: 10.1016/j.wear.2010.02.015.

[28] R. M. Deeley, "Discussion on lubrication," in *Proceedings of the Physical Society of London*, vol. 32, no. 1. IOP Publishing, 1919, pp. 1874–1925, doi: 10.1088/1478-7814/32/1/339.

[29] B. Bhushan, "Boundary Lubrication," in *Encyclopedia of Nanotechnology*. Dordrecht: Springer Netherlands, 2016, pp. 414–423, doi: 10.1007/978-94-017-9780-1˙167.

[30] I. Langmuir, "The mechanism of the surface phenomena of flotation," *Transactions of the Faraday Society*, vol. 15, no. June, pp. 62–74, 1920, doi: 10.1039/TF9201500062.

[31] B. W. B H ardy and I. D. Da oubleday, "Boundary lubrication.— The paraffin series," *Proceedings of the Royal Society of London. Series A, Containing Papers of a Mathematical and Physical Character*, vol. 100, no. 707, pp. 550–574, 1922, doi: 10.1098/rspa.1922.0017.

[32] Z. Tang and S. Li, "A review of recent developments of friction modifiers for liquid lubricants (2007-present)," *Current Opinion in Solid State and Materials Science*, vol. 18, no. 3, pp. 119–139, 2014, doi: 10.1016/j.cossms.2014.02.002.

[33] I. Minami, T. Furesawa, T. Kubo, H. Nanao, and S. Mori, "Investigation of tribochemistry by means of stable isotopic tracers: Mechanism for durability of monomolecular boundary film," *Tribology International*, vol. 41, no. 11, pp. 1056–1062, 2008, doi: 10.1016/j.triboint.2008.01.011.

[34] M. Desanker, X. He, J. Lu, P. Liu, D. B. Pickens, M. Delferro, T. J. Marks, Y. W. Chung, and Q. J. Wang, "Alkyl-Cyclens as Effective Sulfur- and Phosphorus-Free Friction Modifiers for Boundary Lubrication," *ACS Applied Materials and Interfaces*, vol. 9, no. 10, pp. 9118–9125, 2017, doi: 10.1021/acsami.6b15608.

[35] Y. Chen, T. Hong, M. Gopal, and W. P. Jepson, "EIS studies of a corrosion inhibitor behavior under multiphase flow conditions," *Corrosion Science*, vol. 42, no. 6, pp. 979–990, 2000, doi: 10.1016/S0010-938X(99)00127-4.

[36] P. Studt, "Boundary lubrication: adsorption of oil additives on steel and ceramic surfaces and its influence on friction and wear," *Tribology International*, vol. 22, no. 2, pp. 111–119, 1989, doi: 10.1016/0301-679X(89)90171-0.

[37] S. Mischler, "Triboelectrochemical techniques and interpretation methods in tribocorrosion: A comparative evaluation," *Tribology International*, vol. 41, no. 7, pp. 573–583, 2008, doi: 10.1016/j.triboint.2007.11.003.

[38] P. Ponthiaux, F. Wenger, D. Drees, and J. P. Celis, "Electrochemical techniques for studying tribocorrosion processes," *Wear*, vol. 256, no. 5, pp. 459–468, 2004, doi: 10.1016/S0043-1648(03)00556-8.

[39] "G119-09(2016) Standard Guide for Determining Synergism Between Wear and Corrosion," ASTM International, West Conshohocken, PA, Tech. Rep., 2016.

[40] W. Li and R. K. Saini, "Polyacrylamide grafted polysaccharide as friction reducer for slickwater fracturing treatment," *https://doi-org.ezproxy.lib.ucalgary.ca/10.1080/10601325.2020.1840924*, vol. 58, no. 4, pp. 243–248, 2020, doi: 10.1080/10601325.2020.1840924.

[41] E. Willett, D. Vargo, and D. Devore, "Evaluation of Water Soluble Polymers for Aqueous Lubricants," in *74th Annual STLE Meeting*, Nashville, 2019. [Online]. Available: www.functionalproducts.com

[42] B. D. B. Tiu and R. C. Advincula, "Polymeric corrosion inhibitors for the oil and gas industry: Design principles and mechanism," pp. 25–45, 2015, doi: 10.1016/j.reactfunctpolym.2015.08.006.

[43] X. Sun and L. Yu, "Investigation of polyacrylamide containing capsaicin monomer as a novel corrosion inhibitor for mild steel in hydrochloric acid," *Materials and Corrosion*, vol. 69, no. 8, pp. 1095–1103, 2018, doi: 10.1002/MACO.201709876.

[44] X. Rao, L. Zhou, G. Zhang, X. Wang, S. Xia, and L. Yu, "Investigation of a hydrophobically associating AMAHS polyacrylamides: A new corrosion inhibitor for mild steel in HCl," *Materials and Corrosion*, vol. 71, no. 9, pp. 1521–1532, 2020, doi: 10.1002/MACO.201911464.

[45] A. López-Ortega, J. L. Arana, and R. Bayón, "Tribocorrosion of Passive Materials: A Review on Test Procedures and Standards," *International Journal of Corrosion*, vol. 2018, 2018, doi: 10.1155/2018/7345346.

[46] ——, "On the comparison of the tribocorrosion behavior of passive and non-passivating materials and assessment of the influence of agitation," *Wear*, vol. 456-457, p. 203388, 2020, doi: 10.1016/J.WEAR.2020.203388.

[47] J. Chen and W. Cai, "Effect of scratching frequency on the tribocorrosion resistance of Al-Mn amorphous thin films," *Wear*, vol. 426-427, pp. 1457–1465, 2019, doi: 10.1016/J.WEAR.2018.12.055.

[48] B. C. Wong, "Evaluation of Strategies To Reduce Erosion Corrosion of Steel Components," Master's thesis, University of Calgary, 2019.

[49] IntelLiDrives, "Linear Actuator BSMA-140H-200." [Online]. Available: http://www.intellidrives.com/Linear%7B%5C_%7DActuator%7B%5C_%7DBSMA-LY-140H-200

[50] D. Type and P. Date, "Application Design Patterns : State Machines," pp. 4–7, 2011. [Online]. Available: https://www.ni.com/en-ca/support/documentation/supplemental/16/simple-state-machine-template-documentation.html

[51] J. Chen, H. Mraied, and W. Cai, "Determining tribocorrosion rate and wear-corrosion synergy of bulk and thin film aluminum alloys," *Journal of Visualized Experiments*, vol. 2018, no. 139, p. 58235, 2018, doi: 10.3791/58235.

[52] J. N. Panda, B. C. Wong, E. Medvedovski, and P. Egberts, "Enhancement of tribocorrosion performance of carbon steel through boronizing and BN-based coatings," *Tribology International*, vol. 153, p. 106666, 2021, doi: 10.1016/j.triboint.2020.106666.

[53] "G59-97(2020) Standard Test Method for Conducting Potentiodynamic Polarization Resistance Measurements," ASTM International, West Conshohocken, PA, Tech. Rep., 2020.

[54] "G5-14e1 Standard Reference Test Method for Making Potentiodynamic Anodic Polarization Measurements," ASTM International, West Conshohocken, PA, Tech. Rep., 2014.

[55] "G102-89(2015)e1 Standard Practice for Calculation of Corrosion Rates and Related Information from Electrochemical Measurements. West Conshohocken," ASTM International, West Conshohocken, PA, Tech. Rep., 2015.

[56] "G3-14(2019) Standard Practice for Conventions Applicable to Electrochemical Measurements in Corrosion Testing," ASTM International, West Conshohocken, PA, Tech. Rep., 2019.

[57] A. C. Fernandes, F. Vaz, E. Ariza, L. A. Rocha, A. R. Ribeiro, A. C. Vieira, J. P. Rivière, and L. Pichon, "Tribocorrosion behaviour of plasma nitrided and plasma nitrided + oxidised Ti6Al4V alloy," *Surface and Coatings Technology*, vol. 200, no. 22-23 SPEC. ISS., pp. 6218–6224, 2006, doi: 10.1016/j.surfcoat.2005.11.069.

[58] A. Bard and L. Faulkner, "Techniques Based On Concepts of Impedance," in *Electrochemical Methods: Fundamentals and Applications*. John Wiley & Sons, Inc., 2001.

[59] F. Mansfeld, "Electrochemical impedance spectroscopy (EIS) as a new tool for investigating methods of corrosion protection," *Electrochimica Acta*, vol. 35, no. 10, pp. 1533–1544, 1990, doi: 10.1016/0013-4686(90)80007-B.

[60] S. Das, P. K. Baranwal, and P. V. Rajaraman, "Effect of soft cations on carbon steel corrosion in chloride media," *Corrosion Reviews*, vol. 36, no. 4, pp. 395–402, 2018, doi: 10.1515/corrrev-2017-0097.

[61] R. Cabrera-Sierra, "Corrosion Studies of Carbon Steel Immersed in NACE Brine by Weight Loss, EIS and XRD Techniques," *International Journal of Electrochemical Science*, pp. 10 185–10 198, 2016, doi: 10.20964/2016.12.32.

[62] W. Emori, S. L. Jiang, D. L. Duan, O. O. Ekerenam, Y. G. Zheng, P. C. Okafor, and Y. X. Qiao, "Corrosion behavior of carbon steel in amine-based CO2 capture system: effect of sodium sulfate and sodium sulfite contaminants," *Materials and Corrosion*, vol. 68, no. 6, pp. 674–682, 2017, doi: 10.1002/maco.201609245.

[63] E.-S. Sherif, "A Comparative Study on the Electrochemical Corrosion Behavior of Iron and X-65 Steel in 4.0 wt Exposure Intervals," *Molecules*, vol. 19, no. 7, pp. 9962–9974, 2014, doi: 10.3390/molecules19079962.

[64] E. S. M. Sherif, "Effects of 5-(3-aminophenyl)-tetrazole on the inhibition of unalloyed iron corrosion in aerated 3.5% sodium chloride solutions as a corrosion inhibitor," *Materials Chemistry and Physics*, vol. 129, no. 3, pp. 961–967, 2011, doi: 10.1016/j.matchemphys.2011.05.043.

[65] E.-S. M. Sherif, R. Erasmus, and J. Comins, "In situ Raman spectroscopy and electrochemical techniques for studying corrosion and corrosion inhibition of iron in sodium chloride solutions," *Electrochimica Acta*, vol. 55, no. 11, pp. 3657–3663, 2010, doi: 10.1016/j.electacta.2010.01.117.

[66] H. Ma, X. Cheng, G. Li, S. Chen, Z. Quan, S. Zhao, and L. Niu, "The influence of hydrogen sulfide on corrosion of iron under different conditions," *Corrosion Science*, vol. 42, no. 10, pp. 1669–1683, 2000, doi: 10.1016/S0010-938X(00)00003-2.

[67] F. Mansfeld, H. Shih, H. Greene, and R. Tsai, "Analysis of EIS Data for Common Corrosion Processes," in *Electrochemical Impedance: Analysis and Interpretation*, J. Scully, D. Silverman, and M. Kendig, Eds. 100 Barr Harbor Drive, PO Box C700, West Conshohocken, PA 19428-2959: ASTM International, 1993. [Online]. Available: http://www.astm.org/doiLink.cgi?STP1188-EB

[68] T. Q. Nguyen and C. Breitkopf, "Determination of Diffusion Coefficients Using Impedance Spectroscopy Data," *Journal of The Electrochemical Society*, vol. 165, no. 14, pp. E826–E831, 2018, doi: 10.1149/2.1151814jes.

[69] T. Kakiuchi, "Salt bridge in electroanalytical chemistry: Past, present, and future," pp. 1661–1671, 2011, doi: 10.1007/s10008-011-1373-0.

[70] F. Scholz, *Electroanalytical Methods*, 2nd ed., F. Scholz, A. Bond, R. Compton, D. Fiedler, G. Inzelt, H. Kahlert, Š. Komorsky-Lovrić, H. Lohse, M. Lovrić, F. Marken, A. Neudeck, U. Retter, F. Scholz, and Z. Stojek, Eds. Berlin, Heidelberg: Springer Berlin Heidelberg, 2010, doi: 10.1007/978-3-642-02915-8.

[71] U. Guth, F. Gerlach, M. Decker, W. Oelßner, and W. Vonau, "Solid-state reference electrodes for potentiometric sensors," *Journal of Solid State Electrochemistry*, vol. 13, no. 1, pp. 27–39, 2009, doi: 10.1007/s10008-008-0574-7.

[72] P. H. Barry, T. M. Lewis, and A. J. Moorhouse, "An optimised 3 M KCl salt-bridge technique used to measure and validate theoretical liquid junction potential values in patch-clamping and electrophysiology," *European Biophysics Journal*, vol. 42, no. 8, pp. 631–646, 2013, doi: 10.1007/s00249-013-0911-3.

[73] J. Narayanan, J. Y. Xiong, and X. Y. Liu, "Determination of agarose gel pore size: Absorbance measurements vis a vis other techniques," *Journal of Physics: Conference Series*, vol. 28, no. 1, pp. 83–86, 2006, doi: 10.1088/1742-6596/28/1/017.

[74] M. P. Mousavi and P. Bühlmann, "Reference electrodes with salt bridges contained in nanoporous glass: An underappreciated source of error," *Analytical Chemistry*, vol. 85, no. 19, pp. 8895–8901, 2013, doi: 10.1021/ac402170u.

[75] T. L. Schmitz, J. E. Action, J. C. Ziegert, and W. G. Sawyer, "The difficulty of measuring low friction: Uncertainty analysis for friction coefficient measurements," *Journal of Tribology*, vol. 127, no. 3, pp. 673–678, 2005, doi: 10.1115/1.1843853.

[76] D. L. Burris and W. G. Sawyer, "Addressing practical challenges of low friction coefficient measurements," *Tribology Letters*, vol. 35, no. 1, pp. 17–23, 2009, doi: 10.1007/s11249-009-9438-2.

[77] "E2655-14(2020) Standard Guide for Reporting Uncertainty of Test Results and Use of the Term Measurement Uncertainty in ASTM Test Methods," ASTM International, West Conshohocken, PA, Tech. Rep., 2020.

[78] "E2586-19e1 Standard Practice for Calculating and Using Basic Statisticss," ASTM International, West Conshohocken, PA, Tech. Rep., 2019.

[79] "ISO/IEC GUIDE 98-3:2008 Uncertainty of measurement — Part 3: Guide to the expression of uncertainty in measurement (GUM:1995)," International Organization for Standardization (ISO), Tech. Rep., 2010.

[80] S. Sturm and B. Jančar, "Microstructure Characterization of Advanced Ceramics," in *Advanced Ceramics for Dentistry*. Elsevier Inc., 2014, pp. 151–172, doi: 10.1016/B978-0-12-394619-5.00008-0.

[81] K. H. Goh, T. T. Lim, and P. C. Chui, "Evaluation of the effect of dosage, pH and contact time on high-dose phosphate inhibition for copper corrosion control using response surface methodology (RSM)," *Corrosion Science*, vol. 50, no. 4, pp. 918–927, 2008, doi: 10.1016/j.corsci.2007.12.008.

[82] F. Gapsari, R. Soenoko, A. Suprapto, and W. Suprapto, "Minimization of corrosion rate using response surface methodology," Tech. Rep., 2018. [Online]. Available: http://er.riteh.hr/index.php/ER/article/view/804

[83] P. R. Prabhu, D. Prabhu, and P. Rao, "Analysis of Garcinia indica Choisy extract as eco-friendly corrosion inhibitor for aluminum in phosphoric acid using the design of experiment," *Journal of Materials Research and Technology*, vol. 9, no. 3, pp. 3622–3631, 2020, doi: 10.1016/j.jmrt.2020.01.100.

[84] V.-M. Tapani, "Experimental Optimization and Response Surfaces," in *Chemometrics in Practical Applications*. InTech, 2012, doi: 10.5772/33265.

[85] T. Barker and A. Milivojevich, *Quality by Experimental Design*, 4th ed. Boca Raton: CRC Press, 2016.

[86] R. Myers, D. Montgomery, and C. Anderson-Cook, *Response Surface Methodology Process and Porduct Optimization Using Designed Experiments*, 4th ed. New Jersey: John Wiley & Sons, Inc., 2016.

[87] R. W. Revie and H. H. Uhlig, *Corrosion and Corrosion Control*. Hoboken, NJ, USA: John Wiley & Sons, Inc., 2008, doi: 10.1002/9780470277270.

[88] H. Parangusan, J. Bhadra, and N. Al-Thani, "A review of passivity breakdown on metal surfaces: influence of chloride- and sulfide-ion concentrations, temperature, and pH," *Emergent Materials*, 2021, doi: 10.1007/s42247-021-00194-6.

[89] P. Refait, A.-M. Grolleau, M. Jeannin, C. Rémazeilles, and R. Sabot, "Corrosion of Carbon Steel in Marine Environments: Role of the Corrosion Product Layer," *Corrosion and Materials Degradation*, vol. 1, no. 1, pp. 198–218, 2020, doi: 10.3390/cmd1010010.

[90] S. J. Oh, D. C. Cook, and H. E. Townsend, "Characterization of iron oxides commonly formed as corrosion products on steel," *Hyperfine Interactions*, vol. 112, no. 1-4, pp. 59–66, 1998, doi: 10.1023/a:1011076308501.

[91] S. L. Grise and B. J. Saldanha, "Effects of Oxygen, Temperature and Salinity On Carbon Steel Corrosion in Aqueous Solutions; Model Predictions versus Laboratory Results," Tech. Rep., 2008. [Online]. Available: http://onepetro.org/NACECORR/proceedings-pdf/CORR08/All-CORR08/NACE-08271/1806112/nace-08271.pdf

[92] G. Frankel and R. Cottis, "Principles of Corrosion in Liquids," in *Shreir's Corrosion*. Elsevier, 2010, pp. 725–730, doi: 10.1016/B978-044452787-5.00027-5.

[93] L. R. Rudnick, Ed., *Lubricant Additives*. CRC Press, 2009, doi: 10.1201/9781420059656.

[94] G. Stachowiak and A. Batchelor, "Boundary and Extreme Pressure Lubrication," in *Engineering Tribology*. Elsevier, 2014, pp. 371–428, doi: 10.1016/B978-0-12-397047-3.00008-4.

[95] P. A. Williams, *Handbook of Industrial Water Soluble Polymers*. John Wiley and Sons, 2007, doi: 10.1002/9780470988701.

[96] Y. Wang, K. Chen, L. Mo, and H. Hu, "A cationic polyacrylamide dispersion synthesis by dispersion polymerization in aqueous solution," Tech. Rep. 3, 2011.

[97] G. B. Butler and N. Z. Zhang, "Synthetic Methods for Water-Soluble Monomers and Polymers," in *Water-Soluble Polymers*, 1991, pp. 25–56, doi: 10.1021/bk-1991-0467.ch002.

[98] W. D. Ihlenfeldt, E. E. Bolton, and S. H. Bryant, "The PubChem chemical structure sketcher," *Journal of Cheminformatics*, vol. 1, no. 1, p. 20, 2009, doi: 10.1186/1758-2946-1-20.

[99] D. A. Wever, F. Picchioni, and A. A. Broekhuis, "Polymers for enhanced oil recovery: A paradigm for structure-property relationship in aqueous solution," pp. 1558–1628, 2011, doi: 10.1016/j.progpolymsci.2011.05.006.

[100] S. Peng and C. Wu, "Light Scattering Study of the Formation and Structure of Partially Hydrolyzed Poly(acrylamide)/Calcium(II) Complexes," *Macromolecules*, vol. 32, no. 3, pp. 585–589, 1999, doi: 10.1021/ma9809031.

[101] S. Papavinasam, "Corrosion Inhibitors," in *Uhlig's Corrosion Handbook: Third Edition*. John Wiley and Sons, 2011, pp. 1021–1032, doi: 10.1002/9780470872864.ch71.

[102] S. Gunsel, M. Smeeth, and H. Spikes, "Friction and Wear Reduction by Boundary Film-Forming Viscosity Index Improvers." SAE Technical Paper 962037, 1996, doi: 10.4271/962037.

[103] W. J. Brittain and S. Minko, "A structural definition of polymer brushes," *Journal of Polymer Science, Part A: Polymer Chemistry*, vol. 45, no. 16, pp. 3505–3512, 2007, doi: 10.1002/pola.22180.

[104] J. Rühe, "Polymer Brushes: On the Way to Tailor-Made Surfaces," in *Polymer Brushes*. Wiley-VCH, 2004.

[105] H. Spikes, "Friction Modifier Additives," *Tribology Letters*, vol. 60, no. 1, pp. 1–26, 2015, doi: 10.1007/s11249-015-0589-z.

[106] J. Guegan, M. Southby, and H. Spikes, "Friction Modifier Additives, Synergies and Antagonisms," *Tribology Letters*, vol. 67, no. 3, p. 83, 2019, doi: 10.1007/s11249-019-1198-z.

[107] E. Hart, *Corrosion inhibitors: Principles, mechanisms and applications*. Nova Science Publishers, Inc., 2016, doi: 10.5772/57255.

[108] S. A. Umoren, "Polymers as Corrosion Inhibitors for Metals in Different Media - A Review," *The Open Corrosion Journal*, vol. 2, no. 1, pp. 175–188, 2009, doi: 10.2174/1876503300902010175.

[109] K. H. Rashid and A. A. Khadom, "Sodium sulfite as an oxygen scavenger for the corrosion control of mild steel in petroleum refinery wastewater: optimization, mathematical modeling, surface morphology and reaction kinetics studies," *Reaction Kinetics, Mechanisms and Catalysis*, vol. 129, no. 2, pp. 1027–1046, 2020, doi: 10.1007/s11144-020-01738-3.

[110] I. A. Chaves, R. Jeffrey, and R. E. Melchers, "Technical Note: Rust Removal from Steel Coupons After Short-Term Marine Immersion," *CORROSION*, vol. 71, no. 7, pp. 811–818, 2015, doi: 10.5006/1649.

[111] M. M. Stack and G. H. Abdulrahman, "Mapping erosion-corrosion of carbon steel in oil exploration conditions: Some new approaches to characterizing mechanisms

and synergies," *Tribology International*, vol. 43, no. 7, pp. 1268–1277, 2010, doi: 10.1016/j.triboint.2010.01.005.

[112] M. M. Stack, S. M. Abdelrahman, and B. D. Jana, "Some perspectives on modelling the effect of temperature on the erosioncorrosion of Fe in aqueous conditions," *Tribology International*, vol. 43, no. 12, pp. 2279–2297, 2010, doi: 10.1016/j.triboint.2010.07.015.

[113] Minitab, "Interpret the key results for Analyze Response Surface Design - Minitab." [Online]. Available: https://support.minitab.com/en-us/minitab/18/help-and-how-to/modeling-statistics/doe/how-to/response-surface/analyze-response-surface-design/interpret-the-results/interpret-the-results/

[114] G. Dingilian and E. Ruckenstein, "Positive and negative deviations from additivity in drag reduction of binary dilute polymer solutions," *AIChE Journal*, vol. 20, no. 6, pp. 1222–1224, 1974, doi: 10.1002/aic.690200628.

[115] D. A. Jones, "Polarization Methods to Measure Corrosion Rate," in *Principles and Prevention of Corrosion*. Prentice-Hall Inc., 1996.

Appendix A: HTDS water analysis

Extended water analysis

Cations			Anions			Other Measurements	
Ion	**mg/L**	**meq/L**	**Ion**	**mg/L**	**meq/L**	**Measurement**	**Value**
Al	0.06	0	Cl	141506	3991	TDS	233956
Ba	9.4	0.14	HCO_3	78	1.3	Specific Gravity	1.153
Be	<0.01	0	SO_4	377	7.8	pH	6.0
Bi	<0.13	0	CO_3	0	0	Temperature (°C)	24
Cd	<0.01	0	OH	0	0	Total Alkalinity	
Ca	9598	479				as $CaCO_3$(mg/L)	64
Cr	<0.01	0				Hardness	
Co	<0.04	0				as $CaCO_3$(mg/L)	31305
Cu	<0.01	0				H_2S Present	No
Fe	1.4	0.05				Arsenic (mg/L)	<0.25
Pb	<0.17	0				Boron (mg/L)	105
Li	42	6.1				Phosphorus (mg/L)	<1.3
Mg	1782	147				Selenium (mg/L)	<0.49
Mn	97	0.35				Silicon (mg/L)	10
Mo	<0.04	0					
Ni	<0.06	0					
K	3682	94					
Na	76128	3311					
Sr	625	14					
Tl	<0.20	0					
V	<0.02	0					
Zn	0.24	0					
Zr	<0.01	0					
Total Cations		4051.6	Total Anions		4000.1	Ion Balance (%)	1

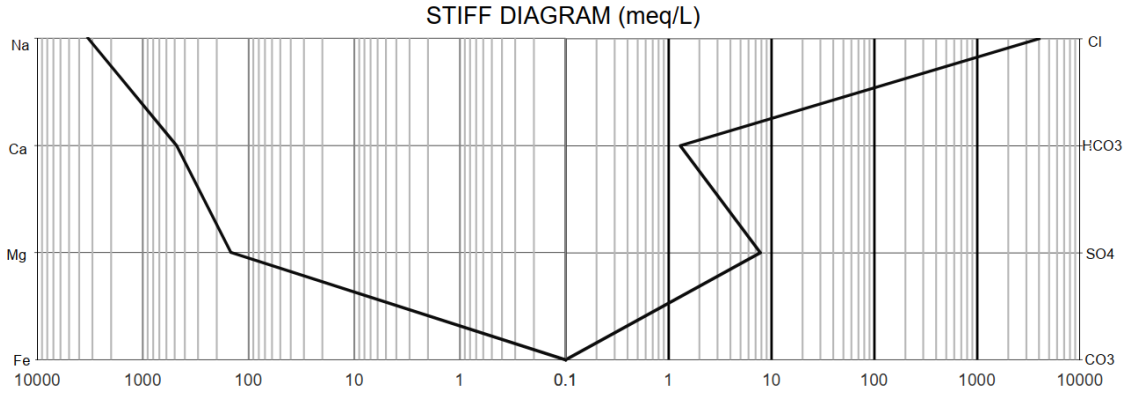
STIFF DIAGRAM (meq/L)
Na
Ca
Mg
Fe
Cl
HCO3
SO4
CO3
10000
1000
100
10
1
0.1
1
10
100
1000
10000

Appendix B: Equations Related to the Measurement of the Coefficient of Friction

The following derivation, taken from [76], shows that by using the average values of the forces involved F_i, the measured friction coefficient $\bar{\mu}'$ accurately represents the interfacial friction coefficient μ regardless of the angle of misalignment α:

$$\begin{aligned}
\bar{\mu}' &= \frac{\frac{1}{2}(F_{Xf} - F_{Xr})}{F_{Z(\text{Average})}} \\
&= \frac{\mu F_n \cos(\alpha) - F_n \sin(\alpha) + \mu F_n \cos(\alpha) + F_n \sin(\alpha)}{F_n \cos(\alpha) + \mu F_n \sin(\alpha) + F_n \cos(\alpha) - \mu F_n \sin(\alpha)} \\
&= \frac{\mu F_n \cos(\alpha) + \mu F_n \cos(\alpha)}{F_n \cos(\alpha) + F_n \cos(\alpha)} \\
&= \frac{2\mu F_n \cos(\alpha)}{2F_n \cos(\alpha)} \\
&= \mu
\end{aligned}$$

Since $\bar{\mu}'$ is composed of averaged quantities F_i, the uncertainty according to the uncertainty propagation rule, Equation 3.6, it is necessary to explicitly show all the terms in $\bar{\mu}'$ as follows:

$$\bar{\mu}' = \frac{\frac{1}{2}(F_{Xf} - F_{Xr})}{\frac{1}{2}(F_{Zf} + F_{Zr})}.$$

The term $(\frac{1}{2}(F_{Zf} + F_{Zr}))^{-1}$ can be multiplied on the numerator and denominator to result in an expression that can be easily derived through the product rule as follows:

$$\bar{\mu}' = \frac{(F_{Xf} - F_{Xr})}{(F_{Zf} + F_{Zr})} = \frac{(F_{Xf} - F_{Xr}) \cdot (F_{Zf} + F_{Zr})^{-1}}{(F_{Zf} + F_{Zr}) \cdot (F_{Zf} + F_{Zr})^{-1}} = (F_{Xf} - F_{Xr}) \cdot (F_{Zf} + F_{Zr})^{-1}.$$

The following are the partial differentials of $\bar{\mu}'$:

$$\begin{aligned}
\frac{\partial \bar{\mu}'}{\partial F_{Xf}} &= \frac{\partial \left(F_{Xf} - F_{Xr}\right)}{\partial F_{Xf}} \cdot \left(F_{Zf} + F_{Zr}\right)^{-1} + \left(F_{Xf} - F_{Xr}\right) \cdot \frac{\partial \left(F_{Zf} + F_{zr}\right)^{-1}}{\partial F_{Xf}} \\
&= (1) \cdot \left(F_{Zf} + F_{zr}\right)^{-1} + \left(F_{Xf} - F_{Xr}\right) \cdot \frac{\partial \left(F_{Zf} + F_{zr}\right)^{-1}}{\partial \left(F_{Zf} + F_{zr}\right)} \cdot \frac{\partial \left(F_{Zf} + F_{zr}\right)}{\partial F_{Xf}} \\
&= \left(F_{Zf} + F_{zr}\right)^{-1} + \left(F_{Xf} - F_{Xr}\right) \cdot (-1) \cdot \left(F_{Zf} + F_{Zr}\right)^{-2} \cdot (0) \\
&= \frac{1}{F_{Zf} + F_{zr}} \\
\frac{\partial \bar{\mu}'}{\partial F_{Xr}} &= \frac{\partial \left(F_{Xf} - F_{Xr}\right)}{\partial F_{Xr}} \cdot \left(F_{Zf} + F_{Zr}\right)^{-1} + \left(F_{Xf} - F_{Xr}\right) \cdot \frac{\partial \left(F_{Zf} + F_{zr}\right)^{-1}}{\partial F_{Xr}} \\
&= (-1) \cdot \left(F_{Zf} + F_{zr}\right)^{-1} + \left(F_{Xf} - F_{Xr}\right) \cdot \frac{\partial \left(F_{Zf} + F_{zr}\right)^{-1}}{\partial \left(F_{Zf} + F_{zr}\right)} \cdot \frac{\partial \left(F_{Zf} + F_{zr}\right)}{\partial F_{Xr}} \\
&= (-1) \cdot \left(F_{Zf} + F_{zr}\right)^{-1} + \left(F_{Xf} - F_{Xr}\right) \cdot (-1) \cdot \left(F_{Zf} + F_{Zr}\right)^{-2} \cdot (0) \\
&= -\frac{1}{F_{Zf} + F_{Zr}} \\
\frac{\partial \bar{\mu}'}{\partial F_{Zf}} &= \frac{\partial \left(F_{Xf} - F_{Xr}\right)}{\partial F_{Zf}} \cdot \left(F_{Zf} + F_{Zr}\right)^{-1} + \left(F_{Xf} - F_{Xr}\right) \cdot \frac{\partial \left(F_{Zf} + F_{zr}\right)^{-1}}{\partial F_{Zf}} \\
&= (0) \cdot \left(F_{Zf} + F_{Zr}\right)^{-1} + \left(F_{Xf} - F_{Xr}\right) \cdot \frac{\partial \left(F_{Zf} + F_{zr}\right)^{-1}}{\partial \left(F_{Zf} + F_{zr}\right)} \cdot \frac{\partial \left(F_{Zf} + F_{zr}\right)}{\partial F_{Zf}} \\
&= \left(F_{Xf} - F_{Xr}\right) \cdot (-1) \cdot \left(F_{Zf} + F_{Zr}\right)^{-2} \cdot (1) \\
&= \frac{F_{Xr} - F_{Xf}}{\left(F_{Zf} + F_{Zr}\right)^2} \\
\frac{\partial \bar{\mu}'}{\partial F_{Zr}} &= \frac{\partial \left(F_{Xf} - F_{Xr}\right)}{\partial F_{Zr}} \cdot \left(F_{Zf} + F_{Zr}\right)^{-1} + \left(F_{Xf} - F_{Xr}\right) \cdot \frac{\partial \left(F_{Zf} + F_{zr}\right)^{-1}}{\partial F_{Zr}} \\
&= (0) \cdot \left(F_{Zf} + F_{Zr}\right)^{-1} + \left(F_{Xf} - F_{Xr}\right) \cdot \frac{\partial \left(F_{Zf} + F_{zr}\right)^{-1}}{\partial \left(F_{Zf} + F_{zr}\right)} \cdot \frac{\partial \left(F_{Zf} + F_{zr}\right)}{\partial F_{Zr}} \\
&= \left(F_{Xf} - F_{Xr}\right) \cdot (-1) \cdot \left(F_{Zf} + F_{Zr}\right)^{-2} \cdot (1) \\
&= \frac{F_{Xr} - F_{Xf}}{\left(F_{Zf} + F_{Zr}\right)^2}
\end{aligned}$$

Collecting it all together into Equation 3.6, the combined error u_c for the calculated friction coefficient $\bar{\mu}'$ per reciprocating cycle is calculated as follows:

$$u_c^2\left(\bar{\mu}^{'}\right) = \sum_{i=1}^{n} \left(\frac{\partial \bar{\mu}^{'}}{\partial F_i}\right)^2 \cdot u^2\left(F_i\right)$$

$$u_c^2\left(\bar{\mu}'\right) = \left(\frac{1}{F_{Zf}+F_{zr}}\right)^2 \cdot s^2\left(F_{Xf}\right) + \left(-\frac{1}{F_{Zf}+F_{Zr}}\right)^2 \cdot s^2\left(F_{Xr}\right) + \left(\frac{F_{Xr}-F_{Xf}}{\left(F_{Zf}+F_{Zr}\right)^2}\right)^2 \cdot s^2\left(F_{Zf}\right) + \left(\frac{F_{Xr}-F_{Xf}}{\left(F_{Zf}+F_{Zr}\right)^2}\right)^2 \cdot s^2\left(F_{Zr}\right)$$

$$u_c\left(\bar{\mu}'\right) = \left(\left(\frac{1}{F_{Zf}+F_{zr}}\right)^2 \cdot s^2\left(F_{Xf}\right) + \left(-\frac{1}{F_{Zf}+F_{Zr}}\right)^2 \cdot s^2\left(F_{Xr}\right) + \left(\frac{F_{Xr}-F_{Xf}}{\left(F_{Zf}+F_{Zr}\right)^2}\right)^2 \cdot s^2\left(F_{Zf}\right) + \left(\frac{F_{Xr}-F_{Xf}}{\left(F_{Zf}+F_{Zr}\right)^2}\right)^2 \cdot s^2\left(F_{Zr}\right)\right)^{\frac{1}{2}}$$

Appendix C: Optical Artifacts

In section 3.4.2.1 it was mentioned that some artifacts tend to appear in the measurements conducted by optical profilometry at locations of abrupt changes in depth, and at the border between high contrast areas. As a demonstration of such effects, below are two extreme examples taken on a sample of known topology. The object is a printed circuit board (PCB) consisting of plated metal connections embedded in a black resin. In both examples, the metallic connectors lay deeper than the surrounding resin. In addition to the line profile taken with the accompanying software, a reconstructed topographic map is provided with each example. These maps show us what the instrument sees when performing the measurement. These maps are constructed from raw optical profilometry data as the topography exceeds the tolerances needed for SPM. The justification behind choosing such large features is the need to observe the presence or absence of such features at a macroscopic level.

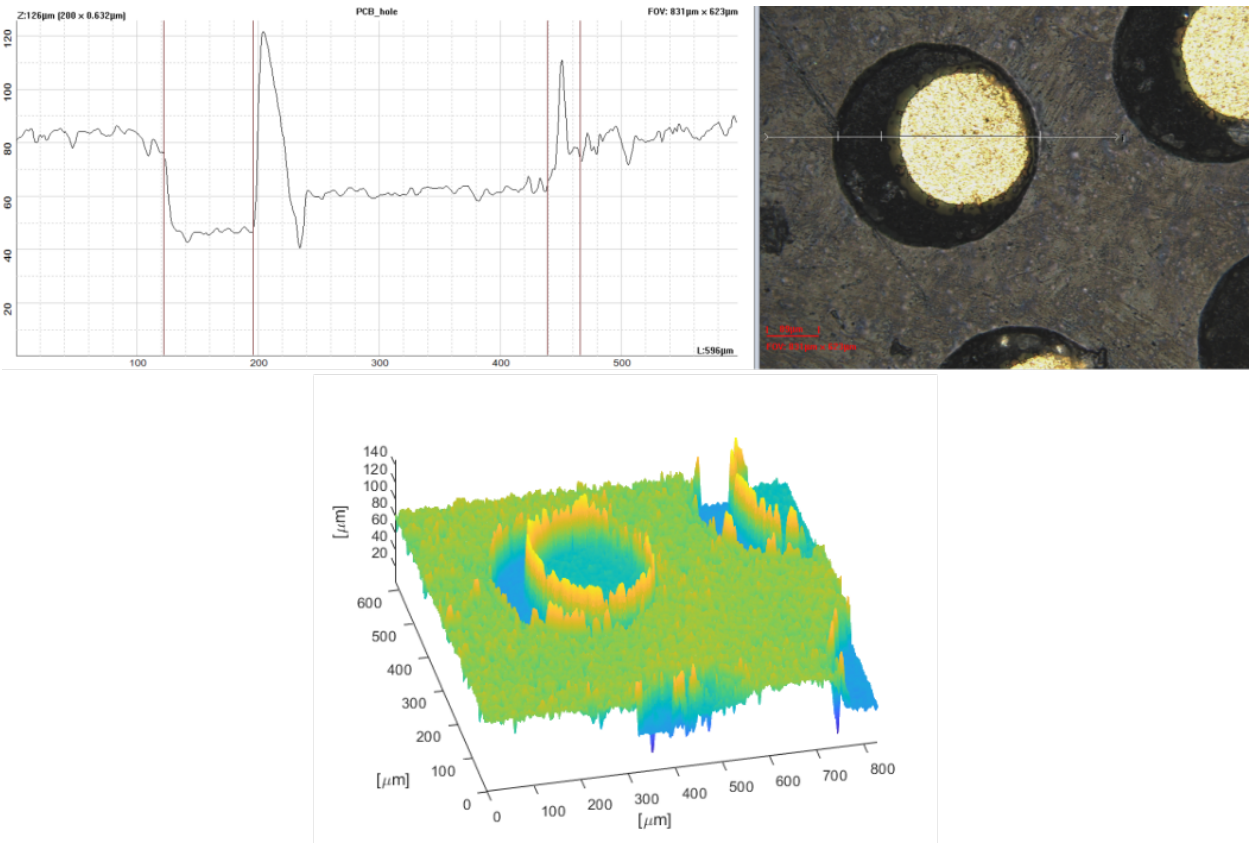

Example 1: Terminal connectors on the PCB.

The line profile on the top left corresponds to the white line superimposed on the image of the PCB on the top right. A correct representation would show a flat region at both ends of the line where the top surface of the PCB is known to be flat. This is somewhat in agreement with the measured profile that shows a relative flat horizontal line at both ends. However, towards the middle of the line profile, the segment crossing over the metal plating should be at the lowest point. This is not the case according to the measurement. Noteworthy, there is a large peak at the 200 μm mark where a non-existent rise is observed by the instrument. Likewise, the line profile also covers a section of the left wall of the cylindrical well. The expected observation in this region is a downward slope from the top of the PCB towards the metallic plating. Instead, the segment is measured as a continuous flat section.

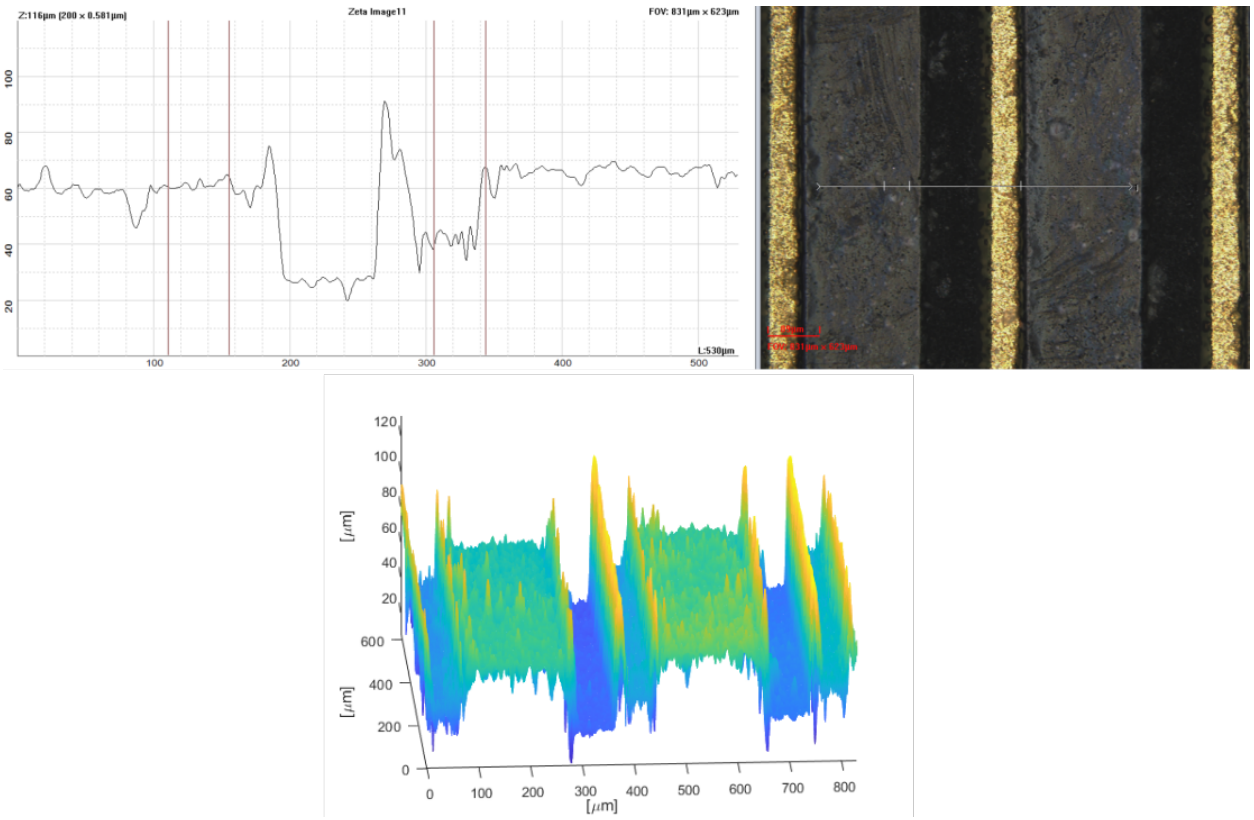

Example 2: Wire traces through the PCB.

The line profile on the top left corresponds to the white line superimposed on the image of the PCB on the top right. A correct representation would show a flat region over the gray segments. Again, this region matches the known surface of the PCB. Then, the same issue as observed in Example 1 occurs at around the 200 μm mark where a descending slope should be observed but instead, the darker region appears as a flat section. Then, continuing from left to right, an artifact shows a perceived peak in the surface at the point where the dark region gives way to the much more reflective metallic region.

Appendix D: Reduced RSM Model

The following are tables summarizing the results from the reduced Model. The reduced model was obtained in Minitab by setting the significance threshold at which terms with larger P-values than 0.05 were systematically removed.

Analysis of coded coefficients

Coded Coefficients					
Term	Coef	SE Coef	T-Value	P-Value	VIF
Constant	612.7	24.3	25.19	0	
Dynarate	-89.4	34.4	-2.6	0.019	1
Calguard	148	34.4	4.3	0.001	1
Dynarate*DWP	96.1	38.5	2.5	0.024	1

Analysis of Variance

ANOVA					
Source	**DF**	**Adj SS**	**Adj MS**	**F-Value**	**P-Value**
Model	3	372877	124292	10.5	0
Linear	2	298970	149485	12.63	0.001
Dynarate	1	79867	79867	6.75	0.019
Calguard	1	219103	219103	18.51	0.001
2-Way Interaction	1	73907	73907	6.24	0.024
Dynarate·DWP	1	73907	73907	6.24	0.024
Error	16	189377	11836		
Lack-of-Fit	11	151439	13767	1.81	0.265
Pure Error	5	37939	7588		
Total	19	562254			

Summary Statistics for the CCD Model

Model Summary			
S	**R-sq**	**R-sq(adj)**	**R-sq(pred)**
108.794	66.32%	60.00%	47.39%

Optimal additive combination

Variable	**Setting**
Dynarate	1
DWP	0
Calguard	0

Predicted response at optimal parameters

Response	**Fit**	**SE Fit**	**95% CI**	**95% PI**
Lin. Wear (um^2)	279.2	66.6	(138.0, 420.5)	(8.8, 549.7)

Appendix E: Extended drift experiment

The following is a Nyquist plot showing the continuous increase in the size of the capacitive arc for an experiment in which the system was allowed to corrode for a period of approximately 15 hours. Represented in the figure are a total number of 86 PEIS measurements.